

# UNIVERSITY OF NAPLES FEDERICO II

*Department of Chemical, Materials and Production Engineering*



**PhD Thesis in**

**Innovative Technologies for Materials, Sensors and Imaging**

*28<sup>th</sup> cycle*

***Sol-gel synthesis of inorganic and hybrid transition  
metal oxides based materials***

***Luciana Minieri***

**Tutor:**

Prof. Antonio Aronne

**Coordinator:**

Prof. Antonio Cassinese

*May 2016*

# CONTENTS

<b>INTRODUCTION</b>	p. 3
<b>PUBLICATIONS</b>	p. 16
<b>CHAPTER 1: SOL–GEL</b>	
1.1 Sol-Gel Technology	p. 19
1.2 Sol-gel Chemistry	p. 21
1.3 Role of organic ligands	p. 26
1.4 Role of surfactant agent	p. 29
<b>CHAPTER 2: EXPERIMENTAL SECTION</b>	
2.1 ZrO <sub>2</sub> -acetylacetonate (HSGZ)	p. 31
2.2 Nb <sub>2</sub> O <sub>5</sub> •SiO <sub>2</sub> and Ru/RuO <sub>2</sub> @Nb <sub>2</sub> O <sub>5</sub> •SiO <sub>2</sub>	p. 35
<b>CHAPTER 3: RESULTS AND DISCUSSION - PART 1</b>	
3.1 ZrO <sub>2</sub> -acac hybrid material	p. 43
3.2 Thermal and structural characterization	p. 43
3.3 Technological applications	p. 53
3.3.1 Long-Term Application	p. 60
<b>RESULTS AND DISCUSSION - PART 2A</b>	
3.4 Nb <sub>2</sub> O <sub>5</sub> •SiO <sub>2</sub> mixed oxides	p. 63
3.5 Structural and morphological characterization	p. 64
3.6 Catalytic activity: methyl oleate epoxidation	p. 68
<b>RESULTS AND DISCUSSION - PART 2B</b>	
3.7 Ru/RuO <sub>2</sub> @Nb <sub>2</sub> O <sub>5</sub> •SiO <sub>2</sub> (RNS) bifunctional mixed oxides	p. 71
3.8 Thermal, structural and morphological characterization	p. 71
3.9 Catalytic activity: Levulinic Acid (LA) hydrogenation	p. 81

**CONCLUSION**

**p. 87**

**REFERENCES**

**p. 90**

## INTRODUCTION

Nowadays, nanomaterials have received much attention because of their potential applications in various fields. Among them, electrochemical energy storage/conversion device and catalysis have attracted a lot of interest.

Nanomaterials employed as catalysts can be synthesized by either top-down or bottom-up methods.

Among top-down methods, coprecipitation, impregnation and grafting should be mentioned, in which the active phase is dispersed on the surface of an inert support. In these synthesis procedures the support and the active phase are synthesized separately, making difficult to avoid the segregation of the latter, especially at high content.

Compared with such methods, the sol-gel (bottom-up approach) exhibits many advantages, such as the high control of purity and composition of the final product, the low temperature process, fine tuning of microstructure as well as textural properties of the final material.

The research activity of this PhD project was focused on the preparation by sol-gel synthesis of two important classes of porous materials containing transition-metal oxides: hybrid organic-inorganic and inorganic materials. These materials act as heterogeneous catalysts in several reaction of industrial interest. Thermal, structural and morphological analysis will be also performed in order to optimize the characteristics of these solids in view of their use in technological applications.

### ***ZrO<sub>2</sub>-based organic-inorganic hybrid materials***

In the last years, among possible applications of doped and defective transition-metal oxides, advanced oxidation processes (AOPs) have been widely used for the wastewaters treatment. The prototypical mechanism involves catalyst photoexcitation and subsequent formation of 'Reactive Oxygen Species' (ROS) that act as oxidant agents.

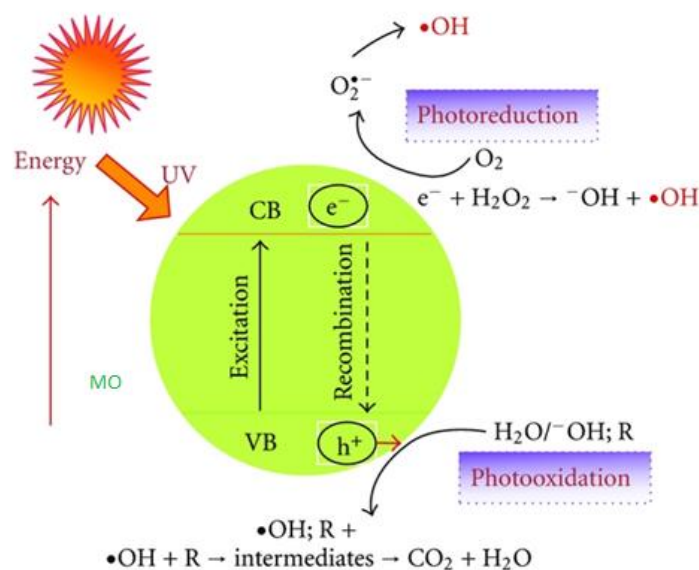


**Figure I.1.** Schematic representation of photocatalytic process

The most studied photocatalytic systems are TiO<sub>2</sub>-based materials. Recently, Macwan et al.<sup>1</sup> have prepared titania-based photocatalytic systems to decompose unwanted and toxic organic compounds, to destroy pollutants from contaminated water and air and to kill harmful bacteria and cancer cells, under irradiation by ultraviolet light (band gap around 3.2 eV). However, the low quantum efficiency, due to an inefficient capture of sunlight (less than 5%) that contains prevalently visible and near-infrared radiation, represents a strong limitation to numerous applications.

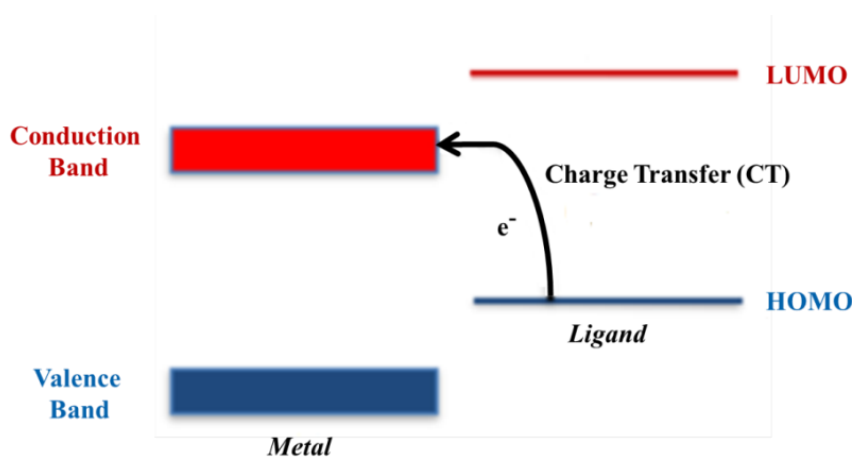
Zirconia-based systems have been rarely applied in photocatalysis because of its larger band gap of about 5.0 eV, energy value corresponding to a negligible fraction of the sunlight.

The common way to modify large band-gap semiconductors is the doping with metallic or non-metallic elements, generating intermediate energy state in the lattice.<sup>2,3</sup> Cerium-doped ZrO<sub>2</sub> (Ce-ZrO<sub>2</sub>) heterostructures<sup>4,5</sup> have shown some extent of photosensitivity to visible light as consequence of the formation of intraband gap between the conductive band (CB) and the valence band (VB) of the oxide because of Ce 4f empty states.

The electronic transitions between the semiconductor bands and dopant levels occur absorbing visible light by two different sensitization mechanisms. In the first one, relatively large dye molecules are adsorbed onto an oxide surface and electronic transition between HOMO and LUMO of dye molecules occurs absorbing a visible light photon. After that, electrons are injected from the excited dye molecule into the conduction band

of the semiconductor. This first mechanism has been extensively studied in common dye-sensitized solar cells.<sup>6-8</sup> In the second mechanism, relatively small organic molecules (dopant) adsorbed on the oxide surface form a charge transfer (CT) complex that absorbs in the visible region at energy lower than either the chelating molecules or the oxide particles. In this case, direct injection of an electron from the ground state of the molecule into the conduction band of the oxide occurs without the involvement of any excited molecular state. This direct charge transfer from the HOMO of the adsorbed molecule to the conduction band (CB) of the oxide can be seen as ligand-to-metal charge transfer (LMCT) process.<sup>2,3</sup>

Among electron rich ligands, salicylate and salicylic, dopamine, catechol and acetylacetone are oxygen-based bidentate ligands that can induce a charge transfer (CT) state with semiconductors.<sup>9,10</sup>



**Scheme S- I.1.** Energy diagram relative to ligand-to-metal charge transfer (LMCT) mechanism.

The possibility to combine properties of organic and inorganic components for materials design and processing is a very old challenge that likely started since ages (Egyptian inks, green bodies of china ceramics, prehistoric frescos, etc.).

The so-called hybrid organic-inorganic materials are not a simple physical mixture. They can be broadly defined as nanomaterials with organic and inorganic components intimately mixed. Indeed, hybrids are either homogeneous systems derived from monomers and miscible organic and inorganic components, or heterogeneous systems (nanocomposites) where at least one of the components' domains has a dimension ranging from some angstroms to several nanometers.<sup>11</sup> Properties of these materials are not only

the sum of the individual contributions of both phases, but the role of the inner interfaces could be predominant. However, the concept of “*hybrid organic-inorganic*” nanomaterials exploded only in the eighties with the expansion of soft inorganic chemistry processes and its development is one of the big achievements of sol-gel science. Indeed, the mild synthetic conditions offered by the sol-gel process (metal alkoxide precursors, organic solvents, low processing temperatures, processing versatility of the colloidal state) allow the mixing of inorganic and organic components at the nanometric scale.<sup>12</sup> Since then, the study of so-called functional hybrid nanocomposites became a field of investigation in rapid growth yielding innovative advanced materials with high added value.

These materials being at the interface of organic and inorganic realms are highly versatile offering a wide range of possibilities to elaborate tailor-made materials in terms of processing and chemical and physical properties.<sup>13</sup> They can be divided into two distinct classes based on the nature of the interface.<sup>11</sup>

Class *I*, organic and inorganic components are embedded and only weak bonds (hydrogen or van der Waals bonds) give the cohesion to the whole structure.

Class *II* materials, the two phases are linked together through strong chemical bonds (covalent or ionic-covalent bonds).

Organic-inorganic hybrids can be applied in many areas of materials chemistry because they are simple to process and are amenable to design on the molecular scale. The most important advantage offered by these materials is the possibility of combining the mechanical, thermal, and structural stability of a rigid inorganic framework together with the high reactivity of the organic component. Hybrid materials have already found numerous applications such as: smart membranes, new catalysts and sensors, new generation of photovoltaic and fuel cells, smart microelectronic, micro-optical and photonic components and systems, or intelligent therapeutic vectors that combine targeting, imaging, therapy and controlled release properties.<sup>14</sup>

In the 2011 *Chem. Soc. Rev.* themed issue devoted to hybrid materials,<sup>15</sup> the preparation methods, the properties and the applications of hybrid organic-inorganic materials have been extensively reviewed.

Recently, many researchers have prepared hybrid zirconia-based materials by sol-gel. Acetylacetone (2,4-pentanedione, *Hacac*) is often used in the sol-gel procedure to control the reactivity of the zirconium precursors, such as zirconium(IV) propoxide ( $Zr(OPr)_4$ ).

The influence of  $\beta$ -diketones, including *Hacac*, on the hydrolysis of zirconium alkoxides has been widely studied.<sup>11,16-24</sup>

In 2012 Georgieva et al.<sup>25</sup> have synthesized hybrid zirconia materials modified with *Hacac* by sol-gel route. They have demonstrated that modifying agents like *Hacac* and nitric acid decrease the optical band gap of the sol-gel zirconia from about 5 eV to about 3 eV.

Despite numerous investigations, however, the chemistry and structure of Zr(IV)-*acetylacetonate* (Zr(IV)-*acac*) complexes in zirconia gels and during gelation are not well understood. As a matter of fact, doping the solution of precursors with *Hacac*, a clearly visible change from transparent to yellow-brown color occurs. This color is caused by the Zr(IV)-*acac* complex formation during hydrolysis in the liquid (sol) state, which exhibits strong absorption in the UV region and low-intensity absorption in the visible spectral region.<sup>26</sup>

Therefore, the experimental conditions and the precursors determine the characteristics of the hybrid zirconia gel-derived. The formation of chemical homogeneous gels depends on the sol stabilization. Two mechanisms have been proposed to explain this stabilization. A first mechanism is based on the hypothesis that the kinetic control is exerted by the modifying chelating ligand on hydrolysis and polycondensation reactions of zirconium alkoxide. According to this mechanism, chelating ligands block the Zr<sup>4+</sup> coordination sites decreasing the rate of hydrolysis and polycondensation.<sup>11,16,19,20</sup>

A more recent interpretation has been suggested by Kessler et al.,<sup>22</sup> and supported by papers recently published.<sup>23,24</sup> According to this interpretation, chelating ligands, on the contrary, increase the rate of hydrolysis and polycondensation giving nanoparticles, formed by oxo-clusters (core) containing *acac* ligands on the surface (shell), that exhibit a typical structure of micelles. The stabilization of sol is obtained as a consequence of the interfacial activity of these micelles.<sup>22</sup> Therefore, it is very important to choose a suitable *Hacac*/Zr molar ratio ( $\rho$ ) value. Using an appropriate  $\rho$  value, the formation of a homogeneous gel at room temperature, occurs. On the contrary, when the *Hacac* is not used, the instantaneous precipitation of a particulate gel occurs. It should be emphasized that when  $\rho$  is equal to 4 the formation of Zirconium(IV) 2,4-pentanedionate, Zr(*acac*)<sub>4</sub>, occurs. This is the more stable Zr-acetylacetonate complex at room temperature, as it contains fully saturated eight-coordinate Zr<sup>4+</sup> in a square antiprismatic structure.<sup>27,28</sup>

It has recently been shown by Weiss et al.<sup>24</sup> that in this complex the interfacial activity of *acac* ligands is not sufficient to prevent the hydrolysis and polycondensations.

Consequently, when the *Hacac* is used to control the reactivity of a zirconium alkoxide, the  $\rho$  value must be properly optimized according to the chemical species that are present in the reaction medium and, in any case, it must be far from the  $\text{Zr}(\text{acac})_4$  stoichiometric one.<sup>29</sup>

Aronne et al.<sup>30</sup> have synthesized a class II  $\text{ZrO}_2$ -*acac* hybrid material in which *Hacac* was used in the sol-gel synthesis with a suitable *Hacac*/Zr molar ratio ( $\rho$ ) value in order to control the reactivity of the zirconium precursor, zirconium(IV) propoxide ( $\text{Zr}(\text{OPr})_4$ ). *Acac* ligands are strongly anchored to the zirconium oxo-oligomeric clusters forming the wet gel, even after the hydrolysis step.

This material was tested in removal and degradation of phenantrene, polycyclic aromatic hydrocarbon (PAH). This class of materials exhibits high stability and low water solubility due to the delocalization of  $\pi$ -electrons, leading to their accumulation in food chains, so threatening human health and environment quality. In addition, they are present in air, soil and waters; therefore, the removal of PAHs and the development of effective strategies to remediate polluted sites is a current focus of research in the environmental science. In the last decades many attempts have been made to remove PAHs from the environment.

Photocatalysis by either solar energy or artificial light has emerged as one of the most attractive strategies for their degradation.

With the aim to implement the potentiality of the hybrid Zr-based systems, part of my research activity was devoted to the preparation of  $\text{ZrO}_2$ -*acac* gel-derived (HSGZ) material according to the synthesis procedure used by Aronne et al.<sup>30</sup> In these conditions, a highly homogeneous porous material in which the functionalities are extended to whole bulk material at the atomic scale, was obtained. In order to better understand the high stability of this complex, a detailed thermal and structural characterization was investigated, by different performing techniques.

In addition, this material was tested in the oxidative degradation of four different phenoxy herbicides (2-methyl-4-chlorophenoxyacetic acid (MCPA), 4-(4-chloro-2-methylphenoxy)butanoic acid (MCPB), 4-chlorophenoxyacetic acid (4-CPA) and 2,4-dichlorophenoxyacetic acid (2,4 D)) and a two-steps kinetic model has been proposed to evaluate their removal.

Finally, in order to clarify the mechanism of action of this catalyst, the physic-chemical properties were investigated by using suitable spectroscopic techniques, such as electron paramagnetic resonance (EPR). The promising results about the striking capability of this

material to catalyze oxidative degradation reactions in absence of light and without any thermal pretreatment are later reported.

### ***Niobium-based inorganic mixed oxides***

- *Nb<sub>2</sub>O<sub>5</sub>-SiO<sub>2</sub> materials*

Niobium based materials synthesized by the sol-gel method have attracted great interest for their potential applications such as heterogeneous acid catalysts<sup>31-33</sup> especially when a high acidity and water tolerance are needed (e.g. epoxidation, esterification, dehydration and hydrolysis reactions),<sup>34-36</sup> supports for biomolecule immobilization<sup>37</sup> and energetic materials.<sup>38</sup>

Niobium pentoxide (also known as niobic acid when fully hydrated) represents the most studied oxide of niobium. It has a crystalline nature and a low surface area; therefore, when it is employed for catalytic purposes, it must be supported on suitable supports in order to obtain a final material characterized by a high specific surface area.

Therefore, the crystallization behavior of the niobium pentoxide supported both on siloxane matrix<sup>39,40</sup> and on silica-alumina<sup>41</sup> has attracted interest. In fact, different niobium surface species (isolated or bulk) can be formed depending on the nature and properties of the support material as well as niobium precursors, niobium content and synthesis method.

The suitable choice of molecular precursors with a comparable hydrolysis rate is of critical importance to obtain a homogeneous gel. Tetraethoxysilane (TEOS), or alkylalkoxysilane and niobium (V) ethoxide, Nb(OC<sub>2</sub>H<sub>5</sub>)<sub>5</sub>, or niobium chloride, NbCl<sub>5</sub>, are the most used as silicon and niobium source, respectively.

Niobium ions (Nb<sup>5+</sup>) in aqueous environment, undergo rapid hydrolysis giving rise to a precipitate of hydrated niobium pentoxide, Nb<sub>2</sub>O<sub>5</sub>·nH<sub>2</sub>O. To prevent this phenomenon, the use of chelating agents, such as ethylenediaminetetracetic, citric and malic acids, 2,4-pentanedione, acetylacetone or organic epoxides, represents a viable strategy.<sup>38,42,43</sup>

The complex chemical behavior of niobium ions makes possible to obtain materials with different structural characteristics using slight differences in the synthesis procedure.

Francisco and Gushikem<sup>31</sup> prepared Nb<sub>2</sub>O<sub>5</sub>-SiO<sub>2</sub> composites using TEOS and NbCl<sub>5</sub> as molecular precursor of silicon and niobium, respectively. The synthesis procedure employed, require both the TEOS prehydrolysis and a suitable amount of HCl to obtain

gelation. In addition, they have operated under a N<sub>2</sub> atmosphere at high temperature to have a slow solvents evaporation.

Drake et al.<sup>34</sup> synthesized Nb<sub>2</sub>O<sub>5</sub>-SiO<sub>2</sub> mixed oxides using niobium ethoxide as niobium source. In this case, TEOS prehydrolysis is employed to have a homogenous gel, too. The complete removal of solvents is obtained under vacuum for 24 h. These authors showed that the structure of the gels at low Nb<sub>2</sub>O<sub>5</sub> contents (~ 3.0 and 7.5 % at.) did not give Nb–O–Nb bonds but all niobium is uniformly distributed throughout the siloxane network. These bonds were found only in the gel with a higher amount of Nb<sub>2</sub>O<sub>5</sub> (~ 30 % at.) showing that the structure of this sample is phase separated on the atomic scale containing domains of Nb<sub>2</sub>O<sub>5</sub> and SiO<sub>2</sub>.

Carniti et al.<sup>44</sup> produced Nb<sub>2</sub>O<sub>5</sub>-SiO<sub>2</sub> systems using the method proposed by Drake et al. with the addition of a defined amount of tetrapropylammonium hydroxide ((C<sub>3</sub>H<sub>7</sub>)<sub>4</sub>-OH, TPAOH, 20 mass % in water) to obtain a complete gelation.

In the last years, Aronne et al.<sup>40</sup> also synthesized Nb<sub>2</sub>O<sub>5</sub>-SiO<sub>2</sub> mixed oxides by sol-gel route. They obtained homogeneous gels operating in air at room temperature using TEOS and NbCl<sub>5</sub> as silicon and niobium source, respectively, without addition of complexing agents. The procedure employed is innovative with respect to the ones previously reported in the lack of TEOS prehydrolysis and the absence of specific agent adopted to speed up the gelation. In addition, the hydrochloride acid (HCl) is employed because it acts both as catalyst and as complexing agent of the Nb<sup>5+</sup> ion allowing to obtain transparent chemical gels at room temperature with high niobium dispersion.

The experimental data carried out by Aronne et al.<sup>40</sup> showed that the different niobium loading did not affect significantly the gelation time but strongly influenced the microstructure of the gel-derived samples. Actually, the progressive increase of niobium content favors the self-condensation of niobium oxo oligomers with respect to the cross-condensation. Specifically, increasing the niobium content (~ 20 % at.), the formation of niobia and silica nanodomains will be favored in the gel structure. In contrast, for materials containing a lower amount of niobium (~ 2.5 % at.), the cross-condensation prevails producing a homogeneous dispersion of niobium in the siloxane matrix. Therefore, the degree of niobium dispersion is strongly influenced by the Nb/Si ratio. This ratio influences the niobium coordination in the matrix and the tendency towards crystallization as well.

The surface acidic properties of the  $\text{Nb}_2\text{O}_5 \cdot \text{SiO}_2$  systems depend on the composition of the material which in turn determines the kind of  $\text{NbO}_x$  species bonded to silica:  $\text{NbO}_4$  tetrahedra,  $\text{NbO}_6$  octahedra with a different distortion degree and niobia clusters.

$\text{NbO}_4$  or  $\text{NbO}_6$  isolated species prevail at low Nb content while clustering of  $\text{NbO}_6$  octahedra with the disappearance of  $\text{NbO}_4$  tetrahedra occur at higher Nb content.<sup>40</sup>

A schematic representation of octahedral and tetrahedral units is shown in Figure I-2.

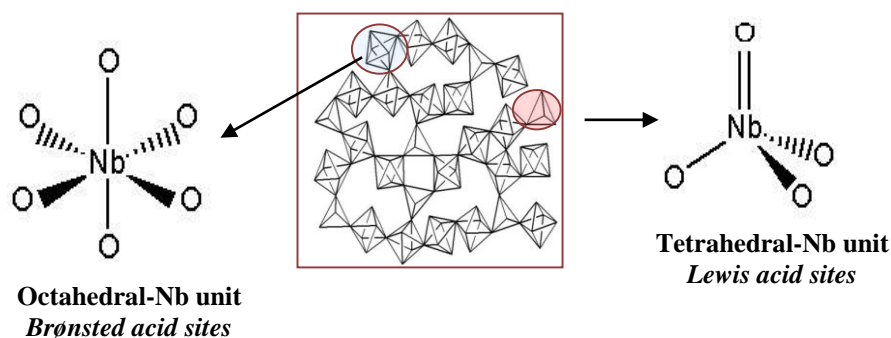


**Figure I-2.** Schematic representation of acid site Nb unit.

The presence of different  $\text{NbO}_x$  surface species interacting with the siloxane matrix can give rise to different acid sites: Brønsted and Lewis acid sites.<sup>35,45</sup>

Brønsted acid sites (proton donors) can be formed on oxide-based solid acid catalysts when protons balance net negative charges introduced by substituting cations with a lower valence charge or by partial reduction of neutral oxide clusters. Alternatively, Lewis acid sites form from coordinatively unsaturated cationic sites, which leave the metal ions ( $\text{M}^{n+}$ ) exposed to interact with guest molecules as an acceptor of an electron pair.<sup>46</sup>

The effective availability of these acid sites is mainly affected by Nb dispersion that strongly depend on the synthesis procedure.

The catalytic performance of the niobium oxide-based materials can be controlled by modulating the distribution and the relative amount of Lewis and Brønsted acid sites by regulating the structure and in turn, the preparation method.

Part of my research activity was devoted to investigate the influence of the preparation procedure on the structure and the properties of  $\text{Nb}_2\text{O}_5 \cdot \text{SiO}_2$  materials containing about the same  $\text{Nb}_2\text{O}_5$  amount (19 % wt.) but obtained by different synthetic routes with special attention to their catalytic activity in the epoxidation of methyl oleate with hydrogen peroxide.

- *Ru/RuO<sub>2</sub>@Nb<sub>2</sub>O<sub>5</sub>-SiO<sub>2</sub> materials*

Nowadays, increasing energy demands coupled with decreasing reserves of fossil resources (non-renewable) has led to increasing interest in the use of biomass based raw materials as an energy source.<sup>47</sup>

Biomass is an inexpensive, renewable, and abundant source of carbon which can be converted to liquid, solid and gaseous fuels and fine chemicals. Biomass-based platform molecules are important bridges linking biomass raw materials and target products. Therefore, utilization of biomass to produce valuable biofuels and feedstock chemicals is one of the promising alternatives to the current petroleum-based chemical industrial technologies.<sup>48,49</sup> The development of simple, efficient and cost-effective processes for the preparation of platform molecules and their further conversion to fuels and chemicals are crucial to the improvement of the competitiveness of biomass resources relative to fossil resources.

Lignocellulosic biomass is the most abundant class of biomass consisting of three main components: cellulose, hemicellulose and lignin.<sup>50</sup>

Cellulose can be converted into glucose by chemical or enzymatic hydrolysis and can be used to produce ethanol, platform chemicals, such as levulinic acid (LA) and 5-hydroxymethylfurfural (HMF), and liquid fuels.

Hemicellulose is an amorphous polymer consisting of C5 and C6 sugars. It is more reactive than cellulose, is easier to remove from lignocellulosic biomass, and is typically associated with the production of xylitol, furfural, and furfural derivatives.

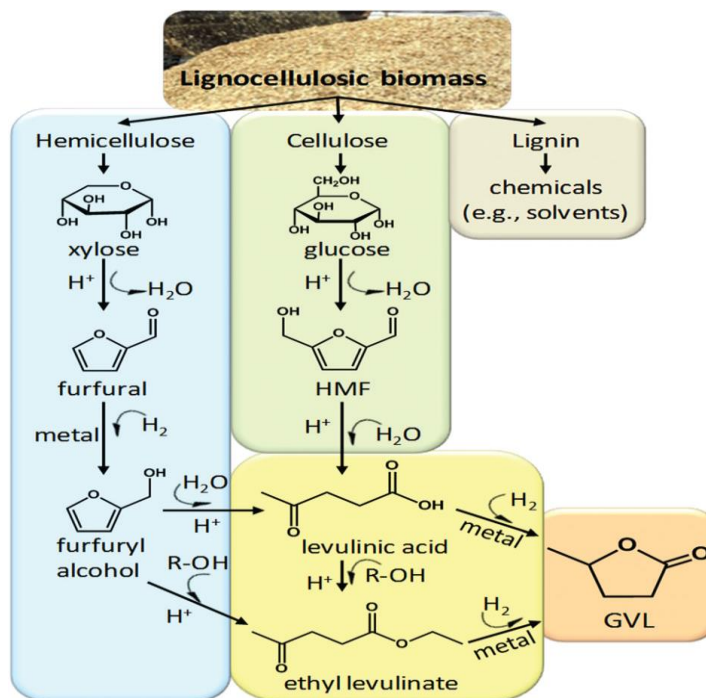
The final component of lignocellulosic biomass is lignin, an amorphous polymer rich in aromatic monomers.<sup>51</sup>

One of the main challenges in converting lignocellulosic biomass is producing chemicals or fuels at high selectivity and yields at economical costs.

Single-step methods, like pyrolysis, rely on high temperatures to deconstruct the lignocellulosic biomass and lead to lower costs due to the lack of pretreatment steps, excluding drying and size reduction. Additional costs are required, however, for the downstream separations.

To control the reactivity and improve selectivity, two-step processing methods are typically employed. These methods first fractionate the lignocellulosic biomass into its main components (hemicellulose, cellulose and lignin) which allows for processing each fraction at different conditions to achieve high yields of target products. The highly functionalized and reactive molecules (mainly C6 and C5 sugars) are processed at mild

conditions to obtain intermediate molecules (Scheme S- I.2), which are less reactive than the original sugars and therefore, more stable, yet they have enough functionality to be used as building blocks to produce a variety of chemicals and fuels depending on the necessities of the market.<sup>51</sup>



**Scheme S-I.2.** Fractionation of lignocellulosic biomass and reaction pathways to produce GVL from hemicellulose and cellulose.

According to the U.S. Department of Energy, in 2004, one of the most promising building blocks is levulinic acid (LA). It can be produced (in combination with formic acid) from cellulose, starch, or C6 sugars by acid hydrolysis through 5-hydroxymethylfurfural (5-HMF) as an intermediate, and from hemicellulose in a 3 step process through furfural and furfuryl alcohol as intermediates (Scheme S-I.2) at low cost.

Additionally, furfuryl alcohol and LA can be esterified with ethanol to produce ethyl levulinate. The ethyl levulinate and LA can then be hydrogenated to  $\gamma$ -valerolactone (GVL) which has excellent properties as solvent and is a precursor for high value chemicals and fuels. Being able to upgrade both the cellulose and hemicellulose to LA and then to GVL improves the economics of converting biomass, leading researchers to find more uses for these chemicals and more efficient processing methods. Recently, the transformation of LA into GVL has extensively studied and heterogeneous Ru-based

catalysts resulted active and selective for this reaction especially under aqueous phase conditions.<sup>52-58</sup> Although very high conversion and selectivity was found using activated carbon supported ruthenium (Ru/C) catalysts, they suffer from continuous deactivation during recycling. To overcome this inconvenient different supports have been explored such as Al<sub>2</sub>O<sub>3</sub> together with acid co-catalysts<sup>52</sup>, Al<sub>2</sub>O<sub>3</sub><sup>52-54</sup>, hydroxyapatite<sup>55</sup>, TiO<sub>2</sub><sup>53,56</sup>, ZrO<sub>2</sub><sup>57</sup>, Zr-SiO<sub>2</sub><sup>49</sup>, SiO<sub>2</sub><sup>53</sup>, and a few layer of grapheme<sup>58</sup> even if the deactivation of catalyst seems to be still an unresolved problem especially for reaction occurring in an upflow packed bed reactor<sup>53</sup>. Two deactivation modes were proposed: the irreversible one, related to the sintering of the metal nanoparticles, and the reversible one the source of which appears still unclear<sup>53</sup>.

To date, most used procedures to synthesize these catalysts are wet impregnation and the sol-gel route.<sup>49,59-61</sup>

Jansat et al.<sup>59</sup> have prepared RuO<sub>2</sub>@SiO<sub>2</sub> materials using hybrid mesostructured silica matrix functionalized with phosphonate groups to foster anchoring of the metal precursor inside the pores of the matrix. These materials were synthesized by more impregnation/hydrogenation cycles. Zhang et al.<sup>60</sup> have prepared nanoparticulate (NP) RuO<sub>2</sub> loaded into a commercial mesoporous silica. Lo et al.<sup>61</sup> have synthesized various SiO<sub>2</sub> : RuO<sub>2</sub> ratios by a wet chemical method using a preformed mesoporous silica matrix as template for metal precursor. More recently, Kuwahara et al.<sup>49</sup> have dispersed and stabilized ruthenium nanoparticle (NP) in Zr-containing spherical mesoporous silicas. Particularly, the supported Ru NP catalyst was synthesized by a conventional impregnation method and a following reduction treatment in a flow of H<sub>2</sub>. Then, the support was dispersed in aqueous solution containing the metal source. To facilitate the incorporation of the Ru(III) ions into the support, vacuum conditions was applied. These are only some examples of RuO<sub>2</sub>@SiO<sub>2</sub> nanomaterials synthesized by wet routes.

An alternative synthetic approach succeeds in the preparation of Ru/RuO<sub>2</sub>@SiO<sub>2</sub> nanocomposites via a co-synthesis sol-gel process, leading to the simultaneous formation of the matrix and metal-ion doping. Matura et al.<sup>62</sup> have produced Ru/SiO<sub>2</sub> and RuO<sub>2</sub>/SiO<sub>2</sub> hybrid nanomaterials with size-controlled ruthenium nanoparticles as elemental bricks. This route takes advantage of the organometallic approach and the use of a bifunctional ligand as metal precursor and a stabilizer for the synthesis of ruthenium nanoparticles. Tristany et al.<sup>63</sup> have synthesized a composite ruthenium-containing silica nanomaterials starting from amine stabilized-ruthenium nanoparticles as elemental bricks.

Therefore, bifunctional ligands act both as nanoparticle stabilizers and as sol-gel promoters.

However, both these methods are complicated, need a strictly controlled atmosphere, present several reaction steps with unknown yields, are energy/time consuming and use toxic or pollutant reactants. Therefore, it is of great significance to develop efficient and inexpensive supported metal catalysts, which can achieve the selective conversion of LA to GVL under mild conditions and the subsequent conversion of GVL.

Part of my research activity was focused on the preparation of new ruthenium-based bifunctional catalyst, which can realize the transformation of LA to GVL in one-pot.

Ru/RuO<sub>2</sub>@Nb<sub>2</sub>O<sub>5</sub>•SiO<sub>2</sub> mixed oxide was obtained by an innovative sol-gel route wholly performed at room temperature and characterized by both easy handling of precursors and the lack of toxic or pollutant reactants.

The mixed oxide matrix (Nb<sub>2</sub>O<sub>5</sub>•SiO<sub>2</sub>) containing a nominal amount of Nb<sub>2</sub>O<sub>5</sub> equal to 10.2 % wt., was selected in order to realize a material that can act as bifunctional catalyst exhibiting both acidic and redox functionalities. Furthermore, the choice of the acidic Nb<sub>2</sub>O<sub>5</sub>-SiO<sub>2</sub> matrix offers the possibility to modulate the strength of the different acid sites exhibiting both strong Brønsted acid sites and Lewis acid sites of moderate strength<sup>35,36</sup>. Therefore, this system should exhibit both acidic and redox functionalities in order to favor both the hydrogenation and the acid catalyzed steps in one-pot.

Ru/RuO<sub>2</sub>@Nb<sub>2</sub>O<sub>5</sub>-SiO<sub>2</sub> nanomaterials were characterized by structural and morphological analysis and were tested in the hydrogenation of LA to GVL when this reaction was carried out under mild conditions and in aqueous environment in a fed batch reactor.

The key factors controlling the catalyst efficiency are the selectivity, reproducibility and longtime stability. These characteristics are satisfied only if the synthesis procedure allows obtaining homogeneous dispersion, efficient immobilization of the active phase inside the host matrix and high surface area. Here, the surface area and the morphological characteristics of materials were controlled adding different amounts of a nonionic surfactant (polyethylene glycol hexadecyl ether, Brij-C10) directly in the starting solution of precursors. In this way, the surfactant can act both as pore-directing agent and as oxygen-rich complexing agent of the metallic species. This approach can elegantly reduce the number of processing steps and the operating cost. The influence of Brij-C10 incorporation on porous structure, size and dispersion of ruthenium nanoparticles were investigated in detail.

## PUBLICATIONS

### Publications included in this PhD thesis

#### *Papers*

1. Muñoz-García, A. B.; Sannino, F.; Vitiello, G.; Pirozzi, D.; Minieri, L.; Aronne, A.; Pernice, P.; Pavone, M.; D'Errico, G., Origin and Electronic Features of Reactive Oxygen Species at Hybrid Zirconia-Acetylacetonate Interfaces, *ACS Applied Materials & Interfaces*, **2015**, 7, 21662-21667.
2. Sannino, F.; Pernice, P.; Minieri, L.; Camandona, G. A.; Aronne, A.; Pirozzi, D.; Oxidative Degradation of Different Chlorinated Phenoxyalkanoic Acid Herbicides by a Hybrid ZrO<sub>2</sub> Gel-Derived Catalyst without Light Irradiation, *ACS Appl. Mater. Interfaces*, **2015**, 7, 256-263.
3. Turco R.; Aronne A.; Carniti P., Gervasini A.; Minieri L.; Pernice P.; Tesser R.; Vitiello R.; Di Serio M., Influence of preparation methods and structure of niobium oxide-based catalysts in the epoxidation reaction, *Catalysis Today*, **2015**, 294, 99-103.
4. Minieri, L.; Esposito, S.; Russo, V.; Bonelli, B.; Di Serio, M.; Aronne, A.; Silvestri, B., Sol-Gel Synthesis of Ru/RuO<sub>2</sub>@Nb<sub>2</sub>O<sub>5</sub>-SiO<sub>2</sub> Nanomaterials as Effective and Reusable Bifunctional Catalysts in the Aqueous-Phase Hydrogenation of Levulinic Acid, submitted on *ACS catalysis*.

#### *Conferences*

5. Minieri, L.; Turco, R.; Gervasini, A.; Carniti, P.; Pernice, P.; Aronne, A.; Esposito, S.; Di Serio, M., Preparation of niobium-silicon mixed oxides nanocomposites as catalyst for epoxidation reaction, *IX Workshop Sol-Gel*, Parma, Italy, 17-18 June 2014.
6. Minieri, L.; Sannino, F.; Pernice, P.; Pirozzi, D.; Imperato, C.; D'Errico, G.; Vitiello, G.; Aronne, A., Hybrid ZrO<sub>2</sub>-acetylacetonate gel-derived material as catalyst for pollutants removal, *VI Workshop Nazionale AICInG*, Rome, Italy, 22-23 June 2015.

## Publication not included in this PhD thesis

### *Papers*

7. Sannino F.; Pernice P.; Imperato C.; Aronne A.; D'Errico G.; Minieri L.; Perfetti M.; Pirozzi D., Hybrid TiO<sub>2</sub>-acetylacetonate amorphous gel derived material with stably adsorbed superoxide radical active in oxidative degradation of organic pollutants, *RSC Advances*, **2015**, 5, 93831-93839.
8. Pirozzi, D.; Abagnale, M.; Minieri, L.; Pernice, P.; Aronne, A., In-situ modified sol-gel process for the development of a monolith continuous microreactor for enzymatic green reactions, submitted on *Chem. Ing. J.*

### *Conferences*

9. Aronne, A.; Sannino, F.; Pirozzi, D.; D'errico, G.; Vitiello, G.; Minieri, L.; Pernice, P., Synthesis of hybrid ZrO<sub>2</sub>-acetylacetonate gel-derived catalyst for oxidative degradation of organic pollutants, *IX Workshop Sol-Gel*, Parma, Italy, 17-18 June 2014.
10. Turco, R.; Di Serio, M.; Tesser, R.; Minieri, L.; Pernice, P.; Aronne, A., Methyl esters epoxidation catalyzed by novel niobium oxide based materials, *VI Workshop Nazionale AICIng*, Rome, Italy, 22-23 June 2015.
11. Russo, V.; Minieri, L.; Tesser, R.; Aronne, A.; Di Serio, M., Ru-based catalysts for  $\gamma$ -valerolactone synthesis, *XIX Congresso Divisione Chimica Industriale*, Salerno, Italy, 14-16 September 2015.

# **CHAPTER 1**

## **SOL-GEL**

## 1.1 Sol- gel technology

The sol-gel technology allows to prepare ceramic and glass materials involving the transition from a sol to a solid gel phase.<sup>12,64-66</sup>

The *sol* is a colloidal suspension of solid particles in the range of 1...100 nm and takes place by hydrolysis and polycondensation reactions of metal alkoxide compounds or inorganic metal salts as starting materials. Polycondensation reactions induce growth of oligomers which begin to impinge on one another forming bonds at random: the *gel*. Therefore, a *gel* is an interconnected, rigid network with pores of sub micrometer dimensions and polymeric chains whose average length is greater than a micrometer.

The term *gel* embraces a diversity of combinations of substances that can be classified in four categories as discussed by Flory:<sup>67</sup>

- (i) well-ordered lamellar structures;
- (ii) covalent polymeric networks, completely disordered;
- (iii) polymer networks formed through physical aggregation, predominantly disordered;
- (iv) particular disordered structures.

At the moment that the gel forms, many clusters will be present in the sol phase and, only with the time, they progressively become connected to the network and the stiffness of the gel will increase. In other words, the gel appears when the last link is formed between two large clusters to create the spanning cluster. This link is responsible for the onset of elasticity by creating a continuous solid network. Therefore, the gel can be defined as a substance containing a continuous solid skeleton enclosing a continuous liquid phase. The “gel point” is reached when a “spanning cluster” appears extending throughout the sol.<sup>12,64,65</sup>

Compared with other synthesis methods, the sol-gel technique offers many advantages, among them:<sup>12</sup>

- the low process temperature;
- the ability to control the composition on molecular scale;
- the porosity to obtain materials with high surface area;
- the homogeneity of the final product up to atomic scale.

It allows modulating microstructure, morphological and textural properties of the final materials by means of the processing parameters (i.e. monomer concentration, water/alkoxide molar ratio, temperature, pH of the reaction medium).<sup>12,68,69</sup> It is possible

to synthesize complex composition materials, to form higher purity products through the use of high purity reagents, and to provide coatings over complex geometries.<sup>12,64,65</sup> Moreover, the sol-gel process is a versatile wet chemical process to make ceramic and glass materials not only as bulk samples but also in a wide variety of forms: ultra-fine or spherical shaped powders, thin film coatings, ceramic fibres, microporous inorganic membranes, monolithics, or extremely porous aerogels. Thin films can be produced by spin-coating or dip-coating.

When the sol is cast into a mold, a wet gel will form. By suitable treatment, the wet gel can be converted in lot of forms:

- *xerogel (dried gels)*, obtained to evaporation of the liquid in a wet gel under normal conditions giving a volume 5 to 10 times smaller of the original gel volume;
- *aerogel materials*, with a highly porous and extremely low density, produced by removal of the solvent in a wet gel under supercritical condition, in autoclave;
- *dense ceramic or glass materials*, generated by successive thermal treatments;
- *ceramic fibers*, drawn adjusting the viscosity of the sol into a suitable viscosity range;
- *ultra-fine and uniform ceramic powders*, formed by precipitation, spray pyrolysis, or emulsion techniques.

An overview of the sol-gel process is illustrated in Figure 1.1

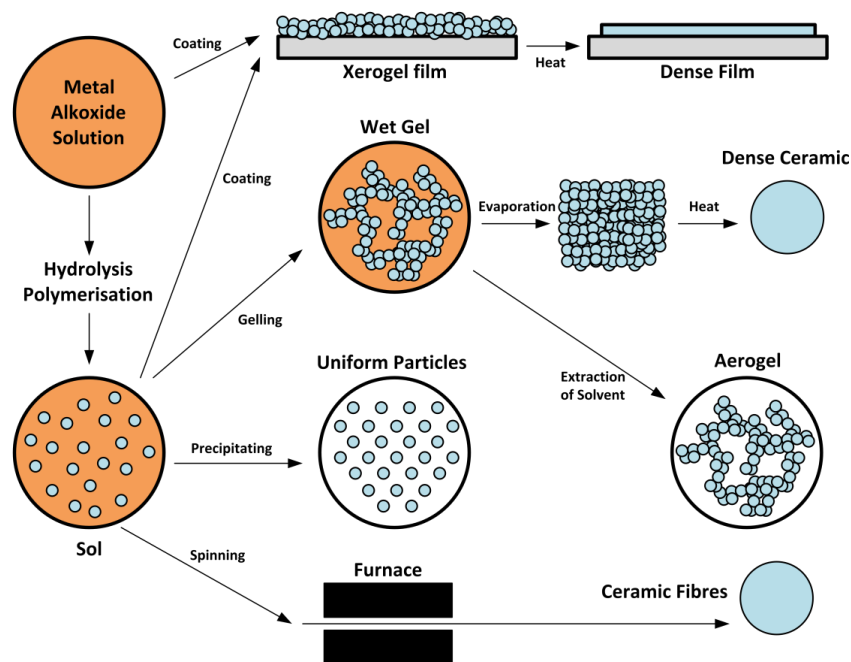


**Figure 1.1.** Schematic representation of the sol-gel process and its products.

For mixed-oxides this synthesis procedure allows obtaining materials characterized by a high dispersion of the minor component in the matrix of the major phase on both molecular and nanometer scale.<sup>31,34,37,39,40</sup>

## 1.2 Sol-gel chemistry

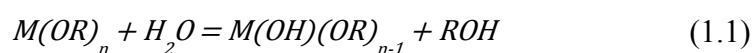
Metallic alkoxides are the starting reagents more commonly used. Their general formula is the following:  $M_x(OR)_y$ , where M represents the element with valence y and R is the alkoxide group. These alkoxides must exhibit useful properties to control the chemical synthesis of oxides as:

1. *easy to purify*, a lot of alkoxides can be distilled in order to obtain highly pure products;
2. *wide variety of R*, it is possible to choice R among a large number of alkylic groups in order to obtain the required reactivity during hydrolysis and polycondensation reactions;
3. *wide variety of mixed alkoxides*, as a further tool to control the stoichiometry and the homogeneity of the final products.

For multi-component systems, the choice of the molecular precursors plays a key role in the synthesis procedure. Actually, in order to obtain homogeneous sols, suitable molecular precursors with comparable hydrolysis rates should be used. In this way, cross-linking between clusters of different components with similar size will take place allowing gelation instead of precipitation and/or co-precipitation. In the former case, gels formed by permanent covalent bonds (chemical gels) are obtained; while in the latter, particulate gels, i.e. gels where temporary or reversible bonds connect the clusters, can be achieved (physical gels).<sup>40</sup>

The sol-gel transition involves two key steps, hydrolysis and polycondensation. Generally, hydrolysis takes place by the addition of small amounts of water. Moreover, when the precursors are insoluble in water, non-aqueous solvents such as alcohols, are added in reaction medium to form a homogeneous solution.

In the hydrolysis reaction, the alkoxide groups (OR) are replaced stepwise by hydroxyl groups (OH) by nucleophilic substitution ( $S_N$ ):<sup>70</sup>



The hydrolysis rate is determined by many factors. Indeed, it is facilitated by the increase of the charge density on the metal, of the number of metal ions bridged by an hydroxo-ligand (M-OH) or oxo-ones (M=O), and of the number of hydrogens contained in the ligand.<sup>71,72</sup>

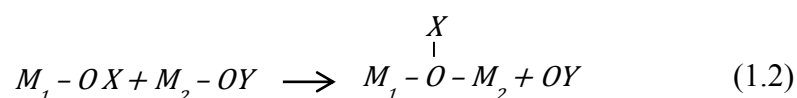
Conversely, hydrolysis is inhibited when the number of hydroxo-ligands coordinating M increases. Therefore, in these conditions, the reverse reaction occurs. The temperature, the pH, the different amount of solvent, the water/metal alkoxide molar ratio (*r* values) could influence the hydrolysis reaction, too.

Due to high oxygen electronegativity compared to metal, the M-OR bonds are highly polarized giving fast hydrolysis rate. Therefore, by increasing the number of OR groups (hard- $\pi$  donors), the stabilization of the highest oxidation state of M occurs making it more susceptible to nucleophilic attack. On the contrary, the hydrolysis rate of non-metal-oxygen bonds (e. g., in silicon alkoxides, Si(OR)<sub>4</sub>) is slower. In fact, the lower electronegativity difference between the non-metal and the oxygen originates a lower partial positive charge on the non-metal decreasing its electrophilic character. This effect makes the non-metal more stable toward hydrolysis, condensation and other nucleophilic reactions. The control of hydrolysis rate is very important when multi-component systems (mixed oxides) are prepared. In fact, the choice of molecular precursors with comparable hydrolysis rates plays a key role in obtaining of homogeneous sols in which cross-linking are preferred to self-ones.

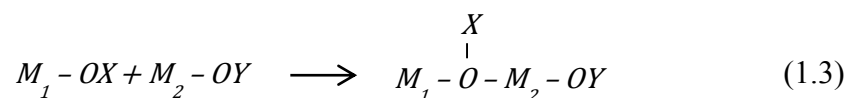
Many solutions can be adopted with the aim to obtain cross-linking, such as:

- modifying the hydrolysis rate of the more reactive precursor *via* inhibitors;
- using double alkoxides, with precise stoichiometry;
- changing the hydrolysis rate of the slower precursor by a catalyzed pre-hydrolysis (acid or basic).

Condensation reactions can proceed by either of two nucleophilic mechanisms depending on the coordination of the metal. When the preferred coordination is satisfied, condensation occurs by nucleophilic substitution (S<sub>N</sub>):



When the preferred coordination is not satisfied, condensation can occur by nucleophilic addition (A<sub>N</sub>):



with an attendant increase in the coordination number of  $M_2$  occurs. Both reactions, require that the coordination of oxygen increase from 2 to 3. Moreover, the creation of the additional bond involves a lone pair electron on oxygen and the bond formed may or not be equivalent to the other two bond.

According to the “partial charge model” (two atoms combine to form a charge transfer so that each atom acquires a partial positive or negative charge), three different predominant species can be obtained with suitable characteristics:

- in the high-pH/high-z domain, oxo-ligands contained in oxy-ions  $[MO_N]^{(2N-z)-}$  ( $N$  is the coordination number and  $z$  is the oxidation state) are good nucleophiles but poor leaving groups. In these conditions, condensation occurs by addition when at least one of the reactant species is coordinatively unsaturated (maximum  $N$  value is less than the  $z$  one).

- In the low-pH/low-z domain, aquo-ligands in aquo-ions  $[M(OH_2)_N]^{z+}$  are good leaving groups but poor nucleophiles. Condensation does not occur since no attacking group is present.

- At intermediate pH and  $z$  values, hydroxo-ions  $[M(OH)_N]^{(N-z)-}$  contain both good nucleophiles (O or OH) and good leaving groups ( $H_2O$  or OH). In these conditions, condensation occurs as soon as one OH is present in the coordination sphere of M.

In Figure 1.2., the charge *versus* pH diagram displays the “aquo”, “hydroxo” and “oxo” domains.

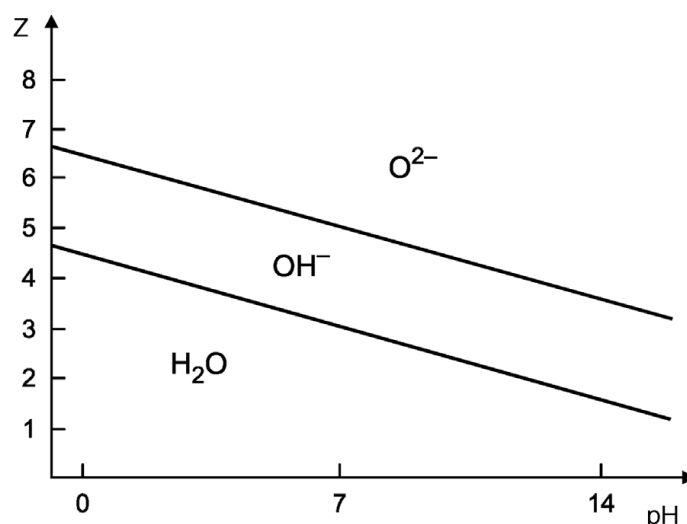


**Figure 1.2.** Charge versus pH diagram indicating the “aquo”, “hydroxo” and “oxo” domains.

When the coordination number ( $N$ ) of the metal is greater than the charge of the metal ( $z$ ) ( $N-z > 0$ ), the condensation can occur by *olation* during which the formation of hydroxyl bridge between two metal center takes place. For coordinately saturated hydroxo-aquo precursors, olation occurs by an  $S_N$  mechanism where the hydroxyl group is the nucleophile and  $H_2O$  is the leaving group. Therefore, the kinetics of olation is related to the ability to dissociate of the aquo ligand, which depends on size, electronegativity and the electronic configuration of metal ( $M$ ).

The condensation reactions can also occur by *oxolation* in which an oxo bridge ( $-O-$ ) is formed between two metal centers. When the metal is coordinately unsaturated, oxolation occurs by nucleophilic addition ( $A_N$ ); while, for coordinately saturated metals, oxolation proceeds by a two-step  $S_N$  reaction between oxyhydroxy precursors involving nucleophile addition followed by water elimination to form a  $M-O-M$  bond.

Compared to olation, oxolation occurs over a wider range of pH, but due to the two-step process, kinetics is slower and never diffusion-controlled.

The thermodynamics of these reactions is governed by:

- the strength of the entering nucleophile;
- the electrophilicity of the metal;
- the partial charge and stability of the leaving group.

Instead, the kinetics depends on:

- the extent of coordination under saturation of the metal ( $N-z$ );
- the transfer ability of the proton.

Therefore, larger values of (N-z) and greater acidities of the protons reduce the activation barriers and enhance the kinetics.

Another factor that influences reaction kinetics is the extent of oligomerization (molecular complexity) of the metal alkoxides. The molecular complexity depends on both the nature of the metal atom and alkoxide ligand. The hydrolysis rate decreases with the alkyl chain length consistent with the steric effect expected for an associative  $S_N$  reaction mechanism. The alkyl chain also influences the morphology (particle size and surface area) and the crystallization behavior of the resulting gel.

The hydrolysis and condensation rates are influenced on acid or base catalysis. Acid catalysts can be used to protonate negatively charged alkoxide groups, producing a good leaving groups. The resulting polymers are more extended and less branched. On the contrary, alkaline conditions produce strong nucleophiles via deprotonation of hydroxo ligands (-OH) leading to more compact and highly branched species. Different gel structures are reported in Figure 1.3.

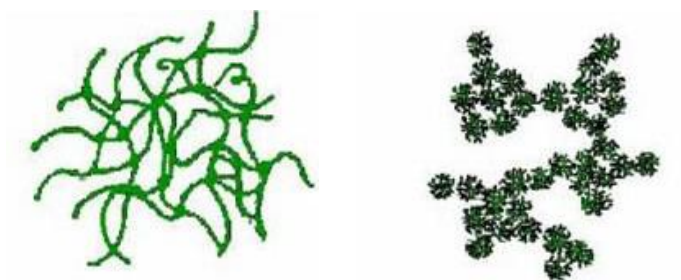


**Figure 1.3.** Gel structure: cross-linked linear chains (on the left); branched clusters (on the right).

The choice of the solvent also influences the kinetics and the resulting structure. Generally, the formation of alkoxy-bridging occurs in nonpolar and aprotic solvent allowing the hydrolysis control with the formation of homogeneous gels; whereas, a rapid hydrolysis occurs in polar and protic solvent giving highly condensed product and precipitates.<sup>12,73</sup>

The gel structures can be defined as “strong” or “weak” according to whether the bonds, connecting the solid phase, are permanent or reversible.

The point where the gel shows the highest elasticity is defined “time of gelation”,  $t_{gel}$ , at which corresponds a specific value of viscosity ( $\eta$ ). The “time of gelation” depends on many factors, among them: the ratio water/alkoxide,<sup>74,75</sup> temperature,<sup>76,77</sup>

concentration<sup>75,78</sup> and size of the alkoxide.<sup>79,80</sup> When all these values increase, the time of gelation decrease. Generally,  $t_{gel}$  decreases by factors that increase the condensation rate. After gelation, the chemical reaction carries on in the period called “aging” of the gel. During the aging process, therefore, many changes occur in the structure and properties of gels. These changes can be categorized as:<sup>12,66</sup>

- *Polymerization*, is the increase in connectivity of the network produced by condensation reactions which occur for months at room temperature;
- *Syneresis*, is shrinkage of the gel network resulting in expulsion of liquid from the pores. This process is caused by the same condensation reactions that produce the gelation;
- *Coarsening or ripening*, is a process which consists in the growth of particles in aqueous conditions starting from aggregates restructured through dissolution-precipitation in order to form larger and more stable particles, thereby consuming the small primary particles.

Finally, to obtain a xerogel, the wet gel must be subjected to specific heating treatments to avoid changing the structure of the synthesized material. The removal of solvent occurs in several phases; initially, it is carried out with a constant evaporation rate during the which the volume reduction is evident. In this phase, some cracks can be formed. Then, the evaporation rate is carried on more slowly due to capillary pressure into pores caused by several factors, such as the different temperature in and out material, the surface tension and the vapor pressure.

### **1.3 Role of organic ligands**

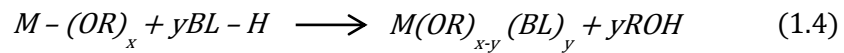
The choice of the molecular precursors plays a key role in the synthesis procedure. They should have a comparable hydrolysis rates in order to obtain homogeneous sols. Frequently, the reactivity of silicon and metal alkoxides towards water have to be controlled, in order to achieve cross-linking between clusters of different components instead of precipitates. For this purpose, chemical additives can be added during synthesis procedure.

Metal alkoxides show a higher reactivity than silicon alkoxides, due to both their lower electronegativity compared to silicon and to their coordination number higher than their valence. Therefore, metal alkoxides are Lewis acids and they can interact with compounds having a lone pair of electrons (Lewis bases) to achieve higher coordination number. While catalysts are often needed to enhance the reactivity of silicon alkoxides in

sol-gel processes, chemical additives are used to moderate the reactivity of metal alkoxides.<sup>81</sup>

In recent years, the reactivity of zirconium alkoxides,  $Zr(OR)_4$ , has been studied. These species show a very high reactivity toward the hydrolysis-condensation reactions due to the high polarity of Zr-O bond which in turn generates a positive partial charge on the zirconium atom, making it very susceptible to nucleophilic attack. Therefore, the use of bidentate (bridging or chelating) complexing ligands (BL), was frequently employed with the aim to control the hydrolysis reaction rate of zirconium precursors avoiding the development of a particulate gel.<sup>16,82</sup>

Particularly, when a metal alkoxide  $M(OR)_x$  is reacted with acetic acid or acetylacetonate (BL-H), a fraction of the alkoxide groups is substituted by acetate or acetylacetonate groups. A new molecular precursor  $M(OR)_{x-y}(BL)_y$  is obtained with a different structure and a lower reactivity.<sup>81</sup>



The metal compounds  $M(OR)_{x-y}(BL)_y$  are coordination compounds (metal complexes), the stability of which is determined by the equilibrium constant  $K$ , called also “stability constant”. The higher the stability constant, *i.e.*, the more the equilibrium is shifted to the product side, the more stable is the metal complex with respect to ligand elimination reactions. Multidentate ligands are more strongly bonded than the corresponding monodentate ligands because of the chelate effect. In this conditions, the stability constant of the corresponding complexes is much higher. As a result of the stronger bonding, multidentate ligands are less readily hydrolyzed than the remaining OR groups upon sol-gel processing. Although a partial cleavage of the metal-BL bond normally cannot be avoided due to the coordination equilibrium mentioned above, a substantial proportion of the BL can be retained in the obtained gels. The replacement of one or more OR groups by BL has several chemical and structural consequences for sol-gel processing apart from the fact that the new precursor  $M(OR)_{x-y}(BL)_y$  has a different reactivity. The chemical and structural consequences during sol-gel process can be reported as following:<sup>81</sup>

- the degree of crosslinking of the gel network is decreased, because of the smaller proportion of hydrolyzable OR groups;
- the substitution of monodentate alkoxy group by bi- or multidentate BL lowers the connectivity of the molecular building blocks. This favors the formation of gels instead of crystalline precipitates;

- the polarity change by the organic groups has probably a similar effect on the network structure as changing the polarity of the solvent;
- the complexing ligands may stereochemically direct the hydrolysis and condensation reactions because the site *trans* to an organic group has a different reactivity than the *cis* sites.

Besides controlling the reactivity of the metal alkoxides and the network structure of the obtained gels, the bidentate ligands can also be used to introduce functional organic groups into gels by means of appropriately substituted derivatives.<sup>16</sup>

As matter of fact, when methacrylic acid is used instead of acetic acid to modify a metal alkoxide, the coordination of the carboxylate group to the metal, i.e., the chemical environment of the metal, is the same. However, the material obtained by sol-gel processing contains organic functionalities (polymerizable double bonds in the case of methacrylate) tethered to the metal via the carboxylate group. In the other hand, the possibility to introduce organic functionalities into metal-based sol-gel materials by using organofunctional BL is an important innovation.

A first mechanism proposed to explain the sol stabilization, is based on the hypothesis that a kinetic control is exerted by the modifying chelating ligand on hydrolysis and polycondensation reactions of metal alkoxide. According to this mechanism, chelating ligands block the coordination sites of ions such as  $Ti^{4+}$ ,  $Zr^{4+}$ , decreasing their rate of hydrolysis and Polycondensation.<sup>11,16,19,20</sup>

A more recent interpretation has been suggested by Kessler et al.,<sup>22,83</sup> and supported by papers recently published about the reactivity of titanium and zirconium alkoxides.<sup>23,24</sup> Kessler et al. have shown that the hydrolysis and polycondensation of these metal alkoxides are facilitated by the chemical modification and their kinetics has no direct relation to the sol-gel transformation of metal alkoxides. Therefore, the whole process of *sol* formation is directed by the self-assembly of ligands. According to this, chelating ligands increase the rate of hydrolysis and polycondensation giving nanoparticles, formed by oxo-clusters (*core*) containing chelating ligands on the surface (*shell*), that exhibit a structure typical of micelles. Therefore, the oxo-alkoxide molecules formed, serve apparently as nuclei for the formation of larger aggregates that become phase separated and can be referred to as *Micelles Templated by Self-Assembly of Ligands*.

The stabilization of sol is obtained as a consequence of the interfacial activity of these micelles.<sup>22</sup>

#### 1.4 Role of surfactant agent

Surfactant agent allows to control over the greater and finer structure of a material. A sacrificial template, which acts as a support around which the final material is built before being removed, is commonly used for the preparation of materials with a specified outer structure as well as a predetermined inner arrangement. Numerous porous materials are fabricated using surfactants to provide control over the inner porous structure.

The use of these agents to form macroporous solids has recently gained attention from the research community. The final structures exhibit some resemblance to the initial template and generally show properties that could not be achieved without the structure directing agent.<sup>84</sup>

Surfactants act as pore-directing agents within the sol-gel process due to their amphiphilic nature, allowing them to spontaneously orient themselves in such a way that the contact between the solvent and the hydrophobic group of the surfactant is minimized, thereby decreasing the free energy of the system.<sup>85,86</sup> As a result, the surfactant is often regarded as a “spacer” within the sol-gel, and can enable the production of highly porous materials with a specific pore structure and size.

Among the several surfactants employed in the making materials, Brij<sup>®</sup> are very used. They are di-block copolymers that have been infrequently used in sol-gel literature not only as pore-directing agents to modulate the morphological characteristics of the final material but also as oxygen-rich complexing agent of the metallic species.

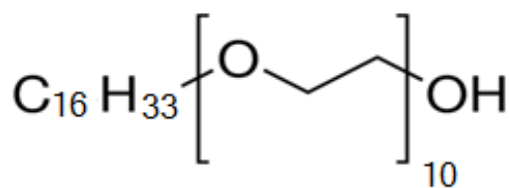


**Figure 1.4.** Structural representation of Brij-C10 surfactant.

## **CHAPTER 2**

### **EXPERIMENTAL SECTION**

## 2.1 ZrO<sub>2</sub>-acetylacetonate (HSGZ)

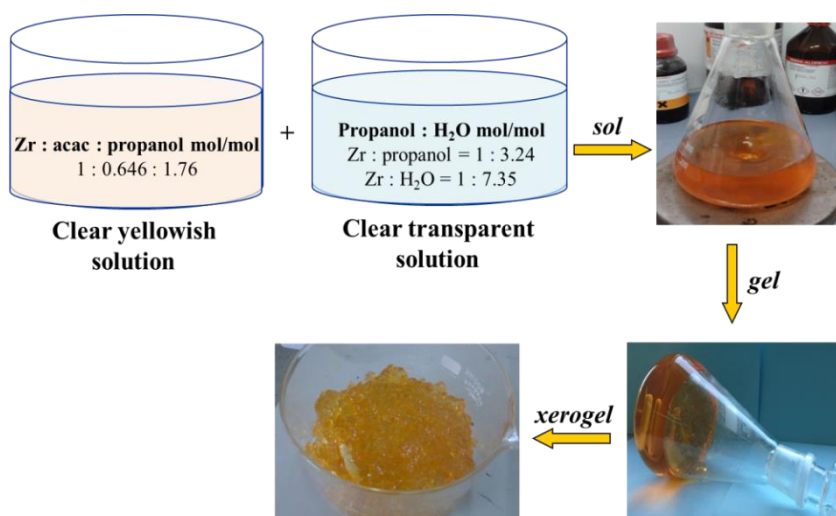
**Materials.** Zirconium (IV) propoxide (70 wt.% in 1-propanol), acetylacetonate (C<sub>5</sub>H<sub>8</sub>O<sub>2</sub> > 99%), and 1-propanol (C<sub>3</sub>H<sub>8</sub>O > 99.80%) were purchased by Sigma-Aldrich (Milan, Italy).

4-Chloro-2-methylphenoxyacetic acid (MCPA), 4-chlorophenoxyacetic acid (4-CPA), 2,4 dichlorophenoxyacetic acid (2,4-D), and 4-(4-chloro-2-methylphenoxy)butanoic acid (MCPB) were purchased by Sigma-Aldrich Chemical Co. (Poole, Dorset, UK; 99.0% purity).

**Sol-gel synthesis.** A yellowish solution containing 10 mL (22.6 mmol) of zirconium (IV) propoxide, 1.5 mL (14.6 mmol) of acetylacetonate (*Hacac*), and 3.0 mL of 1-propanol (39.9 mmol) was prepared and stirred at room temperature for a few minutes. A second clear solution containing 3.0 mL (166 mmol) of distilled water and 5.5 mL (73.2 mmol) of 1-propanol was added to the first one.

The resulting Zr : *Hacac* : propanol : water molar ratio was 1 : 0.646 : 5 : 7.35. The yellowish solution obtained was vigorously stirred until the gelation that occurred in a few minutes at room temperature. A homogeneous slightly yellow colored gel was obtained. The gel was left at room temperature for 2 days and then dried at 30 °C without lyophilization in vacuum at -50 °C for 20 h, giving a porous amorphous *xerogel* (HSGZ). Powders, accurately sieved in order to obtain a granulometric distribution ranging from 63 to 90 μm, were selected to perform the kinetic tests.

A scheme step by step of the synthesis procedure is following reported:



**Scheme 2.1.** Scheme step by step of the synthesis procedure.

**Thermogravimetric (TG) and Differential Thermal Analyses (DTA).** To study the reactions occurring during xerogels heating, we carried out TG-DTA analyses, using a TA Instruments SDT Q 600. The TG and DTA tests were performed keeping 20–25 mg of xerogel under nitrogen atmosphere, varying the temperature from 20 to 1000 °C. A heating rate of 10 °C min<sup>-1</sup> was adopted.<sup>87</sup>

**X-ray diffraction (XRD).** The amorphous nature of the dried gels as well as the nature of the crystallizing phases were ascertained by X-ray diffraction (XRD) with a Philips X'PERT-PRO diffractometer by using monochromatized CuK $\alpha$  radiation (40 mA, 40 kV) with a step width of 0.013° 2 $\theta$ .<sup>87</sup>

**Fourier transform infrared (FTIR) spectroscopy.** The structure of the HSGZ matrix, as well as its structural evolution during the heating, was studied by Fourier Transform InfraRed (FTIR) spectroscopy.

FTIR spectra of dried and heat-treated gel samples were carried out at room temperature by a Nicolet system, Nexus model, equipped with a DTGS KBr (deuterated triglycine sulfate with potassium bromide windows) detector.

The absorption spectra were recorded in the 4000–400 cm<sup>-1</sup> range with a spectral resolution of 2 cm<sup>-1</sup> on samples diluted in KBr. The spectrum of each sample represents an average of 64 scans, which were corrected for the spectrum of the blank KBr. Moreover, FTIR spectrum of HSGZ after repeated batch tests in the presence of 0.2 mmol L<sup>-1</sup> of MCPB solution was recorded at room temperature, as reported in literature.<sup>87</sup>

**Ultra violet and visible light diffuse reflection (UV-vis DR) spectroscopy.** Ultra violet and visible light diffuse reflection (UV-vis DR) spectra were recorded in the range of 200-800 nm on a doubled beam Jasco spectrophotometer.

Barium sulfate was used as a reflectance standard. The measured intensity was expressed as the value of the Kubelka-Munk function F(R).<sup>88</sup>

**Electron Paramagnetic Resonance (EPR) spectroscopy.** The powder sample was analysed using a X-band (9 GHz) Bruker Elexys E-500 spectrometer (Bruker, Rheinstetten, Germany). The capillary containing the sample was placed in a standard 4 mm quartz sample tube. The temperature of the sample was regulated at 25 °C and maintained constant during the measurement by blowing thermostated nitrogen gas through a quartz Dewar.

The instrumental settings were as follows: sweep width, 100 G; resolution, 1024 points; modulation frequency, 100 kHz; modulation amplitude, 1.0 G; time constant, 20.5 ms. EPR spectra were measured with attenuation of 10 dB to avoid microwave saturation of

resonance absorption curve. Several scans, typically 64, were accumulated to improve the signal-to-noise ratio.

The  $g$  values were evaluated by means of two internal standards (1,1-diphenyl-2-picrylhydrazyl (DPPH) and a 4-hydroxy-2,2,6,6-tetramethylpiperidin-1-oxyl (TEMPOL) ethanol solution) which were inserted in the quartz sample tube co-axially with the capillary containing the HSGZ sample.<sup>88</sup>

**Analytical Determination of herbicides.** MCPA, 4-CPA, 2,4-D and MCPB herbicides were analyzed with an Agilent 1200 Series HPLC apparatus (Wilmington U.S.), equipped with a DAD and a ChemStation Agilent Software. A Macharey-Nagel Nucleosil 100-5 C18 column (stainless steel 250 × 4 mm) was utilized.

In the case of MCPA, the mobile phase composed of a binary system of 50:50 acetonitrile: phosphate buffer (0.1%, pH 2.5) was pumped at 1 mL min<sup>-1</sup> flow in isocratic mode. The detector was set at 225 nm.

MCPB was analyzed using the previously described conditions, except of the eluent system which is composed by a binary system of 60:40 acetonitrile: phosphate buffer (0.1%, pH 2.5).

For 2,4-D and 4-CPA, the mobile phase formed by a binary system of 40:60 acetonitrile: phosphate buffer (0.1%, pH 2.5) was pumped at 1 mL min<sup>-1</sup> flow in isocratic mode. The detector was set at 283 nm.

For all chosen herbicides, the injection volume was 20 µL.

The quantitative determination was performed using a calibration curve for each herbicide investigated. The following concentration ranges were adopted: 0.0002-0.9 mmol L<sup>-1</sup>, 0.0001-0.2 mmol L<sup>-1</sup>, 0.0002-2.7 mmol L<sup>-1</sup>, and 0.0002-2.0 mmol L<sup>-1</sup>, for MCPA, MCPB, 4-CPA and 2,4-D, respectively.<sup>87</sup>

**Removal Tests of herbicides by HSGZ Matrix.** A stock solution of each herbicide was prepared by dissolving in 500 mL of Milli-Q ultrapure water the following amounts:

- 100 mg of MCPA (final concentration 0.9 mmol L<sup>-1</sup>);
- 22 mg of MCPB (final concentration 0.2 mmol L<sup>-1</sup>);
- 250 mg of 4-CPA (final concentration 2.7 mmol L<sup>-1</sup>);
- 250 mg of 2,4-D (final concentration 2.0 mmol L<sup>-1</sup>).

The obtained solutions were subsequently kept refrigerated.

All the experiments were carried out in batch conditions in the dark, in a thermostatic rotary shaker at 30 °C. Blanks of each herbicide in aqueous solution were analyzed in order to check the pesticide stability and the possible sorption to vials.

After incubation, the samples were centrifuged at 7000 rpm for 20 min and the supernatants were analyzed as above-reported.

Kinetic experiments were performed incubating about 1 mg of HSGZ matrix with 1 mL of each herbicide (solid/liquid ratio (R) was 1.0) at 0.2 mmol L<sup>-1</sup> concentration for different incubation times (0.25, 0.5, 1.0, 2.0, 3.0, 4.0, 5.0, 6.0, 16, 24, 72 h) at 30 °C.

In order to clarify the effect of the herbicide concentration, kinetic tests were carried out, as above-reported, adopting for each herbicide concentration values close to solubility limits.

The experiments were conducted at R = 1.0 using solutions at 0.9, 0.2, 2.7, and 2.0 mmol L<sup>-1</sup> of MCPA, MCPB, 4-CPA, and 2,4-D, respectively, at 30 °C.

With the purpose to investigate the effect of HSGZ matrix amount, kinetic tests of MCPA removal were performed at 0.2 mmol L<sup>-1</sup> concentration and at R = 1.0, 2.0 (obtained by adding 4 mg of matrix in 2.0 mL of final volume), and 5.0 (obtained by adding 10 mg of matrix in 2.0 mL of final volume).

Finally, the long-term applicability of the MCPB-removal system was verified by carrying out repeated batch tests. After each batch test, the liquid phase was removed and replaced by an equal volume of MCPB solution at the initial concentration of 0.2 mmol L<sup>-1</sup>.

In conclusion, to investigate the stability of the catalyst, FTIR spectrum of HSGZ before and after repeated batch tests at room temperature was recorded.<sup>87</sup>

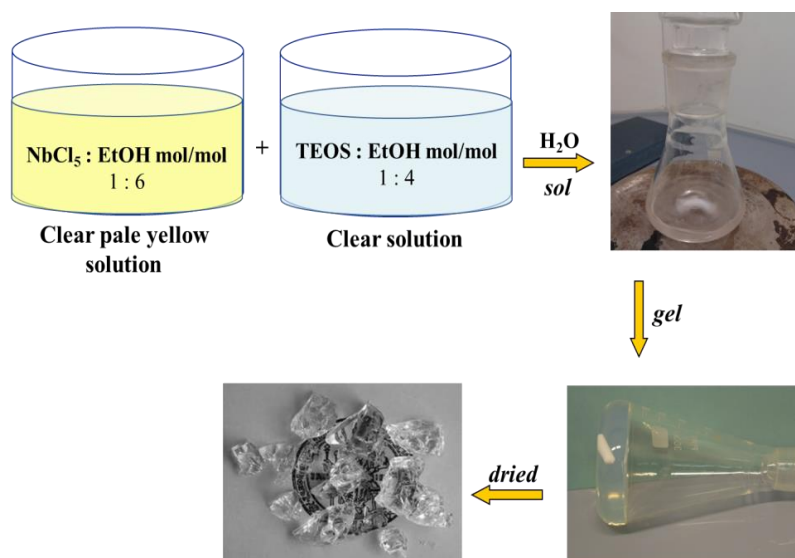
**Kinetic Models.** The removal kinetics of the four herbicides on the HSGZ were elaborated considering an alternative physico-mathematical model in which the first stage of the herbicide removal implied a reversible first-order adsorption on HSGZ surface following from degradation of them. All the experiments were carried out in triplicate and the relative standard deviation was lower than 4%.<sup>87</sup>

## 2.2 Nb<sub>2</sub>O<sub>5</sub>•SiO<sub>2</sub> and Ru/RuO<sub>2</sub>@Nb<sub>2</sub>O<sub>5</sub>•SiO<sub>2</sub>

**Materials.** Tetraethoxysilane (TEOS) (Si(OC<sub>2</sub>H<sub>5</sub>)<sub>4</sub> 99%, Sigma Aldrich), niobium (V) chloride, NbCl<sub>5</sub> (99%, Sigma Aldrich), anhydrous ethanol (EtOH) (Sigma Aldrich), Ruthenium (III) chloride-3-hydrate (RuCl<sub>3</sub>•3H<sub>2</sub>O 99.98%, Aldrich), polyethylene glycol hexadecyl ether (Brij-C10) (C<sub>16</sub>H<sub>33</sub>(OCH<sub>2</sub>CH<sub>2</sub>)<sub>10</sub>OH, Sigma Aldrich). Tetramethylsilane (TMS) (Si(CH<sub>3</sub>)<sub>4</sub> ≥ 99.0 %, Sigma Aldrich).

**Nb<sub>2</sub>O<sub>5</sub>•SiO<sub>2</sub> sol-gel synthesis.** A solution of NbCl<sub>5</sub> in anhydrous ethanol having a molar ratio NbCl<sub>5</sub> : EtOH = 1 : 6 was prepared in a dry box at room temperature. This solution was fluxed with dry-air for 20 min, to allow the HCl removal and the formation of partially substituted Nb(OEt)<sub>5-x</sub>(Cl)<sub>x</sub> species.

An alcoholic solution of TEOS with molar ratio TEOS : EtOH = 1 : 4 was stirred for about 5 minutes, and then mixed with the first one. The resulting clear solution was hydrolyzed, under stirring, at room temperature using a HCl hydro-alcoholic solution so to obtain the final TEOS : H<sub>2</sub>O : HCl = 1 : 4 : 0.01 molar ratio. A transparent gel was obtained from this final solution, with gelation occurring no later than 2 days. The gelled systems were kept for 2 days more at room temperature before drying. The gels were fully dried in air at 110 °C, in an electric oven for 3 days. The catalyst was obtained by finely grounding the hardened dry gel, and then calcining it at 400 °C for about 3 h. The final sample contained a nominal amount of Nb<sub>2</sub>O<sub>5</sub> equal to 18.9 % wt. Hereafter this sample will be indicated as Nb<sub>sgII</sub>.<sup>89</sup>



**Scheme 2.2.** Scheme step by step of the synthesis procedure.

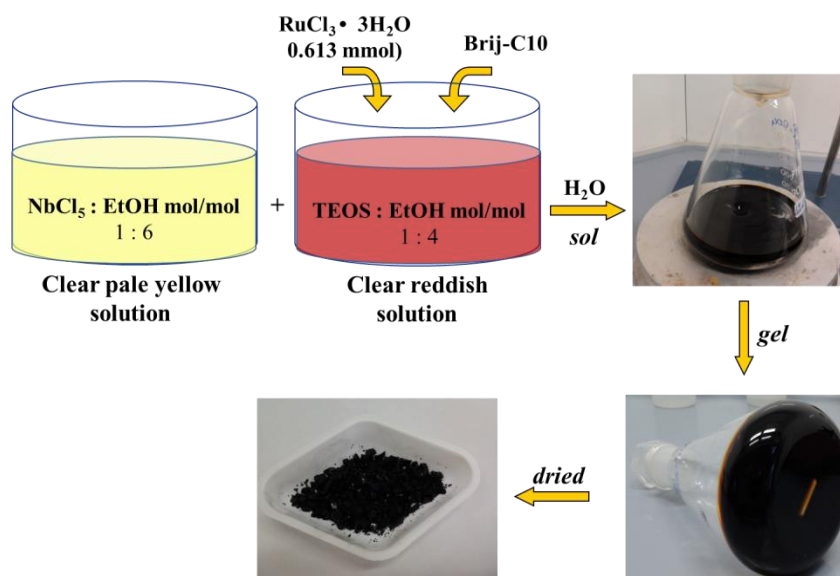
**Ru/RuO<sub>2</sub>@Nb<sub>2</sub>O<sub>5</sub>·SiO<sub>2</sub> sol-gel synthesis.** The materials were prepared by a suitable modification of the sol-gel route previously reported for the preparation of the matrix,<sup>89</sup> having a nominal composition that can be expressed by the formula (Nb<sub>2</sub>O<sub>5</sub>)<sub>0.025</sub>·(SiO<sub>2</sub>)<sub>0.975</sub>, by adding a proper amount of ruthenium in order to reach the 6.2 wt.% with respect to the matrix composition.

A solution of NbCl<sub>5</sub> in anhydrous ethanol (EtOH) having molar ratio NbCl<sub>5</sub> : EtOH = 1 : 6 was prepared in a dry box at room temperature. The solution was stirred for 20 min to allow the formation of partially substituted Nb(OEt)<sub>5-x</sub>(Cl)<sub>x</sub> species and the removal of HCl produced. An alcoholic solution of TEOS (Tetraethoxymethylsilane) with molar ratio TEOS : EtOH = 1 : 4 was prepared to which a proper amount of RuCl<sub>3</sub>·3H<sub>2</sub>O (0.613 mmol) was added and then mixed with the first one. The resulting clear reddish solution was hydrolyzed at room temperature using deionized water, finally obtaining a hydroalcoholic solution with the molar ratio TEOS : H<sub>2</sub>O = 1 : 4. From this final solution, a transparent reddish gel (RNS) was obtained within two days.

The porosity of the material was controlled by adding directly into the initial alcoholic solution of TEOS, a proper amount of polyethylene glycol hexadecyl ether (Brij-C10). Two different Brij-C10 : Si molar ratios were explored: 0.04 : 1 and 0.16 : 1. In both cases, the mixing of this solution with that of the niobium precursor gives rise to a clear reddish solution, the hydrolysis of which produced transparent reddish gels within two (0.04B-RNS) and five (0.16B-RNS) days, respectively.

The gelled systems were kept for 3 days at room temperature before drying, and afterwards they were fully dried in air at 110 °C in an electric oven until a constant weight was reached. After such treatments, amorphous hardened dry gels were obtained.

All samples were annealed for 2h at 500 °C in air and hereafter they will be noted as the acronym RNS-a, 0.04B-RNS-a and 0.16B-RNS-a. The heat-treatment was adopted to remove the template for gels containing Brij-C10.



**Scheme 2.3.** Scheme step by step of the synthesis procedure.

**X-ray diffraction (XRD).** XRD patterns of  $\text{Nb}_2\text{O}_5 \cdot \text{SiO}_2$  powders were recorded by using a Bruker 2D phaser with a  $\text{CuK}\alpha$  radiation of  $1.5418 \text{ \AA}$  (40 kV and 20 mA). A 2D range from  $5^\circ$  to  $80^\circ$  was scanned, at a velocity of  $0.02^\circ 2\theta \text{ min}^{-1}$ .<sup>89</sup>

The amorphous nature of Ruthenium-based dried gels as well as the nature of any crystalline phase formed at high temperature, were ascertained by XRD using a Philips diffractometer model PW1710 (Cu  $\text{K}\alpha$ ) at a scan rate of  $1^\circ \text{ min}^{-1}$ .

**Ultra violet and visible light diffuse reflection (UV–vis DR) spectroscopy.** Ultra violet and visible light diffuse reflection (UV–vis DR) spectra were recorded in the range of 200–800 nm on a doubled beam Jasco spectrophotometer.

Barium sulfate was used as a reflectance standard. The measured intensity was expressed as the value of the Kubelka-Munk function  $F(R)$ .<sup>89</sup>

**Fourier transform infrared (FTIR) spectroscopy.** Fourier transform (FT) IR spectra of dried and heat-treated gel samples were carried out at room temperature by a Nicolet system, Nexus model, equipped with a DTGS KBr (deuterated triglycine sulfate with potassium bromide windows) detector. The absorption spectra were recorded in the  $4000\text{--}400 \text{ cm}^{-1}$  range with a spectral resolution of  $2 \text{ cm}^{-1}$  using pressed disks of powders diluted in KBr (about  $200 \text{ mg} \times 1 \text{ cm}^2$ ). The spectrum of each sample represents an average of 64 scans, which were corrected for the spectrum of the blank KBr. To allow the comparison of the absorbance values, all FTIR spectra were normalized with respect to the maximum absorbance value recorded for each spectrum.<sup>89</sup>

**N<sub>2</sub> adsorption-desorption isotherms.** Nb<sub>2</sub>O<sub>5</sub>•SiO<sub>2</sub> powders were characterized by N<sub>2</sub> isotherms were obtained in an automatic analyzer (Sorptomatic 1900 instrument). The samples were previously treated in the sample cell at 350 °C under vacuum, up for 16 h up to complete degassing. Specific surface area (SSA) was calculated according to the BET (Brunauer-Emmett-Teller) method.<sup>89</sup>

Ruthenium-based powders were also characterized by N<sub>2</sub> adsorption at temperature of -196°C on *ca.* 100 mg sample previously outgassed at 300 °C for 3h to remove atmospheric contaminants (Quantachrome Autosorb 1 instrument). Specific surface area (SSA) was calculated both according to the BET (Brunauer-Emmett-Teller) method and through the Langmuir equation in the case of microporous samples. The pore size distribution (PSD) was calculated by applying the Non Local-Density Functional Theory (NL-DFT) method to isotherms adsorption branches, by applying a N<sub>2</sub>-silica kernel.

**Temperature Programmed Reduction (TPR) and Temperature Programmed Oxidation (TPO).** Ruthenium-based materials were characterized H<sub>2</sub>-TPR (Temperature Programmed Reduction) and O<sub>2</sub>-TPO (Temperature Programmed Oxidation) analysis, carried out on a TPD/R/O 1100 ThermoQuest instrument and using a 5% H<sub>2</sub>/Ar ( $Q=20\text{ cm}^3\text{ min}^{-1}$ ) or a 2% O<sub>2</sub>/He mixture ( $Q=40\text{ cm}^3\text{ min}^{-1}$ ), respectively, with heating rate of 10 °C min<sup>-1</sup>. The sample (100 mg) was loaded in a quartz down-flow cell with a K thermocouple in close contact with the sample.

**Morphological characterization: SEM-EDX and TEM.** Microstructure and chemical composition of the samples were investigated by NOVA/NANOSEM 450 FEI scanning electron microscopy (SEM), equipped with an energy dispersive X-ray analyzer (EDX) at an accelerating voltage of 30 kV.<sup>89</sup>

TEM observation of the Ruthenium-based samples was performed by transmission electron microscopy (TEM) - TECNAI G12 Spirit-Twin (LaB<sub>6</sub> source) equipped with a FEI Eagle 4k CCD camera, operating with an acceleration voltage of 120 kV.

**Thermogravimetric (TG) and Differential Thermal Analyses (DTA).** The weight loss of the Ruthenium-based gels as well as the nature and temperatures of the various reactions occurring during the heating were evaluated by a TA Instrument simultaneous thermoanalyser SDT Q600. The TG/DTA tests were carried out on 20 mg of dried gel specimens in N<sub>2</sub>, from room temperature up to 1000 °C heating rate of 10 °C min<sup>-1</sup>.

**Nb<sub>2</sub>O<sub>5</sub>•SiO<sub>2</sub> application: methyl oleate epoxidation.** The catalytic performance of the Nb<sub>2</sub>O<sub>5</sub>•SiO<sub>2</sub> materials was evaluated in methyl oleate epoxidation with hydrogen peroxide as oxidant. Epoxidation reactions were carried out in a round-bottom glass batch reactor,

put in an oil bath, equipped with a condenser and thermometer, and a magnetic bar for vigorous stirring (300 rpm). In a typical experiment, 600 mg of catalyst, 20 cm<sup>3</sup> of acetonitrile, 5 g of methyl oleate (25 mmol) and 6.9 g of hydrogen peroxide 54.9 % wt. (111 mmol) were used. The temperature was kept constant ( $\approx 80$  °C) with solvent refluxing. All reagents were added in one pot at the beginning of the reaction. The final solution was separated from the catalyst by decantation, and it was analyzed to evaluate the double bond conversion, through the determination of the *Iodine Number* (I.N.), and the epoxide yield, through the evaluation of the *Oxirane Number* (O.N.), according to the analytical methods reported in the literature.<sup>36</sup> The double bond conversions (C) have been determined as:

$$C(\%) = \frac{[I.N.]_i - [I.N.]_f}{[I.N.]_i} \times 100 \quad (\text{eq. 2.1})$$

The yields to epoxide (Y) have been determined as:

$$Y(\%) = \frac{[O.N.]_x [PM]_{1_2}}{[I.N.]_f \times [PM]_0} \times 100 \quad (\text{eq. 2.2})$$

where:

- I.N. is expressed as the grams of I<sub>2</sub> per 100 g of the oil;
- O.N. is expressed as the grams of epoxydic oxygen per 100 g of the oil;
- PM<sub>I<sub>2</sub></sub> is the molar weight of I<sub>2</sub> (g/mol);
- PM<sub>O</sub> is the molar weight of O (g/mol).

The selectivity (S) has been evaluated as:

$$S(\%) = \frac{Yield}{Conversion} \times 100 \quad (\text{eq. 2.3})$$

After all tests, the presence of residual hydrogen peroxide was evaluated. With respect to the initial content charged a residual amount ( $\approx 20\%$ ) was found indicating that in no case hydrogen peroxide was the limiting reagent. The leaching of the active species into the liquid phase under operating conditions has been verified removing the catalyst from the

reaction mixture by filtration after 150 minutes from the start of the reaction, and then recording the residual conversion for additional 150 minutes. For each catalyst almost no detectable subsequent conversion in the filtrate after removing the catalyst was observed, giving very strong evidence that these materials act as real heterogeneous catalysts.

**Ru/RuO<sub>2</sub>@Nb<sub>2</sub>O<sub>5</sub>·SiO<sub>2</sub> application: Levulinic Acid (LA) hydrogenation.** The catalytic performance of the Ru/RuO<sub>2</sub>@Nb<sub>2</sub>O<sub>5</sub>·SiO<sub>2</sub> materials was evaluated in levulinic acid (LA) hydrogenation to produce  $\gamma$ -valerolactone (GVL). The hydrogenation reaction was performed in a fed-batch reactor, where hydrogen is fed at constant pressure to a 0.3L vessel charged with about 4g of levulinic acid and 200g of water. Before loading the catalyst, it was prereduced in a dedicated system under a 0.1L/min hydrogen flow, 1bar and 300 °C of temperature for 3h. The catalyst so reduced, was cooled at room temperature under the same hydrogen flow and then charged quickly to the vessel. The reaction mixture, containing the catalyst, was then flushed with nitrogen at 5 bars, in order to evacuate the dissolved oxygen before feeding hydrogen. In this step, temperature was increased at the desired value (usually 70 °C), and the solution is stirred at 300 rpm. After about 10 washes, hydrogen was sent to the reactor at the desired pressure and the reaction starts. Periodical samples were withdrawn in order to evaluate the evolution with time of both LA conversion and GVL yield. An AISI 316 stainless steel net was installed at the bottom of the withdrawn pipe in order to avoid any catalyst loss. For each catalyst the reuse experiments have been made by performing cycles of 5 experiments the time during of which was 1.5 h. During the course of the reaction reagent/intermediate/product were analyzed by GC (see supplementary materials) every half hour according to a procedure followed described. Once the individual experiment, lasting 1.5h, was concluded, the catalyst was washed with distilled water and reused after filtration for a new experimental test performed in the same operating conditions as the previous. Adsorption tests have been performed by putting in contact either the reagent or the product with the catalyst at fixed temperature and stirring rate. Temperature and hydrogen flow were acquired thanks to a National Instruments DAQ device, while the acquisition software is homemade and written in LabView 2013.

**Analytical methods.** The withdrawn samples are analyzed via GC, using 1,3-propanediol as external standard. In particular, in about 2-4 cm<sup>3</sup> of samples, 100 $\mu$ L of standard are dissolved. 500 $\mu$ L of the solution were put in contact with 250 $\mu$ L of TMS for 45min at 90°C, as a derivatization procedure. The sample so prepared was injected to a Perkin Elmer Clarus 580 GC, with a Zebron ZB-WAX column (30m x 0.32mm x 0.25 $\mu$ m). The

injector is a PSSI, working at 250°C, with a carrier (He) pressure of 14psi and splitless configuration. The temperature ramp has been set as it follows: 150°C heating to 250°C with a rate of 20°C/min; temperature was kept at the final value for 25 minutes.

The retention times are here reported: TMS 5.7 min,  $\alpha$ -angelicolactone 11.1 min,  $\gamma$ -valerolactone 7.4 min, 1,3-propanediol 7.7 min and levulinic acid 11.3 min,  $\gamma$ -hydroxyvaleric acid 13.6 min.

## **CHAPTER 3**

### **RESULT AND DISCUSSION**

#### **PART 1**

### 3.1 ZrO<sub>2</sub>-*acac* hybrid material

ZrO<sub>2</sub>-acetylacetonate hybrid material (HSGZ) was prepared at room temperature by a sol-gel synthesis using suitable process conditions to produce a homogeneous chemical gel. HSGZ was obtained starting from zirconium(IV) propoxide whose reactivity was controlled using acetylacetonate (*Hacac*). This ligand plays a double role: *i*) as a complexing agent (for stabilizing the solution) and *ii*) reagent (i.e. constituent of the final hybrid material).

Depending on the employed *Hacac*/Zr molar ratio, different heteroleptic alkoxide-*acac* complexes were formed. These complexes stabilize the sol allowing to the formation of chemically homogeneous gels.

The final product can be considered a hybrid ZrO<sub>2</sub>-*acac* gel-derived material in which the organic ligands are strongly bounded to Zr<sup>4+</sup> ions.

Thermal and structural characterizations were carried out, as shown in the following paragraph.

### 3.2 Thermal and structural characterization

TG/DTA curves of HSGZ xerogel having a granulometric distribution ranging from 63 to 90 μm, recorded in nitrogen at 10 °C min<sup>-1</sup>, is displayed in Figure 3.1 together with the corresponding room temperature FTIR spectrum. These measurements were carried out to investigate the heating behavior of xerogel and its structural evolution.

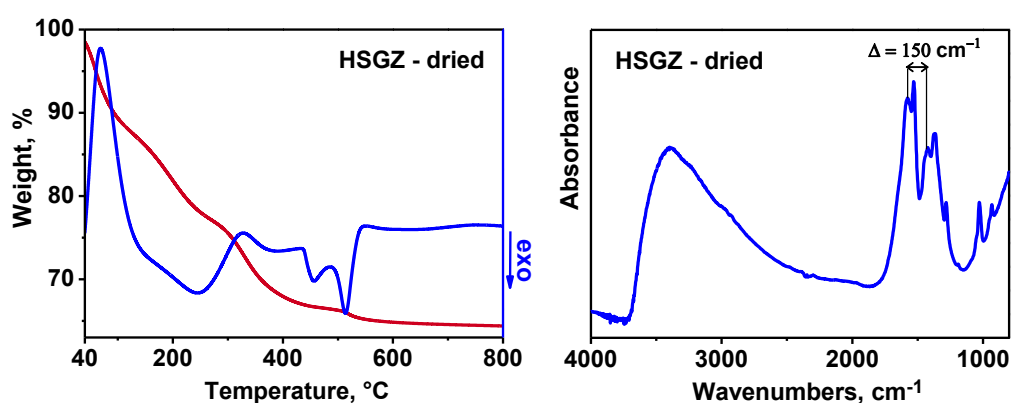


**Figure 3.1.** On the left: TG (red line)-DTA (blue line) curves recorded in nitrogen at 10 °C min<sup>-1</sup> of HSGZ as dried (HSGZ-dried). On the right, the corresponding room-temperature FTIR spectra.

TG curve (red line) of the HSGZ-dried exhibits an overall weight loss is about of 35 wt. % with three distinct inflection points in the range 25-400 °C (~58 °C, ~201 °C and ~332 °C) corresponding to three DTA endothermic peaks (blue line), where the former two are overlapped. Two unresolved DTA exothermic peaks at about 455 and 515 °C, instead, occur in the temperature range in which the zirconia crystallization takes place. In the corresponding TG curve an additional inflection point is also seen (~519 °C) even if it related to a very small weight loss (less than 2 wt. %).

The existence of  $ZrO_2$ -*acac* complex is confirmed by the analysis of the FTIR spectrum. Infrared spectroscopy is very useful technique to identify the two tautomeric forms of the *Hacac*. In solution at pH = 7, the tautomeric equilibrium between the keto and the enol forms is almost completely shifted in favor of the keto form. However, the enol form prevails in presence of a strong Lewis acid such as  $Zr^{4+}$  giving the formation of stable enol-type complexes in which the *Hacac* acts as bidentate chelating ligand. The two tautomers are easily distinguished by infrared spectra due to the delocalization of the double bonds occurring in the enol form. The presence of IR carbonyl bands of the enol form.<sup>23,90</sup> are indeed shifted at lower wavenumbers with respect to the ones of the keto form that are located at 1723 and 1697  $cm^{-1}$ . As a matter of fact, in FTIR spectrum of HSGZ-dried the asymmetric ( $\nu_{asy}$ ) and symmetric ( $\nu_{sym}$ ) stretching of C=O bonds of the carboxylate groups occur at 1575 $cm^{-1}$  and 1425 $cm^{-1}$ , respectively. The splitting ( $\Delta$ ) between these bands is 150  $cm^{-1}$ . According to Klepper et al.,<sup>91</sup> when the  $\Delta$  value lies in the 50–150  $cm^{-1}$  range a bidentate interaction between the ligand and  $Zr^{4+}$  occurs.

Other IR bands related to coordinated *acac* occur at 1530  $cm^{-1}$  (C=C stretching of enol groups,  $\nu_{C=C}$ ), 1376 and 1281  $cm^{-1}$  (stretching of delocalized C–O bond,  $\nu_{C-O}$ ) and at 1190  $cm^{-1}$  (C–H bending of  $CH_3$  groups,  $\delta_{CH_3}$ ). The presence of coordinated alkoxo or alcohol species is confirmed by the bands at the following: 2985 and 2932  $cm^{-1}$  (C–H stretching of methyl and methylene groups,  $\nu_{C-H}$ ), 1024  $cm^{-1}$  (rocking of  $CH_3$  groups,  $\rho_{CH_3}$ ), 930  $cm^{-1}$  (C–C skeletal stretching,  $\nu_{C-C}$ ), besides the broad band from about 3700 to 2500  $cm^{-1}$  centered at about 3400  $cm^{-1}$  (O–H stretching of interacting hydroxyl groups,  $\nu_{O-H}$ ). The absence of any bands and/or shoulders in the 1600–1700  $cm^{-1}$  range, where the H–O–H deformation mode ( $\delta_{HOH}$ ) of physisorbed and/or coordinated molecular water is active, and the low frequency of  $\nu_{O-H}$  indicate that the hydroxyl groups are involved in very strong H-bonding and that the formation of the enol-type complex with *acac* makes the solid HSGZ matrix very stable toward water and atmospheric moisture.<sup>30</sup>

To identify the nature of each DTA peak and to verify the stability of the  $ZrO_2-acac$  complex, different heat treatments were carried out on the dried sample by heating at  $10\text{ }^\circ\text{C min}^{-1}$  up to the required temperature and then quenching. Hereafter the samples will be noted as the acronym HSGZ followed by the heat-treatment temperature, i.e., HSGZ-250, HSGZ-400, HSGZ-480.

In Figure 3.2 are reported TG/DTA curves (on left) and FTIR spectra (on the right) of HSGZ-250.

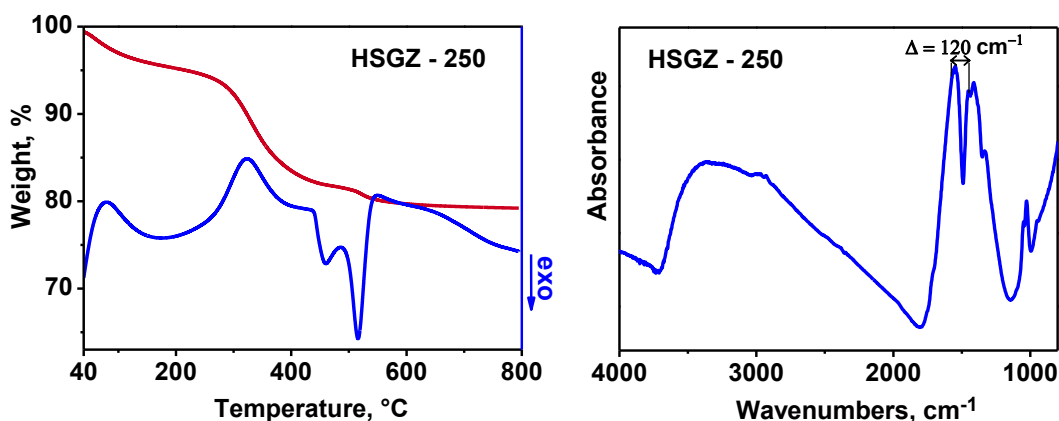


**Figure 3.2.** On the left: TG (red line)-DTA (blue line) curves recorded in nitrogen at  $10\text{ }^\circ\text{C min}^{-1}$  of HSGZ heating at  $250\text{ }^\circ\text{C}$  (HSGZ-250). On the right, the corresponding room-temperature FTIR spectra.

DTA curve (blue line) still exhibits a residual and low intensity endothermic peak at low temperature ( $\sim 80\text{ }^\circ\text{C}$ ), which is related to the loss of adsorbed water during the cooling at room temperature because of the porous nature of material. The DTA endothermic peak at about  $330\text{ }^\circ\text{C}$ , as well as the two DTA exothermic ones, remain unchanged. Therefore, by heating up to  $250\text{ }^\circ\text{C}$  the evaporation of water and alcohol physically trapped in the gels as well as the pyrolysis of organics originated during the gelation and the heating, take place.

In FTIR spectrum of HSGZ-250, the splitting value is still observed ( $\Delta = 120\text{ cm}^{-1}$ ). Therefore,  $ZrO_2-acac$  complex remains stable although the material is heated at high temperature. This result indicates that *acac* ligands are strongly bonded to the solid matrix giving a highly stable hybrid material. No other differences are visible in FTIR spectrum. TG/DTA and FTIR of HSGZ heated at  $400\text{ }^\circ\text{C}$  are shown in Figure 3.3.

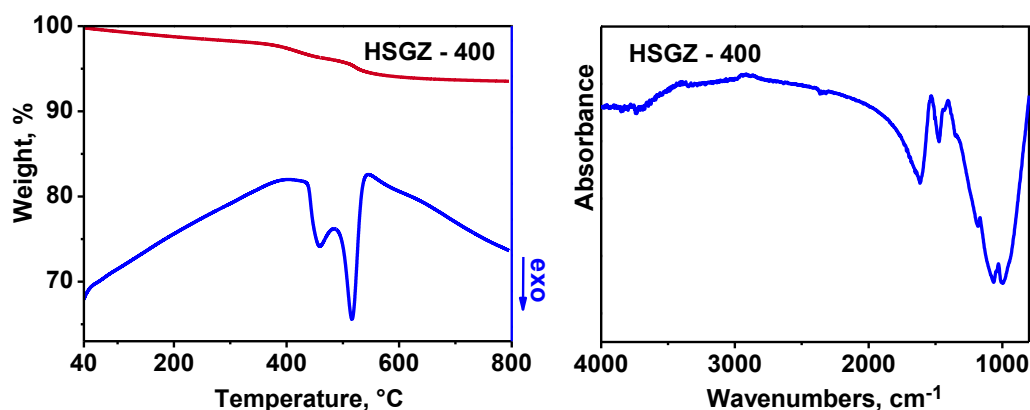


**Figure 3.3.** On the left: TG (red line)-DTA (blue line) curves recorded in nitrogen at 10 °C min<sup>-1</sup> of HSGZ heating at 400 °C (HSGZ-400). On the right, the corresponding room-temperature FTIR spectra.

The DTA curve of HSGZ-400 exhibits the loss of the endothermic peak at about 330 °C and only two exothermic peaks are shown at higher temperature mainly related to crystallization phenomena.

The FTIR spectrum does not exhibit the characteristic absorption bands related to  $\nu_{\text{asyC=O}}$  and  $\nu_{\text{symC=O}}$ . On the contrary, it shows two main absorption bands at about 1500 cm<sup>-1</sup> ( $\nu_{\text{C-C}}$ ) and 1440 cm<sup>-1</sup> ( $\delta_{\text{CH}_2}$ ), that are related to residual organics, allowing to state the lack of Zr-*acac* complexes at this stage, and consequently, to assign the DTA endopeak at about 330 °C, seen in the DTA curves of HSGZ and HSGZ-250, to the loss of the *acac* ligands. Additionally, this spectrum shows the disappearance of the broad band related to O-H stretching in the high frequency range with respect to the HSGZ spectra at lower temperature. This result can be considered as a consequence of the dehydroxylation reaction.

In Figure 3.4, TG-DTA curves and FTIR spectrum of HSGZ-480 are displayed.

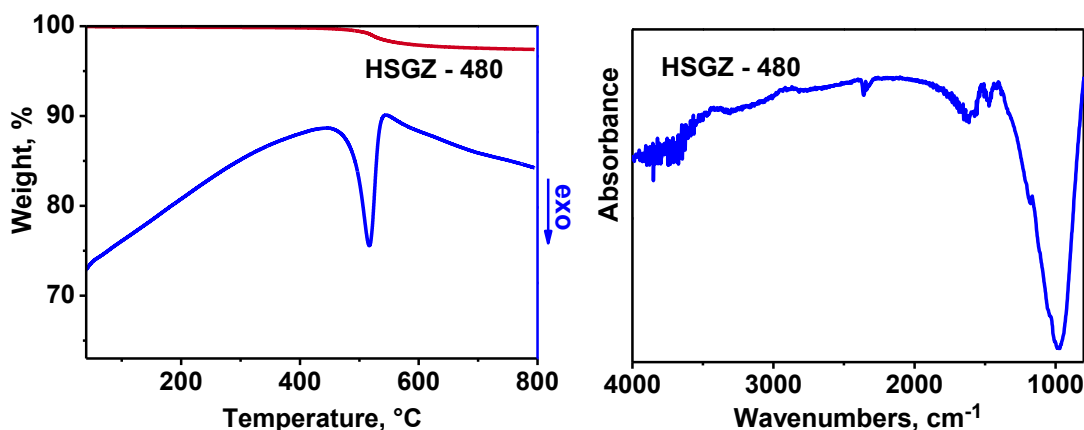


**Figure 3.4.** On the left: TG (red line)-DTA (blue line) curves recorded in nitrogen at  $10\text{ }^{\circ}\text{C}\text{ min}^{-1}$  of HSGZ heating at  $480\text{ }^{\circ}\text{C}$  (HSGZ-480). On the right, the corresponding room-temperature FTIR spectra.

The DTA curve of HSGZ-480 exhibits only one crystallization exothermic peak at higher temperature; whereas, no significant changes are seen in the FTIR spectrum with respect to that of the HSGZ-400.

To identify the nature of crystalline phases, HSGZ-400 was used to prepare two samples by heating at  $10\text{ }^{\circ}\text{C}/\text{min}$  up to  $480\text{ }^{\circ}\text{C}$  (just to the maximum of the first DTA exopeak, HSGZ-400/480) and  $550\text{ }^{\circ}\text{C}$  (just to the end of the second DTA exopeak, HSGZ-400/550) and then quenched. The corresponding XRD profiles are shown in Figure 3.5 where the pattern of HSGZ-400 is also reported.

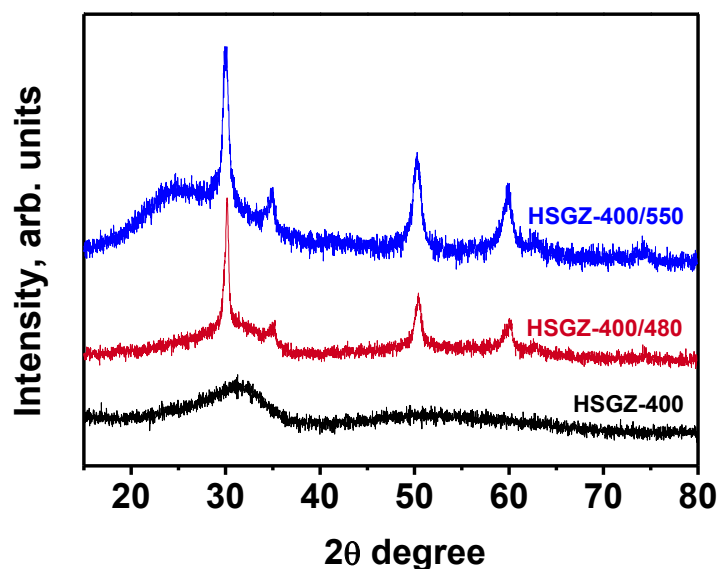


**Figure 3.5.** XRD patterns of dried gel heated up to  $400\text{ }^{\circ}\text{C}$  and then quenched (HSGZ-400). This sample is heated up to  $480\text{ }^{\circ}\text{C}$  (HSGZ-400/480) and up to  $550\text{ }^{\circ}\text{C}$  (HSGZ-400/550).

XRD patterns show that HSGZ keeps its amorphous nature up to 400 °C. When the sample is heating at higher temperature, the formation of ZrO<sub>2</sub> nanocrystals of the tetragonal polymorph, T-ZrO<sub>2</sub>, (JCPDS card 50-1089) starts to occur at the first DTA exopeak. The distinction between tetragonal and cubic phase is not an easy task on account of the overlapping reflections; nevertheless, the above-reported assignment is given both of the lack of (0 4 0) reflection at  $2\theta = 73.98^\circ$  characteristic of the cubic polymorphous and of the presence of the peak at  $2\theta = 74.58^\circ$  detectable for the tetragonal polymorph.<sup>92</sup>

The shape and the position of DTA crystallization peak differ from the ones previously reported for a zirconia gel-derived material prepared using a different Zr/acetylacetonate molar ratio<sup>92</sup> so confirming that, when the crystallization starts from an amorphous sol-gel matrix, both the temperature and the rate of crystallization are strongly influenced by the chemical solution.

Comparing XRD profiles of HSGZ-400/480 and HGSZ-400/550 no differences are seen, indicating that in both samples T-ZrO<sub>2</sub> nanocrystals are only formed. On the contrary, the shape of the amorphous halo changes in the 20-30°  $2\theta$  range, exhibiting a great increase for the HSGZ-400/550 in the corresponding of the highest monocline peak. This result with TG/DTA curves of HSGZ-480 (see Figure 3.4) showing a single DTA exopeak and a corresponding inflection point (~519 °C) on TG curve allow to relate this thermal effect mainly to a modification of the HSGZ amorphous matrix that is partially overlapped to T-ZrO<sub>2</sub> crystallization.

During the non-isothermal devitrification, the growth of a crystalline phase, different from the thermodynamically stable one, has been often observed. It can be said that during a DTA run, the phase that grows faster will be obtained, regardless of the thermodynamic stability and chemical composition.<sup>93</sup> The initial formation of the metastable tetragonal phase occurring from the non-isothermal crystallization of zirconia dried gel can be explained on the basis of its structural similarity with the sol-gel matrix.<sup>92</sup> Its formation is driven and controlled by kinetic aspects. When the crystallization starts from a preheated sample, such as HSGZ-400, the transformation involves mainly the residual amorphous phase and the thermodynamic aspects begin to prevail, facilitating the transformation toward the stable monoclinic phase.

To evidence the optical characteristics induced by the formation of Zr-*acac* complex, the UV-Vis DR spectrum of the hybrid material is compared with that of zirconia gel obtained

without to use of *Hacac* (SGZ). UV-vis DR absorption spectra, calculated using the Kubelka-Munk function  $F(R_\infty)$ , are reported in Figure 3.6.

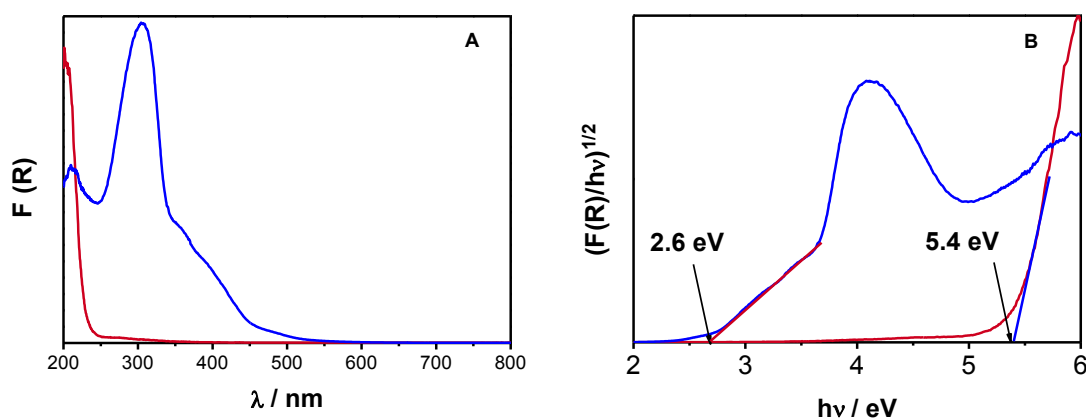
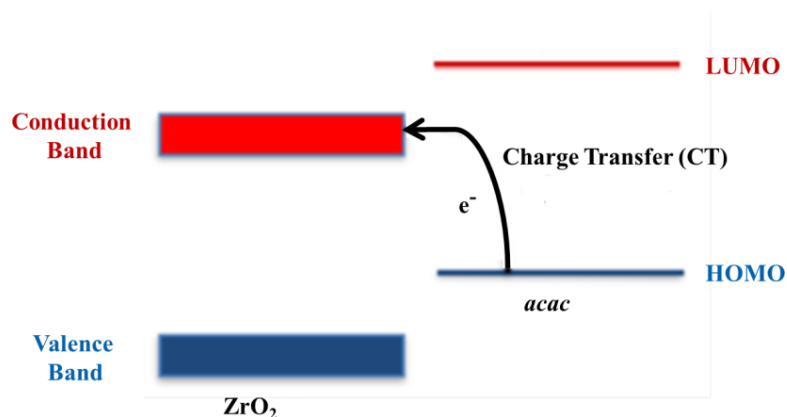


**Figure 3.6.** UV-vis DR absorption spectra (A) and band gap evaluation (B) for HSGZ (blue line) and SGZ (red line) samples.

In Figure 3.6 (A), the HSGZ spectrum (blue line) is characterized by a first peak at about 220 nm and a second one at 300 nm with a shoulder-like queue in the visible region up to 550 nm. In contrast, SGZ (red line) shows only an absorption peak in the UV region at wavelengths below about 220 nm (Figure 3.6 (A)). Figure 3.6 (A) shows that, apart from the presence of the peak at 300 nm, a marked red shift of the absorption edge is seen in the HSGZ material with respect to SGZ one. A quantitative evaluation of the shift of the absorption edge was obtained by linearization of the plot of  $(F(R)hv)^{1/2}$  against  $hv$ , as reported in Figure 3.6(B). For the amorphous SGZ material the value 5.4 eV was obtained, consistent with the transition from the valence band (VB) to conduction band (CB), i.e. related to the  $O^{2-} \rightarrow Zr^{4+}$  charge transfer transition, in agreement with the band gap value reported in the literature for crystalline zirconia.<sup>94</sup> For HSGZ sample absorption occurs at a much lower  $hv$  value, 2.6 eV (460 nm). This low value is associated with  $n \rightarrow \pi^*$  intraligand electronic transition producing the yellow-brown color of the HSGZ zirconia-*acac* gel material.<sup>26</sup> The peak at 300 nm is mainly due to  $\pi \rightarrow \pi^*$  intraligand electronic transition,<sup>26</sup> a further contribution possibly arising from  $\pi(acac) \rightarrow \pi^*(acac)/d(Zr)$  transition that is characterized by a partial ligand-to-metal charge transfer (LMCT).<sup>25</sup>

The extension of the HSGZ absorption in the visible range clearly indicates a mechanism of charge injection from the ligand into the conduction band of the oxide by direct excitation from the HOMO of the *acac* ligands to the 3d-(Zr) CB. This requires that the

alignment of the bands at the hybrid interface is staggered as shown by the energy diagram in Scheme S-3.1.



**Scheme S-3.1.** Energy diagram relative to charge transfer mechanism between *acac* and  $\text{ZrO}_2$  crystalline.

Ligand-to-metal charge-transfer (LMCT) can also induce the generation of electron/hole pairs ( $e^-/h^+$ ) in the HSGZ solid material, where the electrons in the conduction band do not belong to specific atoms of the zirconium network but to the solid as a whole.

In the HSGZ material at room temperature *acac*-to-zirconium electron transfer process leads to the coexistence of  $\text{Zr(IV)-acac}$  and  $\text{Zr(III)-acac}^\bullet$  complexes in equilibrium at this temperature (Figure 3.7).

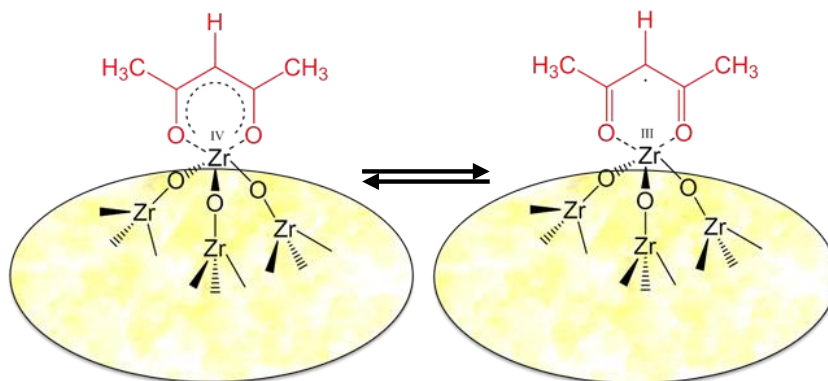
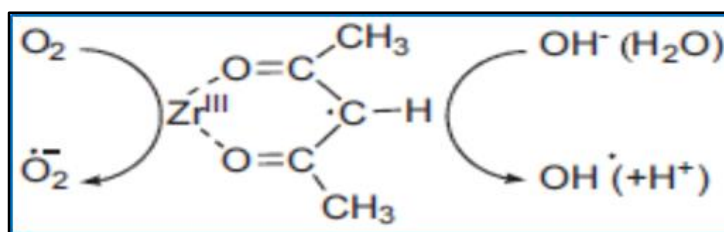


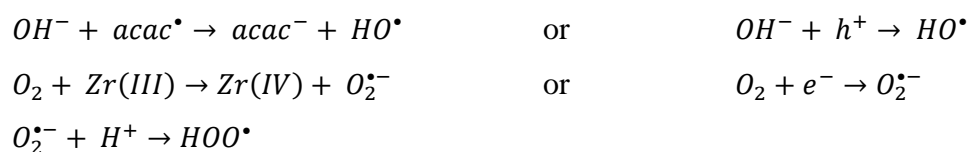
**Figure 3.7.** Schematic representation of the coexistence of  $\text{Zr(IV)-acac}$  and  $\text{Zr(III)-acac}^\bullet$  complexes in equilibrium at room temperature.

The extended oxide matrix also can allow electron delocalization and consequent low recombination rate. This makes the electrons in CB highly reactive in molecular  $\text{O}_2$  reduction to  $\cdot\text{O}_2^-$  superoxide radicals. When HSGZ is used as catalyst in aqueous solution, in the presence of molecular oxygen, other reactive oxygen species (ROSs) are produced on its surface, according to Scheme S-3.2.



**Scheme S-3.2.** Schematic representation of the reactive oxygen species produced on the HSGZ surface in presence of O<sub>2</sub>.

Alternatively, this process can be also described as follows:



Therefore, the interaction of O<sub>2</sub> with Zr<sup>3+</sup> sites generates <sup>•</sup>O<sub>2</sub><sup>-</sup> radical species, which remain coordinated to the metal and simultaneously re-oxidize it in Zr<sup>4+</sup> species. This result is very interesting because the superoxide ion radicals are generally formed only on the surface of ZrO<sub>2</sub> activated by annealing in air or in vacuum at 500-600 °C and then contacted with molecular oxygen at 130 °C.<sup>95</sup>

The molecular oxygen O<sub>2</sub> acting as a conduction band electron scavenger inhibits the fast charge recombination shifting toward right the equilibrium in Figure 3.7.

The formation of superoxide <sup>•</sup>O<sub>2</sub><sup>-</sup> on the HSGZ of HSGZ is confirmed by EPR analysis. EPR spectra, shown in Figure 3.8, are recorded at room temperature in the presence of air and kept in the dark for at least 12 h before. EPR spectra in Figure 3.8 (A, C) and (B, D) correspond to HSGZ and SGZ, respectively. These samples are investigated before (A, B) and after annealing (C, D) at 400 °C for 1 h.

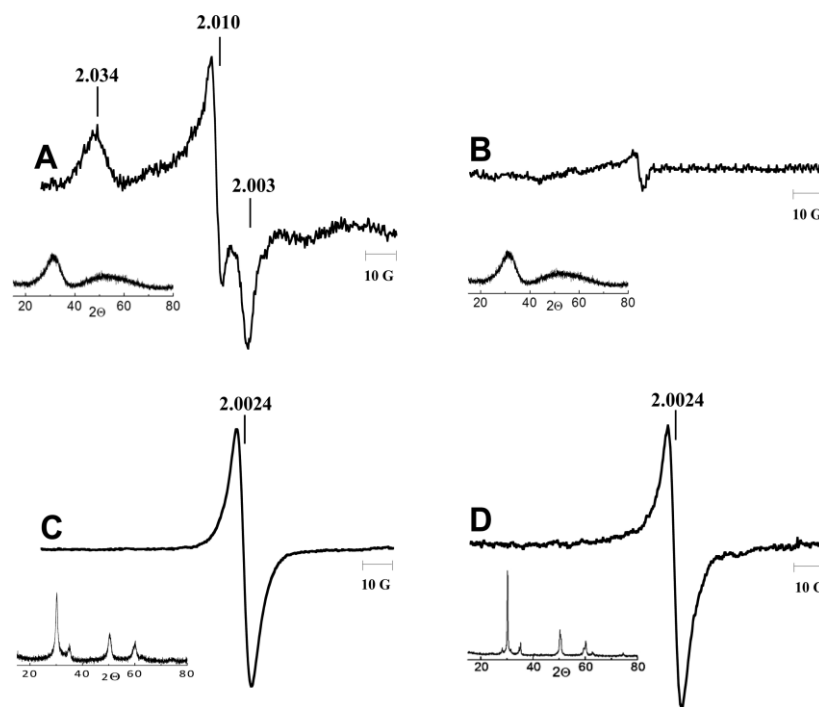


**Figure 3.8.** EPR spectra of (A, C) HSGZ and (B, D) SGZ, (A, B) before and (C, D) after annealing at 400 °C for 1 h. The insets show the XRD data.

The spectrum of the HSGZ-dried sample (Figure 3.8 (A)), presents a complex anisotropic line shape that clearly indicates the presence of radical species on the solid surface. Particularly, this spectrum shows the orthorhombic signal of  $\cdot\text{O}_2^-$  superoxide anion radicals coordinated on surface  $\text{Zr}^{4+}$  ions, as confirmed by the characteristic  $g$ -factor value.<sup>96</sup> Indeed, the  $g$ -tensor of this signal is  $g_{xx} = 2.003$   $g_{yy} = 2.010$   $g_{zz} = 2.034$ , whereas the signal intensity corresponds to a concentration of paramagnetic centers of  $\sim 2 \times 10^{12}$  spin  $g^{-1}$ . The  $g_{zz}$  value is clearly compatible with a tetravalent adsorption site, so that the assignment to the  $\cdot\text{O}_2^-/\text{Zr}^{4+}$  system is straightforward.<sup>88,97</sup>

$\cdot\text{O}_2^-$  is a very reactive and short-lived species; in solution, it can be detected only by using spin traps,<sup>98</sup> whereas its EPR signal has been observed for solid or amorphous materials subjected to drastic treatments. Specifically, spectra similar to that observed for HSGZ are reported in the literature only for crystalline zirconia samples subjected to activation by a thermal pretreatment in vacuum and a contact with oxygen at high temperature or under UV irradiation.<sup>95,97,99</sup>

In Figure 3.8 (B), only a very weak singlet was observed for SGZ ( $\text{ZrO}_2$  without *acac*), positioned at  $g = 2.0024$ , which can be attributed to a few paramagnetic defects due to free electrons localized in oxygen vacancies (F centers).<sup>97</sup> Thus, these results suggest that

*acac* ligands, on the HSGZ surface, play a fundamental role in generating and stabilizing the superoxide radical anions.

EPR spectra were also recorded on HSGZ and SGZ samples heated for 1h at 400 °C (Figure 3.8 (C, D), respectively). The annealing of the HSGZ sample produces the complete *acac* ligands removal as ascertained by thermogravimetric analysis. The spectra of the annealed HSGZ and SGZ show only an intense single peak at  $g = 2.0024$ . Quantitatively, for both samples an increased concentration of paramagnetic defects is observed, up to  $4 \times 10^{13}$  spin  $g^{-1}$  for annealed HSGZ. However, no evidence of  $\cdot O_2^-$  formation is observed, thus showing beyond any doubt that *acac* ligands are necessary to form and stabilize the superoxide anion radicals on the material surface.

Figure 3.8 also shows X-ray diffraction (XRD) insets. Contrary to the initial amorphous samples (XRD insets A and B), in both the annealed ones tetragonal crystalline phase is formed (XRD insets C, D).

### 3.3 Technological Applications

HSGZ material exhibits an intrinsic catalytic activity for the oxidative degradation of many environmental pollutants in aqueous solution without light irradiation.

Starting from promising results obtained on the PHE,<sup>100</sup> the removal and degradations of different chlorinated phenoxyalkanoic acid herbicides is explored during my PhD research.

The chlorinated phenoxyalkanoic acid herbicides investigated are 4-chloro-2-methylphenoxyacetic acid (MCPA), 4-chlorophenoxyacetic acid (4-CPA), and 2,4-dichlorophenoxyacetic acid (2,4-D) belonging to the phenoxyacetic group, and 4-(4-chloro-2-methylphenoxy) butanoic acid (MCPB), a phenoxybutyric herbicide (Figure 3.9). They are classified as potential groundwater contaminants by U.S. EPA, so the development of new remediation technologies appears to be of primary importance.<sup>87</sup>

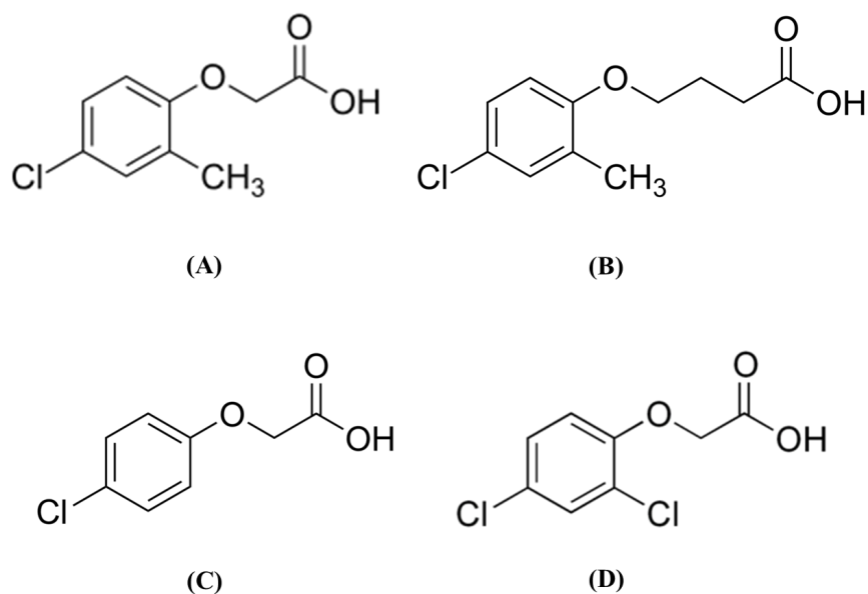


**Figure 3.9.** Schematic representation of herbicides analyzed: MCPA (A), MCPB (B), 4-CPA (C), 2,4-D (D).

HSGZ intrinsic catalytic activity was tested for all pollutants in aqueous solution and in absence of any light irradiation at room temperature.

The kinetics of removal of the four herbicides in the presence of HSGZ is shown in Figure 3.10. For the sake of comparison, the initial concentration ( $C_0$ ) of all the four herbicides has been set at  $0.2 \text{ mmol L}^{-1}$ , and the solid/liquid ratio (R) is 1.0.

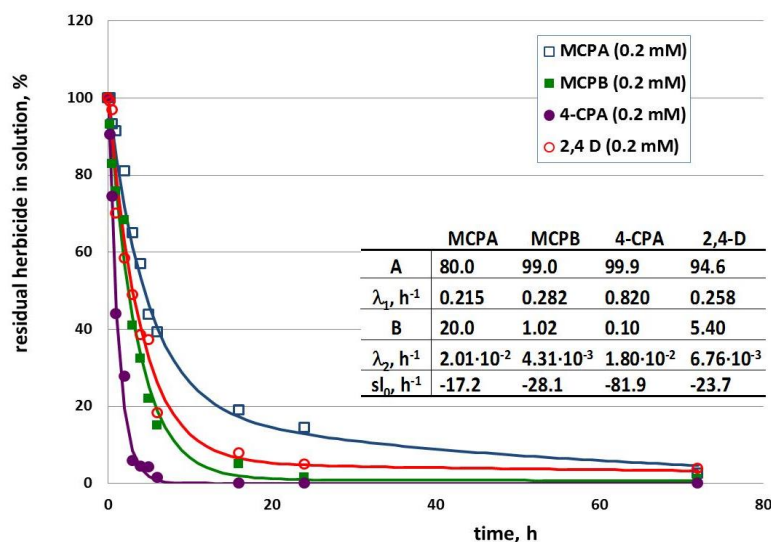
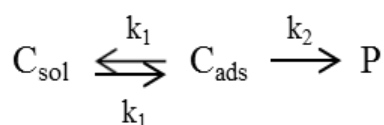


**Figure 3.10.** Kinetics of herbicide removal at 30 °C, in the presence of HSGZ matrix. Herbicides: MCPA (□), MCPB (■), 4-CPA (●), 2,4-D(○).  $C_0 = 0.2 \text{ mmol L}^{-1}$ ,  $R = 1$ . The interpolation curves have been obtained using mathematical model 2. The estimated parameters are reported in the box.

The experimental data demonstrate that an almost complete removal of the herbicides can be achieved in about 3 days at room temperature without any electromagnetic or thermal activation. As the concentration-time profiles could not be satisfactorily described by a pseudo-first-order kinetic model or a pseudosecond-order kinetic model,<sup>101</sup> (both models showed a low correlation coefficient  $r^2$ ), an alternative physico-mathematical model, previously developed for MCPA removal<sup>30</sup> was used to elaborate the data. Briefly, the model is based on the hypothesis that reversible, first-order adsorption on HSGZ surface is the first stage of the herbicide removal as usually occurs in heterogeneous catalysis. The subsequent reaction of herbicides, catalytically driven by HSGZ surface groups, yields degradation products, according to the Scheme S-3.3:



**Scheme S-3.3.** Schematic representation of the removal/degradation herbicides on HSGZ matrix.

where:

- $C_{sol}$  is the herbicide concentration in the liquid phase ( $\text{mmol L}^{-1}$ ),
- $C_{ads}$  is the concentration of adsorbed herbicide ( $\text{mmol L}^{-1}$ ),
- $P$  indicates the degradation products,
- $k_1$  and  $k_{-1}$  are the direct and inverse first-order kinetic constants of the herbicide sorption,
- $k_2$  is the first-order kinetic constants of the herbicide degradation.

The mass balances applied to the chemical species involved in model 1 yield concentration-time profiles describing the herbicide removal by double-exponential curves<sup>30</sup>

$$C_{sol}(t) = Ae^{-\lambda_1 t} + Be^{-\lambda_2 t} \quad (\text{eq. 3.1})$$

where:

- $C_{sol}$  is the herbicide concentration in the liquid phase ( $\text{mmol L}^{-1}$ ),
- $t$  is the time (h).

Mathematical model 2, previously tested only for MCPA removal, could satisfactorily be used to interpolate the experimental data. The interpolating curves are dashed in Figure 3.10, together with the estimated values of the model parameters.

In order to elaborate the experimental data, model 2 was used to evaluate the initial slope of the concentration profiles, i.e., the initial removal rate of herbicide (also reported in Figure 3.10)

$$sl_0 = \left. \frac{dC_{sol}(t)}{dt} \right|_{t=0} = -\lambda_1 A - \lambda_2 B \quad (\text{eq. 3.2})$$

It is possible to observed that when the hypothesis  $\lambda_1 \gg \lambda_2$  can be made, the first exponential term in eq. 3.1 decays much faster than the second exponential term. Consequently, the final part of each concentration profiles in Figure 3.10 can be described by the second exponential term. Physically, the decay of the first exponential term corresponds to the achievement of a pseudostationary condition in the first stage of mechanism proposed in Scheme 3: the sorption on HSGZ. Once this condition is

achieved, further changes in the concentration profiles of herbicides are much slower, as they reflect the kinetics of herbicide degradation (second stage in mechanism of Scheme 3.3), that is described by the second exponential term in eq. 3.1. Therefore, when  $\lambda_1 \gg \lambda_2$ , the parameter  $\lambda_2$  can be assumed to coincide with the first-order kinetic constant of the herbicide degradation ( $k_2$ ). On the other hand, the pre-exponential term B can be seen as a measurement of the herbicide amount that remains in liquid phase once the pseudostationary condition is reached.

Under the experimental conditions adopted to obtain the curves in Figure 3.10, the initial removal rate of 4-CPA is significantly faster as compared to those observed when the other herbicides are tested. This effect is due to the higher sorption rate, as the degradation rate for 4-CPA is not faster than those pertaining to other herbicides.

The values of B are close to zero when using MCPB and 4-CPA, indicating that most of herbicide was removed before the pseudostationary condition is reached. In the tests with 2,4-D and with MCPA, higher values of B are obtained. This indicates that the HSGZ is not able to fully adsorb the herbicide, and the total solute removal is obtained slowly, as the progressive degradation of the adsorbed herbicide shifted the sorption equilibrium. However, the fastest degradation rate is observed in the presence of MCPA.

To clarify the effect of the herbicide concentration, removal tests were carried out adopting, for each herbicide,  $C_0$  values close to solubility limits, as shown in Figure 3.11.

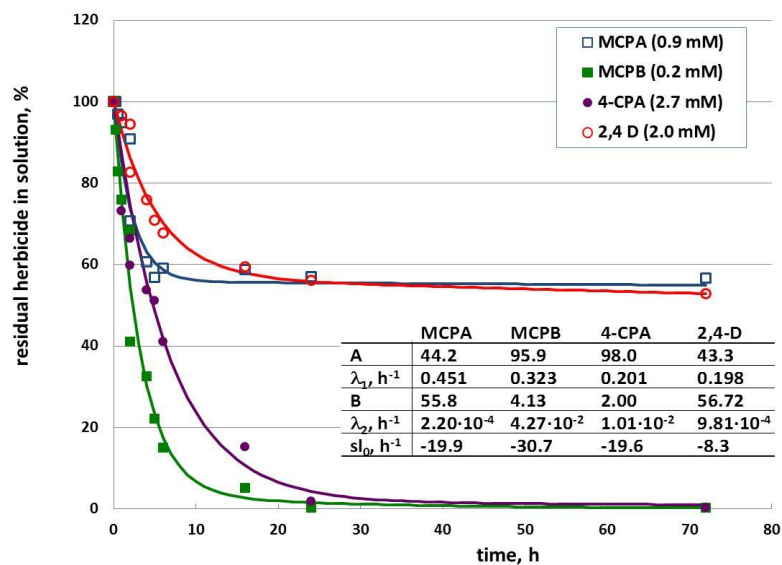


**Figure 3.11.** Kinetics of herbicide removal at 30 °C, in the presence of HSGZ matrix. Herbicides: MCPA (□), MCPB (■), 4-CPA (●), 2,4-D(○) adopted a  $C_0$  value of about 0.9, 0.2, 2.7, 2.0  $\text{mmol L}^{-1}$ , respectively.  $R = 1$ . The interpolation curves have been obtained using mathematical model 2. The estimated parameters are reported in the box.

When working at higher herbicide concentrations, higher values of B is obtained for all the herbicides tested, due to the reduction of herbicide fraction removed during the initial sorption. In particular, using MCPA and 2,4-D, about 50% of herbicides is still in solution once the pseudostationary condition is achieved. In all cases, the rate of degradation of herbicides is slower as the initial  $C_0$  concentration increased.

The effect of the HSGZ concentration (R) is shown in Figure 3.12, with reference to the MCPA degradation.

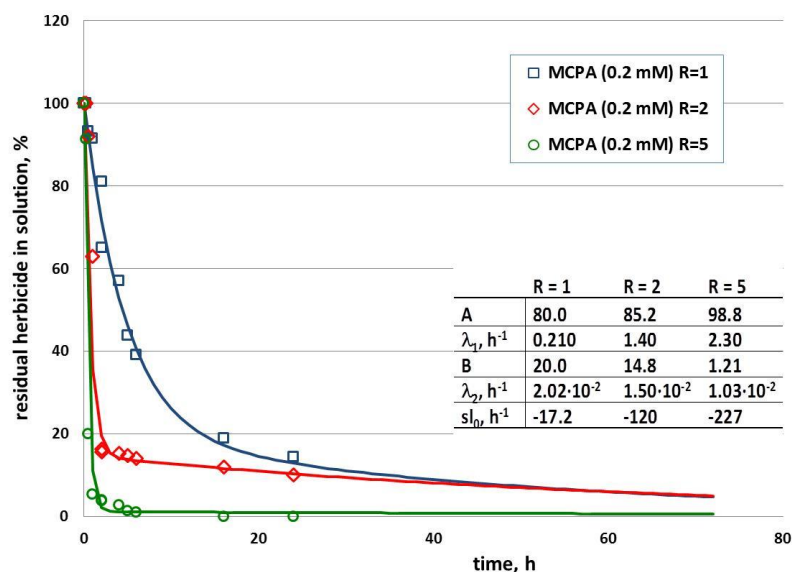


**Figure 3.12.** Kinetics of MCPA removal at 30 °C, in the presence of HSGZ matrix.  $C_0$  value is  $0.2 \text{ mmol L}^{-1}$  and R values are 1 ( $\square$ ), 2 ( $\diamond$ ), 5 ( $\circ$ ). The interpolation curves have been obtained using mathematical model 2. The estimated parameters are reported in the box.

The experimental data demonstrate that, as R increases, the initial rate of the MCPA removal is faster. Increasing the concentration of catalyst (R), a lower amount of residual herbicide still dissolved in solution is found once the pseudostationary condition is achieved, as shown by the decrease of the parameter B.

Similar trends are observed when changing the catalyst concentration in the presence of other herbicides. The results obtained with 2,4-D and 4-CPA are summarized in Table T-3.1.

**Table T-3.1.** Values of parameters of the Physico-Mathematical Model obtained from the removal test of 2,4-D<sup>a</sup> and 4-CPA<sup>a</sup> at 30 °C, in the presence of HSGZ Matrix.

	2,4 D			4-CPA		
	R = 1.0	R = 20	R = 5.0	R = 1.0	R = 20	R = 5.0
A	94.6	109	116	99.9	114	117
$\lambda_1 (h^{-1})$	0.250	0.271	0.282	0.821	0.625	0.640
B	5.40	3.65	2.98	0.110	0.082	0.071
$\lambda_2 (h^{-1})$	$6.76 \times 10^{-3}$	$2.48 \times 10^{-3}$	$1.05 \times 10^{-3}$	$1.80 \times 10^{-2}$	$1.11 \times 10^{-2}$	$7.84 \times 10^{-3}$
$sl_0 (h^{-1})$	-23.7	-98.0	-201	-81.9	-340	-844

<sup>a</sup> $C_0 = 0.2 \text{ mmol L}^{-1}$

Again, increases in the zirconia concentration (R) produce higher values of the initial rate of the MCPA removal, as well as lower values of the parameter B.

When adopting MCPA concentration not above  $0.2 \text{ mmol L}^{-1}$ , a complete herbicide removal is obtained in a treatment time of 24-72 h. On the basis of these results, it can be observed that the kinetics of herbicide removal by sorption/degradation mechanism using HSGZ is comparable to that obtained by photodegradation,<sup>102,103</sup> and in any case they were much faster in comparison to ones achieved by bio-augmentation.<sup>104</sup>

This ability is due to facility to produce free radicals formed by an intramolecular LMCT mechanism, confirmed by structural characterization (UV-vis DR and EPR spectroscopy).

### **3.3.1 Long-Term Application**

To evaluate the suitability of the HSGZ matrix for commercial application, the long-term performance of its was tested by repeated batch cycles of MCPB removal (Figure 3.13). Each batch sorption cycle was carried out for 1 h at  $30 \text{ }^{\circ}\text{C}$  and  $R = 10$ , restoring the initial concentration of MCPB ( $0.2 \text{ mmol L}^{-1}$ ) after each test.

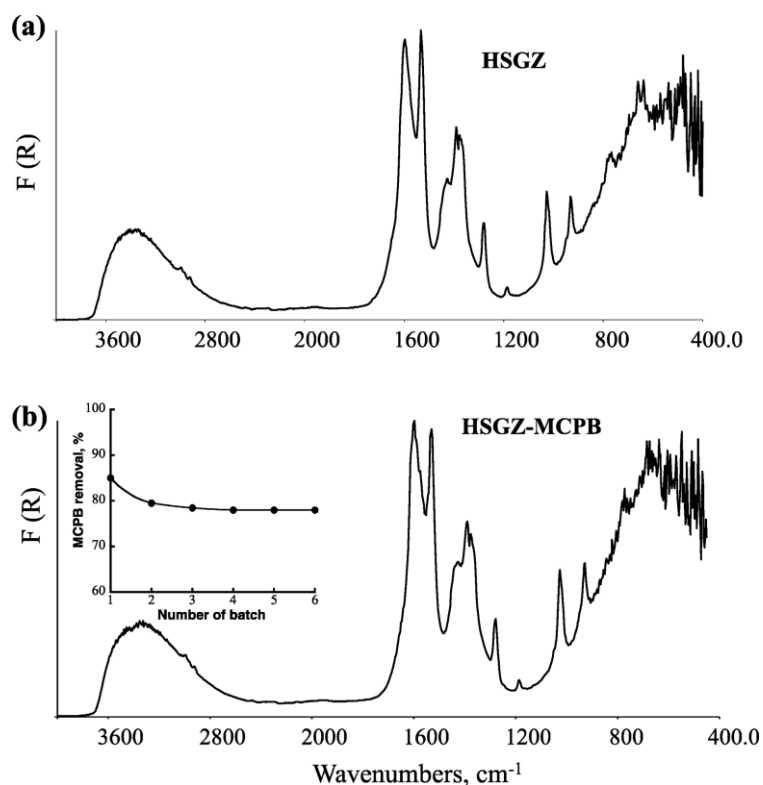


**Figure 3.13.** FTIR spectra recorded at room temperature. (a) HSGZ matrix; (b) HSGZ matrix after six repeated batch tests with  $0.2 \text{ mmolL}^{-1}$  of MCPB solution. In the inset of the (b), repeated batch tests are reported.

In Figure 3.13, no significant change is seen in the FTIR spectrum of HSGZ after 6 batches indicating the stability of the catalyst. Moreover only a slight decrease of the fractional MCPB removal from the first test (85%) to the second (80%) is revealed by the data in the inset. Nevertheless, the removal efficiency remains virtually constant in the following 5 tests. On the basis of these results, it can be envisaged that a long-term use of the HSGZ matrix is possible.

## **RESULTS AND DISCUSSION**

### **PART 2A**

### 3.4 Nb<sub>2</sub>O<sub>5</sub>•SiO<sub>2</sub> mixed oxides

The catalytic performance of the niobium oxide-based materials can be controlled by modulating the acidic properties, by regulating the structure and in turn, the preparation method.

The influence of the preparation procedure on the structure and the properties of the final materials was studied preparing Nb<sub>2</sub>O<sub>5</sub>•SiO<sub>2</sub> material with different synthetic approaches but containing a similar amount of Nb<sub>2</sub>O<sub>5</sub> (~ 19 wt. %).

According to a procedure proposed by Aronne et al.,<sup>40</sup> in detail reported in paragraph 2.2, a Nb<sub>2</sub>O<sub>5</sub>/SiO<sub>2</sub> homogeneous gel was obtained at room temperature using suitable molecular precursors of silicon and niobium. During the synthesis, the hydrochloride acid (HCl) is employed because it acts both as catalyst and as complexing agent of the Nb<sup>5+</sup> ion allowing to obtain transparent chemical gels. In these operating conditions, neither TEOS prehydrolysis nor the addition of specific complexing agent is required. The catalyst was obtained by finely grounding the hardened dry gel, and then annealing it at 400 °C for 3 h. Hereafter this sample will be indicated as NbsgII.

NbsgI indicates Nb<sub>2</sub>O<sub>5</sub>/SiO<sub>2</sub> catalyst obtained by a different sol–gel procedure, reported in literature.<sup>44</sup> The synthesis occurs under nitrogen flow due to use of niobium ethoxide as niobium source. The homogeneous gel is obtained after TEOS prehydrolysis in HCl 0.1 M solution and adding a defined amount of tetrapropylammonium hydroxide ((C<sub>3</sub>H<sub>7</sub>)<sub>4</sub>NOH, TPAOH, 20 % wt. in water) in the final solution. The unripe solid was aged at room temperature for 24 h, dried under vacuum at 40 °C for 2 h, and then annealed at 550 °C for 8 h.

The Nb<sub>2</sub>O<sub>5</sub>/SiO<sub>2</sub> catalyst obtained by wet impregnation was prepared according to the procedure reported elsewhere,<sup>105</sup> using a commercial silica (grinded Silica Degussa Aerolyst 3038 whose morphological characteristics are: BET surface area = 194 m<sup>2</sup>g<sup>-1</sup>; pore volume = 0.96 cm<sup>3</sup>g<sup>-1</sup>; average pore size ≈ 19 nm) and niobium oxalate in oxalic acid solution (0.1 M), as Nb source. The niobium oxalate was obtained from niobium pentoxide according to procedure reported in literature.<sup>105</sup> After drying, the solid was calcined at 975 °C for 6 h. Hereafter this sample will be indicated as Nbimp.

The Nb<sub>2</sub>O<sub>5</sub> catalyst was obtained by annealing commercial Nb<sub>2</sub>O<sub>5</sub> powders (from Aldrich) at 900 °C for 6 h.

All these materials were characterized by various techniques and tested in the epoxidation of methyl oleate with hydrogen peroxide as “green” oxidant agent.

### 3.5 Structural and morphological characterization

The niobium oxide-based materials were characterized by using complementary techniques. All the measurements were carried out starting annealed samples.

The nature of crystalline niobium phases was investigated by XRD spectroscopy. The XRD patterns of the catalysts are shown in Figure 3.14.

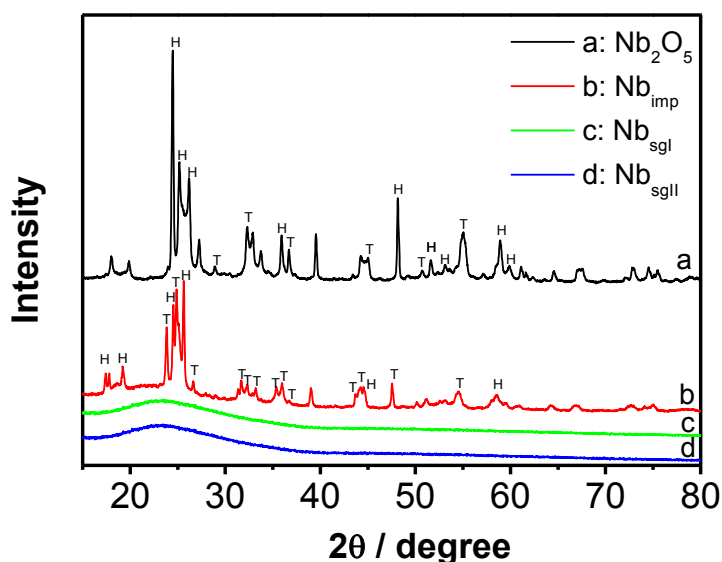


**Figure 3.14.** XRD patterns of the investigated catalysts. (a)  $\text{Nb}_2\text{O}_5$ , (b)  $\text{Nb}_{\text{imp}}$ , (c)  $\text{Nb}_{\text{sgI}}$ , and (d)  $\text{Nb}_{\text{sgII}}$ . H: monoclinic H- $\text{Nb}_2\text{O}_5$ , T: orthorhombic T- $\text{Nb}_2\text{O}_5$ .

It is known that the amorphous niobium pentoxide exhibits a complex crystallization behavior upon heating both in the pure state<sup>106</sup> and deposited on a support.<sup>31,41</sup> In the latter case, the crystallization behavior is strongly affected by the support physico-chemical properties. The XRD profile of  $\text{Nb}_2\text{O}_5$  catalyst (trace “a” in Figure 3.14) exhibits different peaks, the majority of which are related to the monoclinic H-  $\text{Nb}_2\text{O}_5$  (PDF card 37-1468) phase, and the residual ones to the orthorhombic T- $\text{Nb}_2\text{O}_5$  (PDF card 30-0873) phase.

A reverse trend is seen in the XRD profile of  $\text{Nb}_{\text{imp}}$  (trace “b” in Figure 3.14), where T- $\text{Nb}_2\text{O}_5$  is the main crystalline phase.

On the contrary, XRD profiles of both gel-derived catalysts (traces “c” and “d” in Figure 3.14) show an amorphous halo centered at  $2\theta = 22^\circ$ , typical of amorphous silica, indicating their amorphous nature. No peaks related to the presence of  $\text{Nb}_2\text{O}_5$  crystalline aggregates are detectable for these samples.

The coordination geometry and the chemical arrangement of the Nb species were determined by UV–vis DR spectroscopy. The Figure 3.15 shows the UV–vis DR spectra of the investigated catalysts.

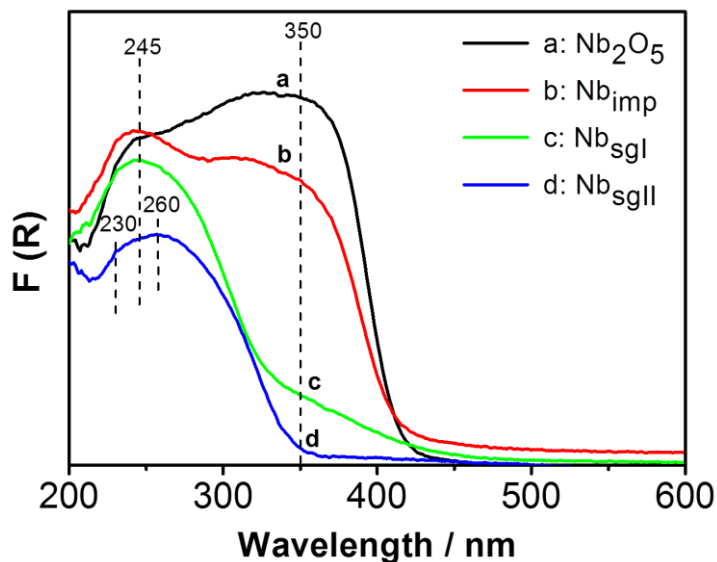


**Figure 3.15.** UV–vis DR spectra of the studied catalysts. (a)  $\text{Nb}_2\text{O}_5$ , (b)  $\text{Nb}_{\text{imp}}$ , (c)  $\text{Nb}_{\text{sgI}}$  and (d)  $\text{Nb}_{\text{sgII}}$ .

The spectrum of  $\text{Nb}_2\text{O}_5$  catalyst (trace “a” in Figure 3.15) shows a broad band in the 300–400 nm range, centered at about 350 nm due to niobia nanodomains (low distorted  $\text{NbO}_6$  octahedra, i.e. corner-sharing  $\text{NbO}_6$  octahedra), and another one at about 245 nm, corresponding to ligand-to-metal charge-transfer transition (LMCT from  $\text{O}^{2-}$  to  $\text{Nb}^{5+}$ ).

The UV–vis DR spectrum of  $\text{Nb}_{\text{imp}}$  (trace “b” in Figure 3.15) exhibits a very similar profile, even if the relative intensity of the two broad bands is reversed, confirming the presence of niobia nanodomains on the surface of this sample.

The UV–vis DR spectra of gel-derived catalysts are dominated by the LMCT band, even if few differences can be recognized. For the  $\text{Nb}_{\text{sgI}}$  (trace “c” in Figure 3.15), this band is centered around 245 nm and it is slightly narrower than that for  $\text{Nb}_{\text{sgII}}$  (trace “d” in Figure 3.15), even if it appears tailed showing a residual absorption in the 340–380 nm range. In this wavelength range, on the contrary, the spectrum of  $\text{Nb}_{\text{sgII}}$  does not show any absorption and, in addition, it exhibits features at about 230 nm and 260 nm that can be assigned to isolated  $\text{NbO}_4$  tetrahedra and distorted  $\text{NbO}_6$  octahedra, respectively.<sup>107</sup> The above-noted differences can be related to a wider distribution of isolated Nb structural units in  $\text{Nb}_{\text{sgII}}$  than in  $\text{Nb}_{\text{sgI}}$ , with the presence of a greater amount of more polymerized

species (clustering of  $\text{NbO}_6$  octahedra) in the latter sample. Therefore, it can be inferred that the sgI route gives a good dispersion of Nb species into the siloxane framework, with predominant isolated  $\text{NbO}_x$  units besides a low amount of larger units in comparison with the sgII route.

The textural and morphological characterization were performed by SEM/EDX and  $\text{N}_2$ -adsorption-desorption isotherms calculating the Surface Specific Area (SSA) by BET method. SEM micrographs of the investigated catalysts are displayed in Figure 3.16.

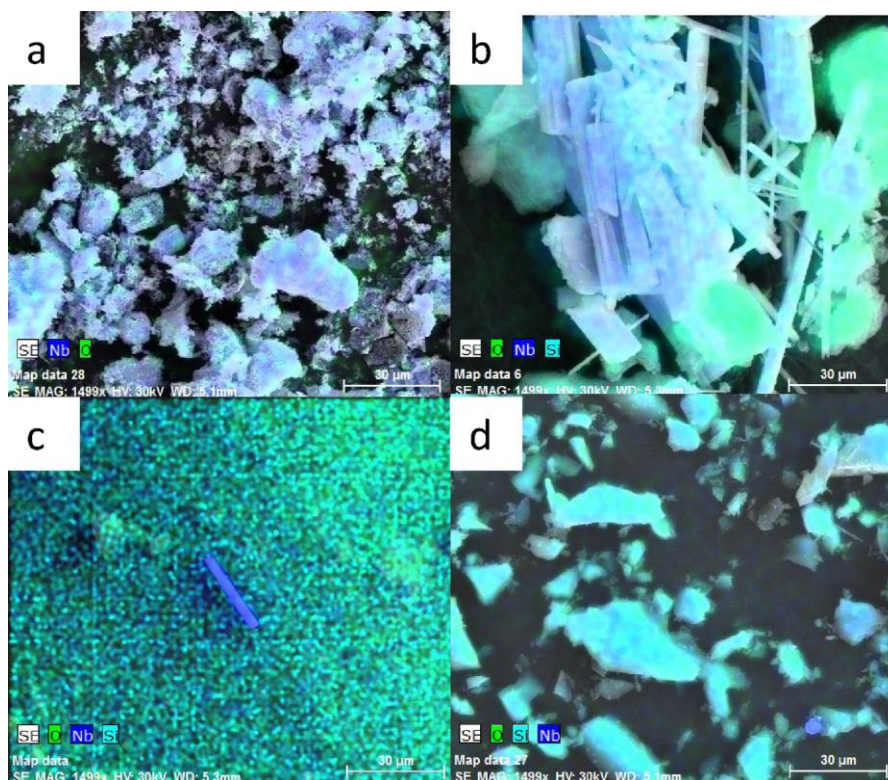


**Figure 3.16.** SEM micrographs (magnification 1500 $\times$ ) of the surface of the studied catalysts. (a)  $\text{Nb}_2\text{O}_5$ , (b)  $\text{Nb}_{\text{imp}}$ , (c)  $\text{Nb}_{\text{sgI}}$ , and (d)  $\text{Nb}_{\text{sgII}}$ . Atomic maps of Nb (blue) and Si (green) derived from EDX analysis are also showed.

From SEM images, besides the morphology of the catalysts, it is possible to see the atomic distribution of Nb (blue) and Si (green), as obtained by EDX analysis.

$\text{Nb}_2\text{O}_5$  (Figure 3.16 (a)) has a morphology characterized by crystals of irregular shape, while in the  $\text{Nb}_{\text{imp}}$  (Figure 3.16 (b)) sample the presence of  $\text{Nb}_2\text{O}_5$  crystals having a needle shape is clearly observed on to silica matrix. This proves the expected low efficiency of the impregnation method to homogeneously disperse the oxide phases on oxide supports. On the contrary, Nb species appear homogeneously distributed on the sample surfaces of gel-derived catalysts  $\text{Nb}_{\text{sgI}}$  and  $\text{Nb}_{\text{sgII}}$ , that exhibit a similar morphology formed by

irregular polyhedral-shaped particles. However, the efficiency of Nb dispersion is higher in Nb<sub>sgII</sub> (Figure 3.16 (d)) than in Nb<sub>sgI</sub> (Figure 3.16 (c)), where spots of Nb atoms are more clearly visible. Therefore, SEM images confirm the above structural analysis. In Table T-3.4, the textural characteristics of the catalysts under investigation are summarized.

**Table T-3.4.** Morphological characterization of the investigated catalysts.

<b>Catalyst</b>	<b>Nb<sub>2</sub>O<sub>5</sub> nominal content (% wt.)</b>	<b>Nb<sub>2</sub>O<sub>5</sub> Actual content (% wt.)</b>	<b>BET (SSA) (m<sup>2</sup> g<sup>-1</sup>)</b>	<b>Pore volume (cm<sup>3</sup>g<sup>-1</sup>)</b>
<b>Nb<sub>imp</sub></b>	20.0	15.0 <sup>a</sup>	161	0.10
<b>Nb<sub>sgI</sub></b>	14.9	11.2 <sup>b</sup>	434	0.93
<b>Nb<sub>sgII</sub></b>	18.9	19.1 <sup>c</sup>	159	0.11
<b>Nb<sub>2</sub>O<sub>5</sub></b>	-	99.9 <sup>d</sup>	11	-

(a) by ICP; (b) by XPS;<sup>105</sup> (c) by spectrophotometry;<sup>40</sup> (d) purchased from Aldrich and calcined at 900°C.

The low surface area of the Nb<sub>2</sub>O<sub>5</sub> catalyst is mainly related to its crystalline nature and to the high calcination temperature, while the higher value measured for the Nb<sub>imp</sub> catalyst is likely due to the poor coverage of silica matrix by Nb-phase.

The Nb<sub>sgI</sub> and Nb<sub>sgII</sub> samples exhibit different textural characteristics. Both BET area and pore volume of Nb<sub>sgI</sub> are higher than those of Nb<sub>sgII</sub>. On the other hand, different pore size distributions were shown by these gel-derived samples: Nb<sub>sgI</sub> is mesoporous, showing in prevalence a broad pore size distribution centered at about 4 nm; on the contrary Nb<sub>sgII</sub> is microporous, mainly showing a narrower pore size distribution centered at about 2 nm. These different results are mainly due to the gelation mechanism. In particular, the gelation of Nb<sub>sgI</sub> is caused by the addition of TPAOH to the starting solution that acted as templating agent.

On the contrary, the gelation of Nb<sub>sgII</sub> occurred upon the completion of hydrolysis and polycondensation reactions, taking place in the starting solution and leading to the formation of interconnected framework of Nb–O–Si linkages.

### 3.6 Catalytic activity: methyl oleate epoxidation

The catalytic performances of the investigated catalysts in the epoxidation of methyl oleate with hydrogen peroxide are compared with those of Nb<sub>2</sub>O<sub>5</sub> in Figure 3.17.

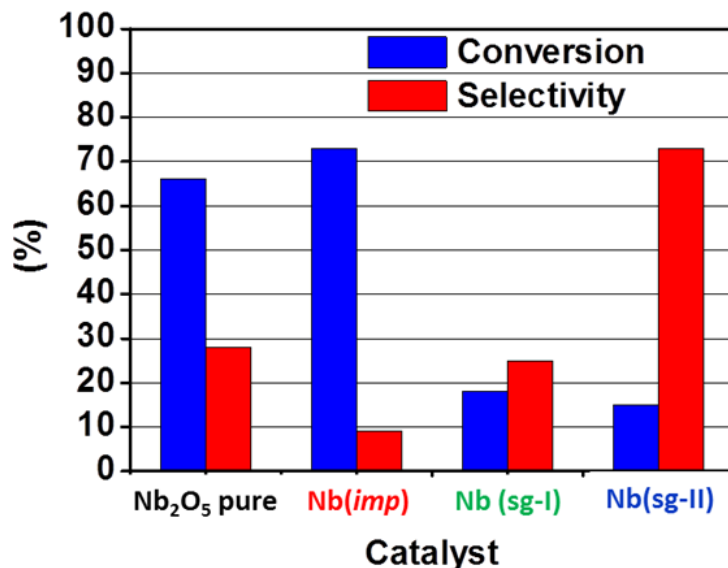


**Figure 3.17.** Conversion (C) and selectivity (S) for the epoxidation of methyl oleate with hydrogen peroxide catalyzed by different niobium oxide-based materials. Reaction conditions: catalyst, 600 mg; acetonitrile, 20 cm<sup>3</sup>; methyl oleate, 5 g (25 mmol); hydrogen peroxide 54.9 % wt., 6.9 g (111 mmol); temperature, 80–82°C. Both Conversion (%) and Selectivity (%) were measured after 5 h of reaction.

Nb<sub>2</sub>O<sub>5</sub> and Nb<sub>imp</sub> show a good conversion (about 70%), which is related with the presence of Lewis acid sites on the surface, but a moderate selectivity that becomes very low for Nb<sub>imp</sub>. It is generally believed that acid sites of moderate strength are involved in the epoxidation mechanism, while strong acidity activates the decomposition of H<sub>2</sub>O<sub>2</sub>, giving the epoxide ring opening.<sup>35</sup> Particularly, Lewis acid sites of moderate strength promote the epoxidation, while Brønsted acid sites and/or strong Lewis sites give the formation of diols.<sup>36</sup> Therefore, the performance of the crystalline catalysts can be related to the concentration of the different crystalline structures in these samples. The higher concentration of monoclinic H-phase which has a complex structure, originating from the existence of superstructures comprising 3x5 and 3x4 ReO<sub>3</sub> type blocks,<sup>106</sup> is present in Nb<sub>2</sub>O<sub>5</sub> sample, whereas the concentration of orthorhombic T-phase (formed by corner- and edge-sharing distorted octahedra and pentagonal bipyramids<sup>31</sup>) is higher in the case of Nb<sub>imp</sub>. So Nb<sub>imp</sub> contains the higher concentration of distorted NbO<sub>6</sub> octahedra, i.e. the

higher concentration of Brønsted acid sites and consequently it exhibits the lower selectivity.

Both gel-derived catalysts exhibit a moderate conversion (about 15%), while their selectivity is greatly different. Nb<sub>sgII</sub> shows the highest selectivity (about 70%) among all the investigated catalysts. This behavior can be related to two diverse characteristics of the gel-derived catalysts that are related to each other: the dispersion degree of the active phase (NbO<sub>4</sub> tetrahedra) into the siloxane matrix and the distribution of the surface acid sites.

According with recent results obtained for the epoxidation with H<sub>2</sub>O<sub>2</sub>,<sup>108,109</sup> the presence of only Nb species in tetrahedral coordination seems to be the key point to determinate the selectivity to epoxide. As shown in Figure 3.15, Nb<sub>sgII</sub> exhibits a wider distribution of isolated Nb structural units than Nb<sub>sgI</sub> that, on the contrary, shows a greater amount of more polymerized species (clustering of NbO<sub>6</sub> octahedra) than Nb<sub>sgII</sub>. Therefore the distribution of the surface acid sites in these samples is very different. The concentration of Lewis acid sites results higher for Nb<sub>sgII</sub> than Nb<sub>sgI</sub> and, at the same time, the concentration of Brønsted acid sites is higher in Nb<sub>sgI</sub> than in Nb<sub>sgII</sub>, yielding the higher selectivity to epoxide for the Nb<sub>sgII</sub> catalyst.

**RESULTS AND DISCUSSION**  
**PART 2B**

### 3.7 Ru/RuO<sub>2</sub>@Nb<sub>2</sub>O<sub>5</sub>•SiO<sub>2</sub> (RNS) system

Ru-based mixed oxide (Ru/RuO<sub>2</sub>@Nb<sub>2</sub>O<sub>5</sub>-SiO<sub>2</sub>) was obtained by an innovative sol-gel synthesis wholly performed at room temperature and characterized by both easy handling of precursors and the lack of toxic or pollutant reactants. A homogeneous gel is obtained starting from niobium (V) chloride and tetraethoxysilane (TEOS) as precursors of the matrix and adding in it a proper amount of ruthenium chloride (~ 6 wt. %). In order to control the porosity of the final material, two specific amount (0.04 and 0.16 % mol., 0.04B-RNS and 0.16B-RNS, respectively) of a nonionic surfactant (polyethylene glycol hexadecyl ether, Brij-C10) were added directly into starting solution of precursors. In this way, the surfactant can play a double role: *i*) as pore-directing agent and *ii*) as oxygen-rich complexing agent of the metallic species. The influence of Brij-C10 incorporation on porous structure, size and dispersion of ruthenium nanoparticles was investigated in detail by structural, morphological and textural characterization.

Ru-based materials were tested in the hydrogenation of levulinic acid to  $\gamma$ -valerolactone by a one-pot mechanism due to acidic (Nb<sub>2</sub>O<sub>5</sub>-SiO<sub>2</sub> matrix) and redox (Ru metal) functionalities of these bifunctional catalysts.

### 3.8 Thermal, structural and morphological characterization

Thermal, structural and morphological measurements were carried out starting from the dried gel and including gels annealed at 500 °C. This temperature stands at the minimum value at which it is possible to obtain stable and fully amorphous inorganic gel-derived materials for all studied compositions, characterized by considerable residual porosity.

Thermal behaviour of RNS dried gel was investigated by TG/DTA analysis. Figure 3.17 shows the TG/DTA curves of the RNS dried gel.

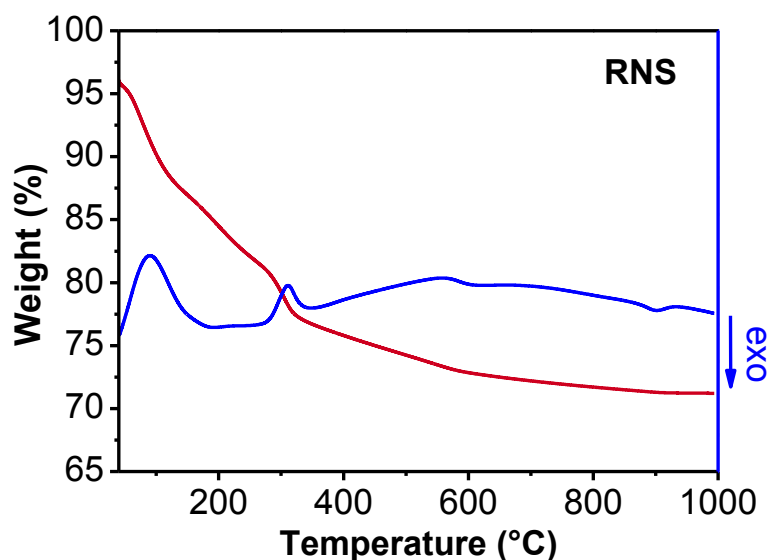


**Figure 3.17** TG/DTA curves of the RNS dried gel recorded in N<sub>2</sub> at 10 °C/min.

From TG curve, a total weight loss of about 29 % wt. was evaluated. Below 400 °C most of the weight loss was found to occur in two main steps. The first inflection point of TG curve occurs at about 80 °C, and it is associated with an endothermic peak in the corresponding DTA curve due to evaporation of water and alcohol molecules physically trapped in the gels pores. The second inflection point of TG curve occurs at about 300 °C, and in the corresponding DTA curve a second endothermic peak is seen. This peak can be related to two overlapped phenomena: the evaporation of solvent and/or organic molecules originating in the dehydration process of the gels that are more tightly trapped in the pores of the siloxane matrix, and their subsequent pyrolysis. At temperatures higher than 400 °C, no additional DTA peaks are observed, only a slight drift of the weight loss (about 2 wt %) still occurs on the TG curve, indicating that the elimination of organic residues as well as of any volatile species is almost completed at 400 °C.

The structural evolution of dried gels upon heat treatment was studied by IR spectroscopy as well as XRD analysis within the range of temperatures used, starting from the dried gel and including gels annealed at 500 °C for 2 h.

FTIR spectra of dried and annealed samples are displayed in Figures 3.18A and 3.18B, respectively.

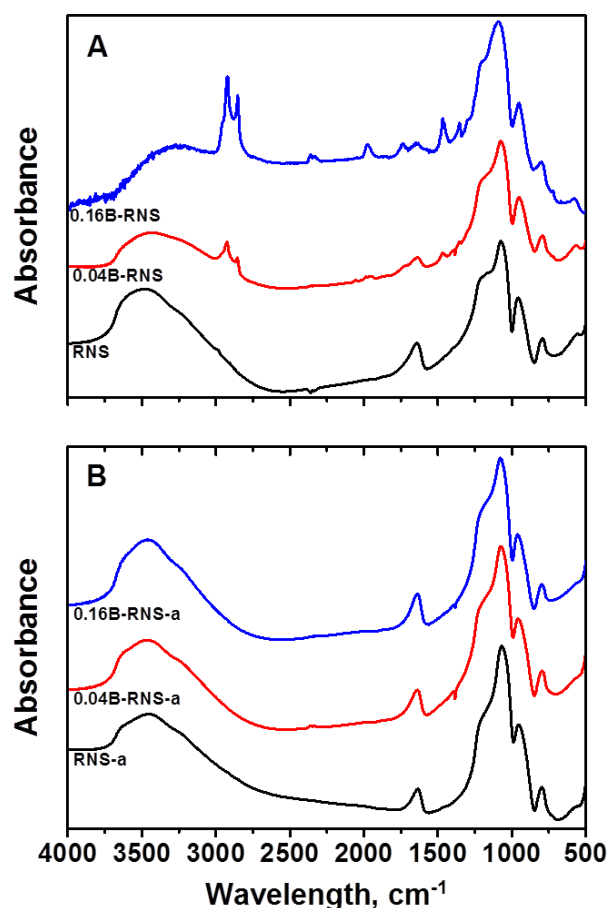


**Figure 3.18.** FT-IR spectra of dried (Figure 3.18A) and annealed (Figure 3.18B) samples.

FTIR spectra of dried gels (Figure 3.18A) show the main envelope in the 1000-1300  $\text{cm}^{-1}$  region, where some of the vibration modes of partially hydrolyzed TEOS molecules<sup>110</sup> overlap with the ones typical of a siloxane network (1080 and 1230  $\text{cm}^{-1}$ ).<sup>111</sup> Absorption bands at about 795  $\text{cm}^{-1}$  ( $\nu_{\text{s Si-O-Si}}$ ),<sup>110</sup> and 1640  $\text{cm}^{-1}$  (deformation modes of O-H bonds and of molecularly adsorbed water,  $\delta_{\text{O-H}}$ )<sup>93,112</sup> are also seen.

The spectrum of RNS dried gel shows a broad adsorption band in the 2800-3800  $\text{cm}^{-1}$  range with a maximum at about 3500  $\text{cm}^{-1}$  and two shoulders at about 3240 and 3650  $\text{cm}^{-1}$ . This broad band arises from O-H stretches involved in hydrogen bonding and the shoulders are related to free and strongly H-bonded OH groups, respectively. Increasing the surfactant content this band gradually shifts towards lower frequencies and the shoulders completely disappear as a consequence of the formation of stronger hydrogen bonding between the surfactant and silanol groups.<sup>40,113</sup> Moreover, FTIR spectra of 0.04B-RNS and 0.16B-RNS (Figure 3.18A) show additional bands related to the surfactant. These bands are visible at 2920  $\text{cm}^{-1}$  ( $\nu_{\text{asym(CH}_3)}$ ), 2840  $\text{cm}^{-1}$  ( $\nu_{\text{sym(CH}_3)}$ ), 1463  $\text{cm}^{-1}$  ( $\delta_{\text{(CH}_2)}$ ) and 724  $\text{cm}^{-1}$  ( $\rho_{\text{(CH}_2)}$ ).<sup>114</sup>

The analysis of the FTIR spectra of gel-derived samples annealed at 500°C for 2h (Figure 3.18B) show that the structural evolution of the dried gels upon heating results in the formation of a typical polymerized siloxane network. An unexpected result is the presence of evident OH related bands in these FTIR spectra that appear almost unchanged with respect to those occurring for dried gels. The  $\delta_{(O-H)}$  band indicates that the annealed samples adsorb water during cooling due to their porous nature, whereas the broad and large  $\nu_{(O-H)}$  band can be related to the stabilization on these samples of Brønsted acid sites of different strength likely occurred for niobium-phosphorus-silicon mixed oxide gels recently prepared.<sup>115</sup> Furthermore, the absence of all peaks related to Brij-C10 (Figure 2B: 0.04B-RNS-a and 0.16B-RNS-a curves) confirms that the selected heat treatment is suitable to completely remove the surfactant.

The XRD patterns of the investigated samples are shown in Figure 3.19.

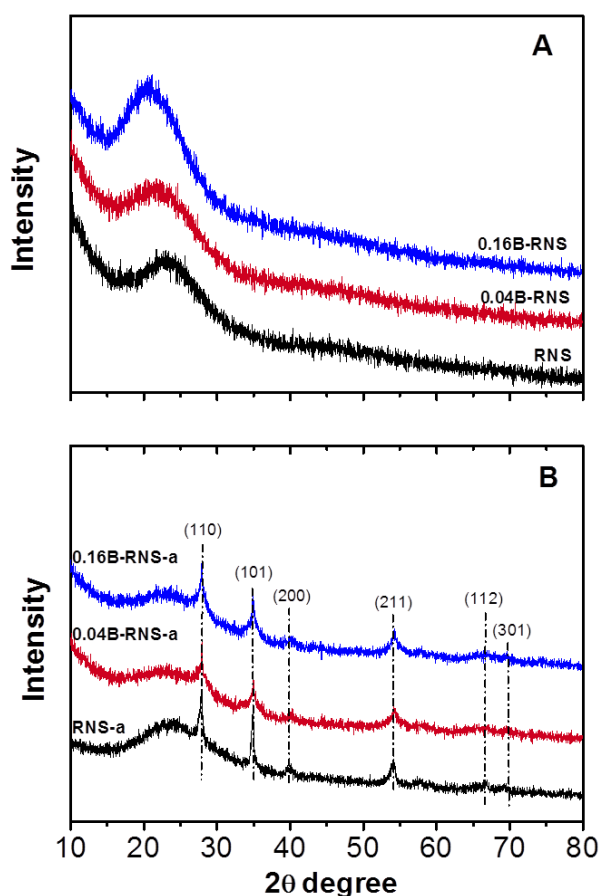


**Figure 3.19.** XRD spectroscopy of dried (Figure 3.19A) and annealed (Figure 3.19B) samples

XRD profiles of all dried gels (Figure 3.19A) show an amorphous halo centered at about  $2\theta = 22^\circ$ , typical of amorphous silica, indicating their amorphous nature.<sup>89,116,117</sup> The absence of typical peaks of Nb<sub>2</sub>O<sub>5</sub> crystalline aggregates suggests that the synthesis procedure allows to obtain a high dispersion of niobium in the siloxane matrix.

A residual amorphous phase can still be noticed in the spectra of all annealed samples (Figure 3.19B) in addition to the typical crystallization peaks of ruthenium (IV) oxide (RuO<sub>2</sub>). [JCPDS Card No. 40-1290]

The RuO<sub>2</sub> crystallite sizes were estimated by Scherrer equation considering the main diffraction lines (110), (101) and (211). Their values progressively decrease from about 25 nm (RNS-a) to about 6 nm (0.16B-RNS-a). This evaluation well agrees with the analysis of TEM images displayed in Figure 3.20. Pictures of RNS-a (Figure 3.20A) and 0.16B-RNS-a (Figure 3.20B) samples at different magnifications and the corresponding RuO<sub>2</sub> particle size distributions (derived from more than 200 nanoparticles) are reported.

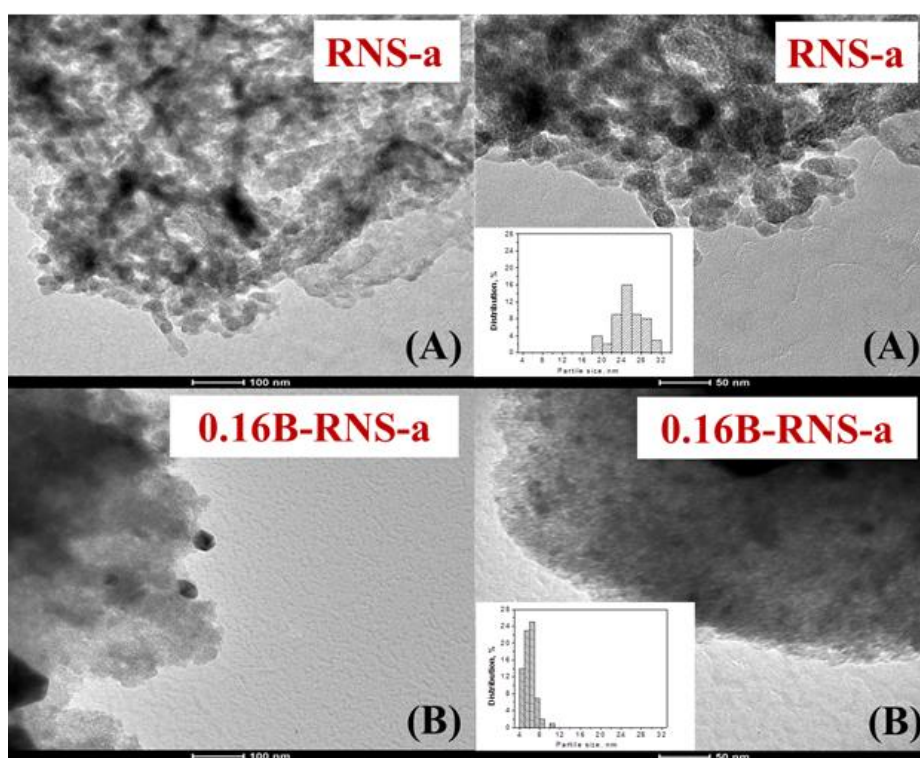


**Figure 3.20.** TEM images of RNS-a (A) and 0.16B-RNS-a (B) samples at low-magnification (left panel) and high-magnification (right panel).

RNS-a samples (Figure 3.20A) show less homogeneous dispersion of ruthenium oxide nanodomains (black zone) with an average particle size of about 25 nm. In contrast, TEM image of 0.016B-RNS-a (Figure 3.20B, left panel) does not show so evident color

contrast. The images are magnified until a higher resolution in order to get much finer details and small black dots appear visible (Figure 3.20B, right panel) which are highly dispersed RuO<sub>2</sub> nanocrystals with an average size of approximately 6 nm.

The differences in particle size of ruthenium oxide and their dispersion are likely due to the different grain growth rate during the synthesis caused by the addition of Brij-C10. These results indicate that Brij-C10 actually plays a role of complexing agent of the metallic species, giving a homogeneous distribution of smaller RuO<sub>2</sub> nanocrystals, and not only acts as pore directing agent, as proven by N<sub>2</sub> isotherms analysis (*vide infra*).

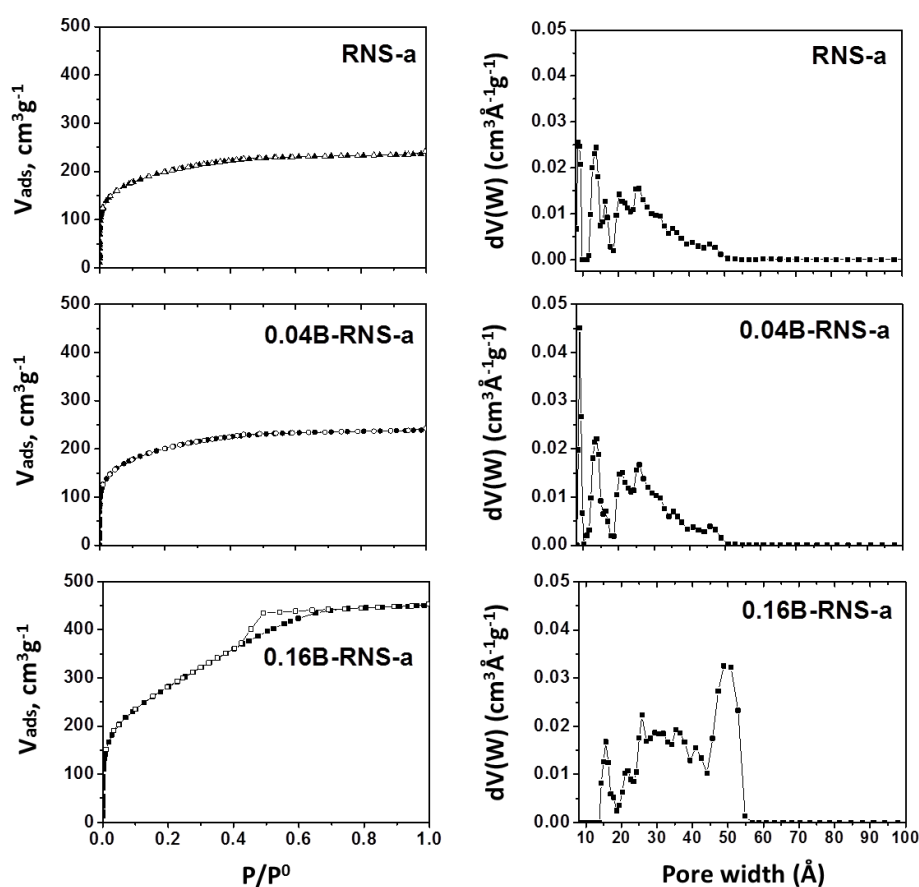


**Figure 3.21.** N<sub>2</sub> adsorption-desorption isotherms of annealed samples (left panel) in which full symbols and empty symbol correspond to adsorption and desorption run, respectively, and PSD of annealed samples (right panel) obtained by NL-DFT method.

N<sub>2</sub> isotherms at -196 °C of annealed samples are reported in Figure 3.21 (left panel). With both RNS-a and 0.04B-RNS-a samples, type I isotherms are obtained, typical of microporous systems, in which a slight deviation from the ideal Langmuirian shape is ascribable to a small degree of mesoporosity. The effect of Brij-C10 addition in the

synthesis batch is instead relevant in the case of 0.16B-RNS-a sample: the corresponding isotherm shows an initial steep increase at low  $P/P^0$  values, due to the presence of micropores, followed by a continuous increase of adsorbed volume with increasing  $P/P^0$  and a small hysteresis loop, suggesting the presence of disordered mesopores with variable diameter. The right part of Figure 3.21 reports the corresponding PSDs: as suggested by the isotherms shape, both micro- and mesopores are present in all the samples, but with different relative abundance. The 0.16B-RNS-a sample shows indeed a major family of mesopores, with diameter in the 20-60 Å range, and a minor contribution of micropores to porous volume. Table T-3.5 reports the corresponding data for the samples prepared at different Brij-C10 content. N<sub>2</sub> adsorption analysis provides evidence that the introduction of a Brij-C10 content equal to 0.04 mol. % (0.04B-RNS-a) does not contribute to a relevant change of the textural properties with respect to the bare sample (RNS), whereas the addition of 0.16 mol % definitely affects both the SSA value and the pore network, in that the total volume increases along with a simultaneous decrease of the microporous volume, indicating the preferential formation of mesopores.

**Table T-3.5.** Samples properties of annealed samples as derived from N<sub>2</sub> sorption isotherms at -196°C.

Sample	SSA (m <sup>2</sup> g <sup>-1</sup> )	Total Pore Volume (cm <sup>3</sup> g <sup>-1</sup> )	Micropore Volume (cm <sup>3</sup> g <sup>-1</sup> ) <sup>c</sup>	Pore Diameter (Å)
0.16B-RNS-a	1030 <sup>a</sup> (1165 <sup>b</sup> )	0.7	0.061	15-50 <sup>c</sup>
0.04B-RNS-a	706 <sup>a</sup> (840 <sup>b</sup> )	0.376	0.132	8-30 <sup>c</sup>
RNS-a	697 <sup>a</sup> (802 <sup>b</sup> )	0.374	0.14	8-30 <sup>c</sup>

<sup>a</sup> calculated according to the BET algorithm

<sup>b</sup> calculated by applying Langmuir equation

<sup>c</sup> obtained by applying the NL-DFT method to isotherms adsorption branch.

SEM images of all annealed samples and their corresponding EDX analysis are reported in Figure 3.22.

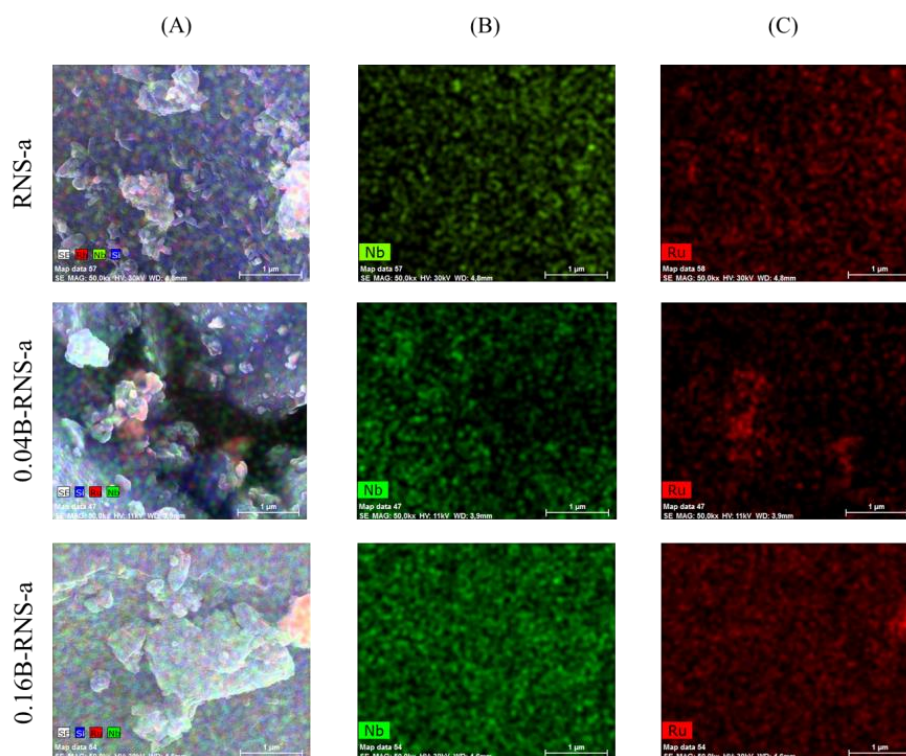


**Figure 3.22.** SEM micrographs (magnification 1500×) of the surface of the studied catalysts. Atomic maps (A) of Nb (green), Si (blue) and Ru (red) derived from EDX analysis are showed.

The atomic distribution of Nb (green), Ru (red) and Si (blue) can be seen in Figure 3.22 (A). Both RNS and 0.04B-RNS-a show the presence of isolated Nb and Ru domains clearly observed on to silica matrix. On the contrary, Nb and Ru species appear homogeneously distributed on the whole surface of 0.16B-RNS-a as better highlighted in Figure 3.22 (B) and (C) where the EDX analysis of the only Nb and Ru are reported. These results further confirm the expected role of Brij-C10 as oxygen-rich complexing agent of the metallic species.

TPR technique was used to get a deeper insight into the redox behaviour of RNS-a and 0.16B-RNS-a, and to assess how addition of Brij-C10 may affect the metal-silica matrix interaction.

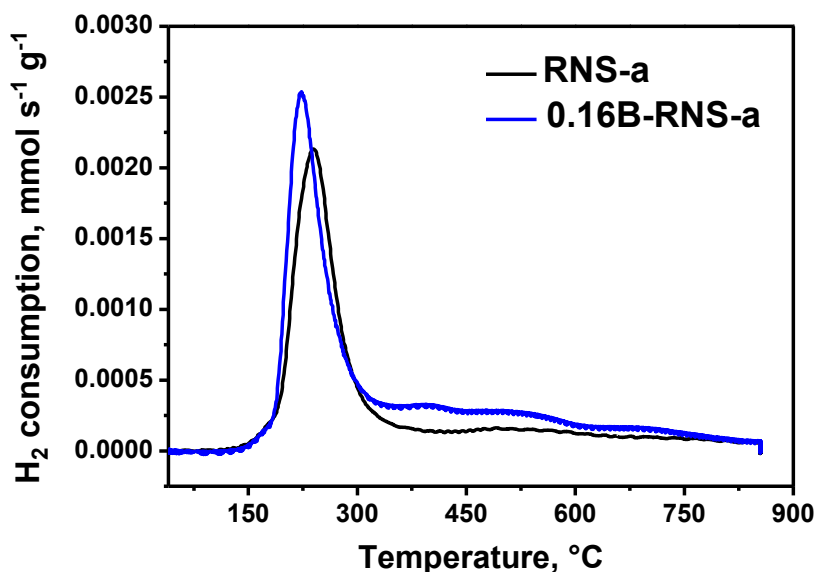
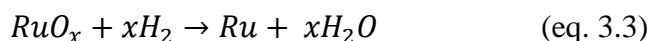


**Figure 3.23.** TPR spectra of annealed RNS-a and 0.16B-RNS-a samples heated at 10 °Cmin<sup>-1</sup> up to 900 °C.

Figure 3.23 reports the TPR curves of samples heated at 10 °Cmin<sup>-1</sup> up to 900 °C. Both curves show a single peak in the low temperature range and a negligible H<sub>2</sub> consumption at higher temperatures. The acknowledged reduction reaction of ruthenium oxides may be written as the general reaction:



where  $x$  identifies different Ru oxides.<sup>118</sup>

Overlapped reduction profiles are seen with a slight shift to higher temperature in the peak maximum: TPR peaks at 223 and 240 °C are indeed seen for samples 0.16B-RNS-a and RNS-a, respectively, which can be assigned to the reduction of RuO<sub>2</sub>,<sup>118</sup> and the corresponding amounts of H<sub>2</sub> consumed are reported in Table T-3.6.

The slight shift to higher temperature observed for RNS-a could be attributed to a major interaction of the metal ion with the support, or to the likely presence of larger RuO<sub>2</sub> particles formed in the absence of O-rich surfactant molecules able to act as complexing agents with respect to the metal. Whatever the case of the peak shift, this does not limit the extent of reduction, since the overall amount of H<sub>2</sub> consumed (Table T-3.6) is nearly the same for both samples and is very close to the stoichiometric one (1.23 mmol), indicating an almost total reduction of the RuO<sub>2</sub>.

In order to thoroughly investigate the catalytic behaviour and to obtain more information on the properties of the metallic Ru phase, a TPR-1/TPO/TPR-2 cycle was carried out heating the samples at  $10\text{ }^{\circ}\text{C min}^{-1}$  up to  $600\text{ }^{\circ}\text{C}$ . In Figure 6, the TPR-1/TPR-2 profiles of the samples are displayed, while the corresponding  $\text{H}_2$  consumption and  $T_{\text{max}}$  values are reported in Table T-3.6.

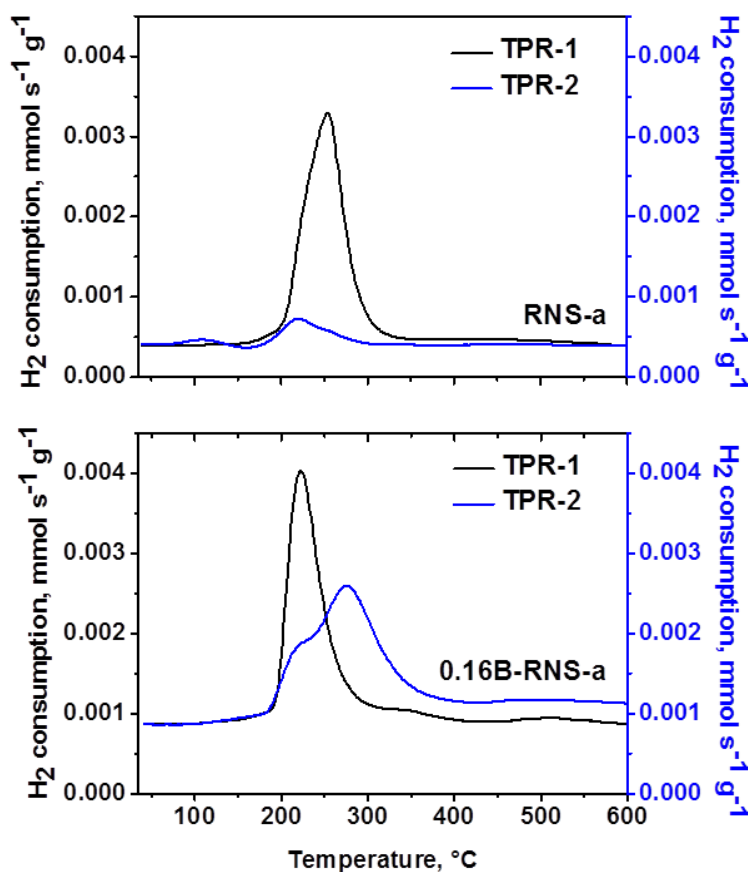


**Figure 3.24.** TPR-1/TPR-2 spectra of the annealed RNS-a and 0.16B-RNS-a samples heated up to  $600\text{ }^{\circ}\text{C}$  at heating rate of  $10\text{ }^{\circ}\text{C min}^{-1}$ .

By comparing the TPR-1/TPR-2 curves of RNS-a, it follows that the oxidation treatment was not effective in regenerating  $\text{RuO}_2$ : the peak of the TPR-2 curve is shifted to lower temperature, and has a smaller area as compared to that of the TPR-1 curve, indicating that the oxidation to  $\text{RuO}_2$  was not completely attained. Additionally, a small peak at  $110\text{ }^{\circ}\text{C}$  is observed, that can be related to the reduction of  $\text{Ru}^{3+}$  species to  $\text{Ru}^{2+}$  species according to Hengne *et al.*<sup>119</sup> This could be due to the presence of bulkier metal particles, difficult to re-oxidize after the first reduction cycle.

**Table T-3.6.**  $T_{\max}$  values and  $H_2$  consumption in the TPR experiments (heating up to 900 °C at h.r. = 10 °C min<sup>-1</sup>) and the TPR-1/TPO/TPR-2 cycle (heating up to 600 °C at h.r. = 10 °C min<sup>-1</sup>).

Sample	$T_{\max}$ (°C)	TPR, $H_2$ (mmol g <sup>-1</sup> )	$T_{\max}$ (°C)	TPR-1, $H_2$ (mmol g <sup>-1</sup> )	$T_{\max}$ (°C)	TPR-2, $H_2$ (mmol g <sup>-1</sup> )
0.16B-RNS-a	223	1.13	222	1.12	213 (sh), 270	1.20
RNS-a	240	1.09	254	1.18	110, 217	0.0124, 0.131

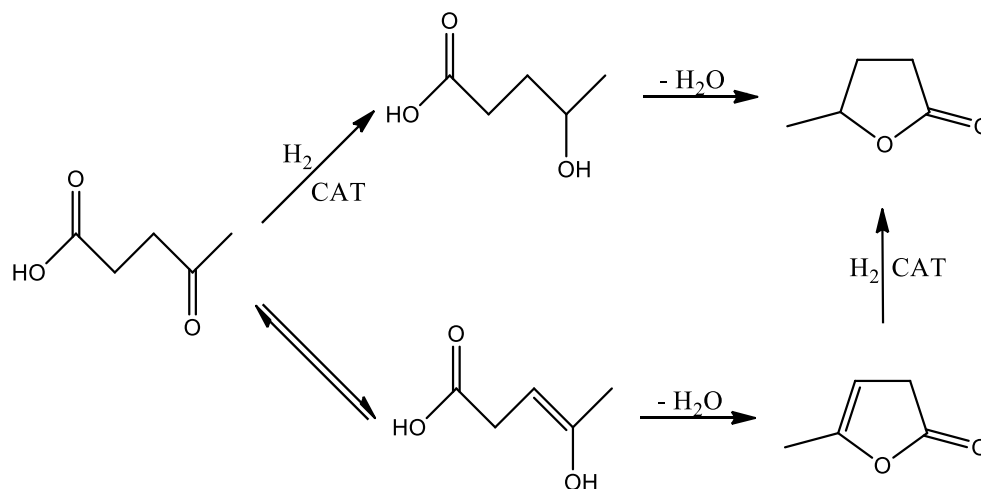
Also the TPR-2 curve of 0.16B-RNS-a does not exactly resemble the corresponding TPR-1 curve: two unresolved peaks are observed indicating the formation of different  $RuO_x$  species during the oxidation treatment. Particularly, the shoulder occurring at lower temperature can be related to the presence of well-dispersed  $RuO_x$  species,<sup>117,120</sup> whereas the peak at higher temperature (270 °C) could be assigned to the reduction of  $Ru(OH)_x$  and/or  $RuO_y(OH)$  species.<sup>121</sup>

The data in Table T-3.6 clearly indicate the effectiveness of the Brij-C10 assisted sol-gel synthesis on the preparation of RNS catalysts: the reducibility of 0.16B-RNS-a is not affected by the oxidative treatment showing a complete reduction after the TPR-2 treatment. Such tendency is compromised within the sample prepared without the surfactant, RNS-a, for which the amount of consumed  $H_2$  during the TPR-2 was much smaller as compared to the TPR-1 treatment. A possible explanation for such a behaviour may lie in the different dispersion degree of  $RuO_x$  particles within the matrix, in agreement with TEM and XRD observations. In the absence of the surfactant molecules, able to coordinate the metal particles, poorly dispersed ruthenium species likely form in RNS-a sample giving larger aggregated that are less sensitive to the oxidative treatment, which causes the formation of a partially oxidized outer layer, though the inner core of the particles remains reduced.

### 3.9 Catalytic activity: Levulinic Acid (LA) hydrogenation

The two catalysts RNS-a and 0.16B-RNS-a were tested in the hydrogenation of LA to GVL. Two main pathways have been proposed for this reaction (see Scheme 3.4). In the former, that seems to prevail under mild conditions,<sup>52</sup> the hydrogenation of LA to  $\gamma$ -hydroxypentanoic acid first occurs, followed by the intramolecular lactonization to GVL. In the second pathway, that seems to prevail at higher temperatures (>200 °C),<sup>55,56</sup> the

cyclising dehydration of the enolic form of LA takes place forming the angelica lactone, that is then hydrogenated leading to GVL.



**Scheme S-3.4.** Reaction pathways<sup>52,55,56</sup>

In order to investigate the reusability of these catalysts, they were subject to multiple cycles. The reaction mixture composition was monitored via GC and the detected species were found to be GVL,  $\gamma$ -hydroxyvaleric acid (HV) and LA. The obtained experimental results are shown in Figure 3.25.

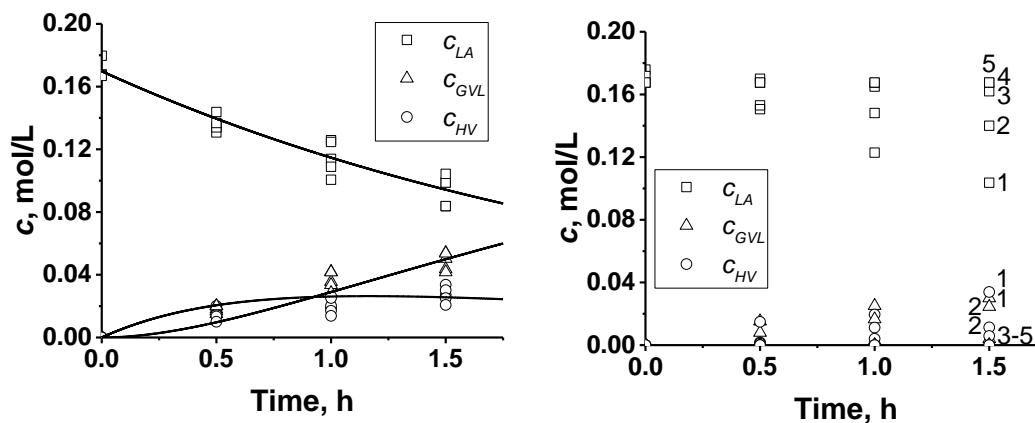


**Figure 3.25.** Concentration profiles obtained using RNS-a (left panel) and 0.16B-RNS-a (right panel) as catalysts. Reaction condition: 300 rpm; 70°C; cat = 0.5 g; LA= 4.0 g; water 200.0 g;  $P_{N_2}$ = 1.0 bar;  $P_{H_2}$ = 20.0 bar; number of cycle 5.

Taking into account that the catalytic performances of the RNS-a were tested under mild conditions, the presence of HV as the only relevant intermediate confirms that the I mechanism, in the pathways of Scheme S-3.4, contributes to the catalytic process.

The left panel of Figure 3.25 shows the concentrations of both reagent/intermediate/product using RNA-a as catalyst. As can be seen the concentration profiles are typical of a reaction in series. The amount of LA gradually decrease as the reaction progressed, while both HV and GVL concentrations increase, furthermore no differences in concentration profiles were observed over all repeated cycles. In fact, all the collected experimental data, scatters roughly inside the experimental errors. These results clearly indicate that RNS-a catalyst is stable under the adopted conditions as any activity loss was ascertained after about 8h of total reaction time.

Surprisingly, significant deactivation is seen in the case of 0.16B-RNS-a catalyst (see the right panel of Figure 3.25). As a matter of fact, a continuous deactivation is observed until 4<sup>th</sup> reuse cycle where no conversion was observed.

Usually, aggregation of ruthenium domains and/or ruthenium leaching, surface adsorption of organic species or formation of the inert RuO<sub>2</sub> are common reasons for deactivation processes.

In order to identify the main causes of the deactivation, both the catalysts were characterized after their reuse. Figure 3.26 displays XRD spectra of RNS-a and 0.16B-RNS-a after the 5<sup>th</sup> reuse cycle.

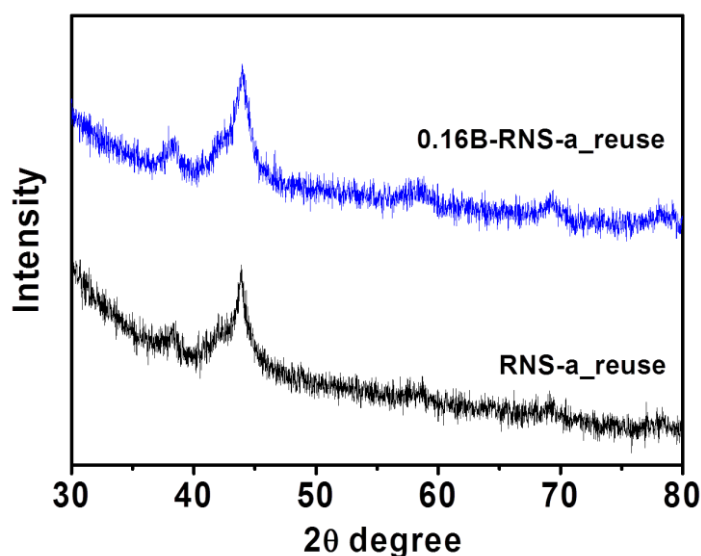


**Figure 3.26.** XRD spectra of RNS-a and 0.16B-RNS-a after the 5<sup>th</sup> reuse cycle.

In spite of the different oxidation behavior shown by RNS-a and 0.16B-RNS-a samples, after the 5<sup>th</sup> reuse cycle only diffraction peaks related to metallic Ru (JCPDS Card No. 06-0663) were seen in their XRD profiles and no peaks corresponding to ruthenium oxide were detected. These results exclude any oxidative phenomena during the use of both catalysts. Considering that the catalysts were reused without any high temperature hydrogenation pre-treatment, all prepared Ru@Nb<sub>2</sub>O<sub>5</sub>-SiO<sub>2</sub> catalysts show a high stability of the Ru metallic species under the experimental conditions of reaction. The average Ru crystallite size of about 5 nm was determined using Scherrer's equation for both samples. Therefore, in the 0.16B-RNS-a catalyst there is no significant modification in the crystallite size with respect to the unreduced sample, whereas the RNS-a samples showed a significant size reduction after its reuse from 25 nm (unreduced sample) to about 5 nm. This result well agrees with the analysis of TEM image of RNS-a reused catalyst displayed in Figure 3.27 where the corresponding particle size distribution (derived from more than 200 nanoparticles) was also reported. These results clearly demonstrate that the synthesized nanomaterials do not suffer of the typical deactivation related to metallic species segregation.

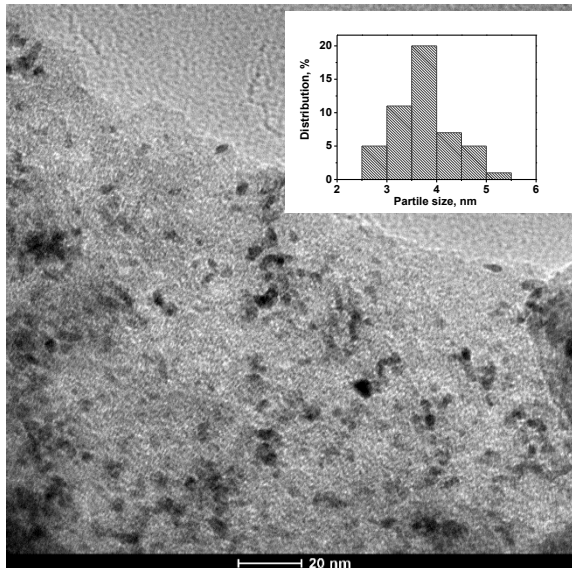


**Figure 3.27.** TEM images of RNS-a after the 5<sup>th</sup> reuse cycle.

To check the eventually surface adsorption of organic species TG curves and FTIR spectra of both reused catalysts were displayed in the left and right panel of Figure 3.28, respectively. Both TG curves exhibit a slight weight loss before 150°C due to desorption of absorbed water. On the contrary, in the temperature range of 150-600 °C a different

behavior is seen: a pronounced weight loss of about 8 wt. % occurs for the 0.16B-RNS-a, while a negligible weight loss takes place for the RNS-a. This weight loss suggests the presence of adsorbed organic species on the 0.16B-RNS-a surface.

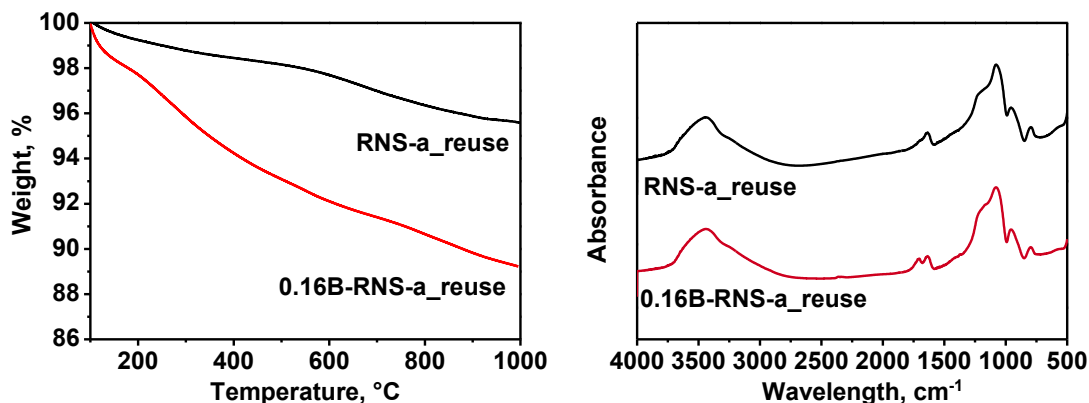


**Figure 3.28.** TG curves (left panel) and FTIR spectra (right panel) of RNS-a and 0.16B-RNS-a after the reuse tests.

To confirm this hypothesis, the FTIR spectra of the reused catalysts (Figure 3.28 right panel) were carried out. Their comparison shows the presence of a new absorption band at about 1715 cm<sup>-1</sup> only in the 0.16B-RNS-a. This band is related to the C=O asymmetric stretching of carbonylic group in carboxylic acids and this result clearly excludes adsorption of the reaction product on the catalyst, since this group in lactones is marked by a distinguished adsorption band at 1768 cm<sup>-1</sup>.<sup>122</sup>

Since both levulinic acid and  $\gamma$ -hydroxypentanoic acid show the adsorption band related to C = O at about the same wavelength value<sup>122,123</sup> it is difficult to distinguish from one another using FTIR analysis.

To assess any preferential adsorption of the reagent or the intermediate onto the samples, adsorption tests were performed on both catalysts, as reported in Figure 3.29.

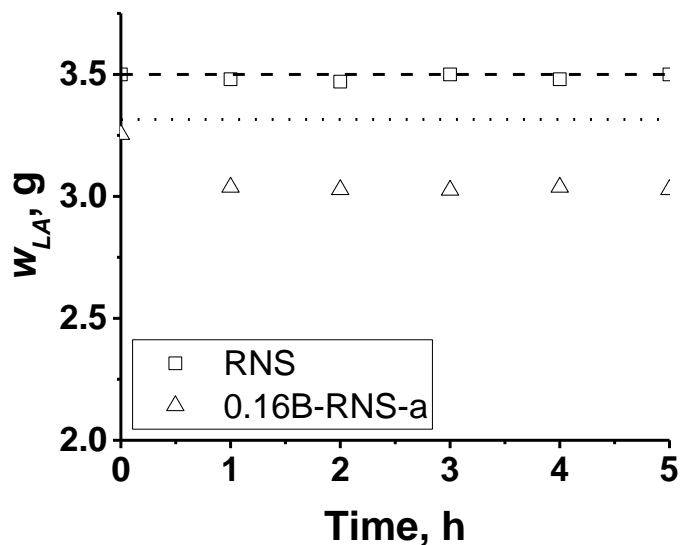


**Figure 3.29.** Levulinic acid adsorption tests performed on both RNS-a and 0.16B-RNS-a catalysts. The experiments have been performed at 70°C, 300rpm, by loading 200g H<sub>2</sub>O and respectively 3.5001g and 3.3155g levulinic acid. RNS-a gave no appreciable adsorption, while 0.16B-RNS-a about 7.5%.

The obtained results show that there is no adsorption of organic species onto the RNS-a catalyst, giving a further confirmation of the stability in the reuse tests of this sample. On the contrary, only levulinic acid is adsorbed on the surface of the 0.16B-RNS-a (about 7.5 %) probably due to the higher surface area of this sample that enhances the amount of adsorption species. These data confirm the strong influence on deactivation of the interaction between acid organic group and the support. In our case the greater surface of 0.16B-RNS catalysts in respect to that of RNS favors the adsorption of acid compounds present in the reaction environment (LA and  $\gamma$ -hydroxypentanoic) producing a strong deactivation effect.

## CONCLUSION

In this PhD research activity hybrid ( $ZrO_2$ -acac) and inorganic ( $Nb_2O_5 \cdot SiO_2$  and  $Ru/RuO_2 @ Nb_2O_5 \cdot SiO_2$ ) mixed oxide materials were synthesized by sol-gel route and characterised in view of their applications in catalytic field.

### *ZrO<sub>2</sub>-based organic-inorganic hybrid materials*

$ZrO_2$ -based hybrid material was prepared using acetylacetone (Hacac) to control the hydrolysis reaction rate of zirconium precursor avoiding the development of a particulate gel. Contrary to the usual practice, these acac complexing/sensitizing molecules were added directly to the solution containing the precursor of zirconium.

The formation of a hybrid homogeneous xerogel (HSGZ), slightly yellow colored, was obtained by a synthesis procedure entirely performed in air at room temperature. The porous gel derived material can be described as a polymeric network of zirconium oxo-clusters, on the surface of which part of  $Zr_4^+$  ions are involved in strong complexation with acac ligands. Therefore, HSGZ can be considered as an acac surface-modified porous zirconia. These characteristics were confirmed by TG-DTA analysis and FTIR spectroscopy which indicated that HSGZ is a highly stable hybrid material. The presence of acac, strongly bond on the surface, induced a ligand-to-metal charge transfer giving light absorption in the visible region with a reduction of band gap value (2.6 eV). The intramolecular acac-to-metal electron transfer mechanism was also responsible of the equilibrium formation between  $Zr(IV)$ -acac and  $Zr(III)$ -acac• complexes on the solid surface from which in presence of molecular  $O_2$ , reactive oxygen species (ROs) were produced. Particularly, the organic ligand played a pivotal role in generating and stabilizing the superoxide radical species ( $\cdot O_2^-$ ) at the HSGZ-air interfaces for very long time. Therefore, HSGZ material behaved like radicals initiator in absence of any light irradiation at room temperature. The ability of this hybrid material to produce these paramagnetic centers was checked by EPR measurements, carried out in absence of irradiation. The presence of free radicals made HSGZ material a useful catalyst in degradation of organic pollutants. Its catalytic activity has been tested in the oxidative degradation of different chlorinated phenoxyalkanoic acid herbicides (MCPA, 2,4-D, 4-CPA, and MCPB) without light irradiation with special reference to evaluation of their degradation kinetics. A virtually complete removal in about 3 days at room temperature

was achieved for the four herbicides. This result is comparable to those usually obtained by photo-oxidation.<sup>102</sup> A long-term application of the HSGZ catalyst tested by repeated-batch tests was achieved, as well.

Finally, these results lead the path toward further development of HSGZ and related hybrid materials for ROS-based energy and environmental applications that do not require any activation procedure neither thermal nor light.

#### *Niobium-silicon mixed oxides*

Niobium-silicon mixed oxide, containing about 19 wt. % of Nb<sub>2</sub>O<sub>5</sub> (NbsgII), was prepared by a sol-gel synthesis procedure and its structural, morphological and textural properties were studied and compared with the results obtained from niobium oxides-based materials containing a similar amount of Nb<sub>2</sub>O<sub>5</sub> but prepared following different synthetic procedures: wet impregnation (Nbimp),<sup>105</sup> different sol-gel route (NbsgI)<sup>44</sup> and pure niobium pentoxide (Nb<sub>2</sub>O<sub>5</sub>).

All materials were tested in the epoxidation of methyl oleate, which is structure-sensitive on crystalline Nb<sub>2</sub>O<sub>5</sub>. It was shown, indeed, that the prevalence of the monoclinic H-phase in the commercial Nb<sub>2</sub>O<sub>5</sub> and of the orthorhombic T-phase in Nbimp catalyst enhances the epoxidation in the first case while promotes the hydrolysis of epoxide in the last instance leading to a decrease of the selectivity. In the amorphous catalysts prepared by sol-gel, instead, the selectivity is moderate and increases for NbsgII material. This effect is due to the presence of different NbO<sub>x</sub> surface species that, interacting with the siloxane matrix, give rise to different acid sites (Brønsted, NbO<sub>6</sub> octahedra, and Lewis, NbO<sub>4</sub> tetrahedra, acid sites) which strongly influence the catalytic performance of investigated catalysts. It was shown that the dispersion of the active NbO<sub>4</sub> tetrahedra in the NbsgII material is the most important factor affecting the oxirane selectivity.

It can be concluded that the nature and the distribution of Nb polyedra are strongly influenced by the synthesis parameters and, in turn, are responsible for the catalytic performance.

#### *Ruthenium-based mixed oxides*

Ru/RuO<sub>2</sub>@Nb<sub>2</sub>O<sub>5</sub>-SiO<sub>2</sub> sol-gel materials, characterized by a very high dispersion of the metallic species, both in the oxidized and reduced state, were successfully synthesised by an innovative co-synthesis process.

The structural properties of the samples were modulated adding a nonionic surfactant directly in the starting solution of precursors that actually plays a role of both pore directing and complexing agent of the metallic species. Varying the amount of the surfactant both the specific surface area and the pore network of the materials can be affected obtaining a very homogeneous distribution of RuO<sub>2</sub> nanocrystals.

Ru@Nb<sub>2</sub>O<sub>5</sub>-SiO<sub>2</sub> were demonstrated to be effective bifunctional catalysts in the hydrogenation of LA to GVL, carried out under mild conditions and in aqueous environment, and the catalytic performances are not influenced by textural properties of these materials in their first use. The reusability experiments showed good stability of the catalyst prepared without the surfactant and any activity loss was ascertained after about 8h of total reaction time. Deactivation phenomena, by contrast, occurred in the catalyst prepared with the surfactant. Deep investigation revealed the adsorption of levulinic acid onto this catalyst, enhanced by the higher surface area that actually caused a deactivation already at the second run of the reuse tests.

## REFERENCES

1. Macwan, D. P.; Dave, P. N.; Chaturvedi, S., *J Mater Sci*, **2011**, 46, 3669-3686.
2. Kumar, S. G.; Devi, L. G., *J. Phys. Chem. A*, **2011**, 115, 13211-13241.
3. Zhang, G.; Kim, G.; Choi, W., *Energy Environ. Sci.*, **2014**, 7, 954-966.
4. Gionco, C.; Paganini, M. C.; Giamello, E.; Burgess, R.; Di Valentin, C.; Pacchioni, G., *J. Phys. Chem. Lett.*, **2014**, 5, 447-451.
5. Gionco, C.; Livraghi, S.; Maurelli, S.; Giamello, E.; Tosoni, S.; Di Valentin, C.; Pacchioni, G., *Chem. Mater.*, **2015**, 27, 3936-3945.
6. Nakahira, T., Grätzel, M., *Makromol. Chem., Rapid Commun.*, **1985**, 6, 341-347.
7. O'Regan, B.; Gratzel, M.; *Nature*, **1991**, 353, 737-740.
8. Vinodgopal, K.; Wynkoop, D. E.; Kamat, P. V., *Environ. Sci. Technol.*, **1996**, 30, 1660-1666.
9. Finkelstein-Shapiro, D.; Petrosko, S. H.; Dimitrijevic, N. M.; Gosztola, D.; Gray, K. A.; Rajh, T.; Tarakeshwar, P.; Mujica, V.; *J. Phys. Chem. Lett.*, **2013**, 4, 475-479.
10. Musumeci, A.; Gosztola, D.; Schiller, T.; Dimitrijevic, N. M.; Mujica, V.; Martin, D.; Rajh, T., *J. Am. Chem. Soc.*, **2009**, 131, 6040-6041.
11. Schubert, U., *Acc. Chem. Res.*, **2007**, 40, 730-737.
12. Brinker, C. J.; Schere, S. W., *Sol-Gel science: the physics and chemistry of sol-gel processing*, Academic Press, New York, **1990**.
13. Sanchez, C.; Gómez-Romero, P., *Functional Hybrid Materials*, Wiley VCH, Weinheim, **2004**.
14. Sanchez, C.; Julian, B.; Belleville, P.; Popall, M., *J. Mater. Chem.*, **2005**, 15, 3559-3592.
15. Sanchez, C.; Shea, K. J.; Kitagawa, S., *Chem. Soc. Rev.*, **2011**, 40, Themed issue: Hybrid material.
16. Schubert, U., *J. Sol-Gel Sci. Technol.*, **2003**, 26, 47-55.
17. Spijksma, G. I.; Bouwmeester, H. J. M.; Blank, D. H. A.; Kessler, V. G., *Chem Commun.*, **2004**, 16, 1874-1875.
18. Seisenbaeva, G. A.; Gohil, S.; Kessler, V. G., *J. Mater. Chem.*, **2006**, 14, 3177-3190.
19. Sanchez, C.; In, M., *J. Non-Cryst. Solids*, **1992**, 147&148, 1-12.

20. Percy, M. J.; Barlett, J. R.; Woolfrey, J. L.; Spiccia, L.; West, B. O., *J. Mater. Chem.*, **1999**, 9, 499-505.
21. Pirozzi, D.; Fanelli, E.; Aronne, A.; Pernice, P.; Mingione, A., *J. Mol. Catal. B: Enzymatic*, **2009**, 59, 116-120.
22. Kessler, V. G.; Spijksma, G. I.; Seisenbaeva, G. A.; Håkansson, S.; Blank, D. H. A.; Bouwmeester, H. J. M., *J. Sol-Gel Sci. Technol.*, **2006**, 40, 163-179.
23. Lemonnier, S.; Grandjean, S.; Robisson, A. C.; Jolivet, J. P., *Dalton Trans.*, **2010**, 39, 2254-2262.
24. van den Brom, C. R.; Vogel, N.; Hauser, C. P.; Goerres, S.; Wagner, M.; Landfester, K.; Weiss, C. K., *Langmuir*, **2011**, 27, 8044-8053.
25. Georgieva, I.; Danchova, N.; Gutzov, S.; Trendafilova, N., *J Mol Model*, **2012**, 18, 2409-2422.
26. Petkova, N.; Dlugocz, S.; Gutzov, S., *J. Non-Cryst. Solids*, **2011**, 357, 1547-1551.
27. Spijksma, G. I.; Bouwmeester, H. J. M.; Blank, D. H. A.; Kessler, V. G., *Chem Commun.*, **2004**, 16, 1874-1875.
28. Jones, A. C., *J. Mater. Chem.*, **2002**, 12, 2576-2590.
29. Fanelli, E.; Turco, M.; Russo, A.; Bagnasco, G.; Marchese, S.; Pernice, P.; Aronne, A., *J. Sol-Gel Sci. Technol.*, **2011**, 426-436.
30. Aronne, A.; Sannino, F.; Bonavolonta, S. R.; Fanelli, E.; Mingione, A.; Pernice, P.; Spaccini, R.; Pirozzi, D., *Environ. Sci. Technol.*, **2012**, 46, 1755-1763.
31. Francisco, M. S. P.; Gushikem, Y., *J. Mater. Chem.*, **2002**, 12, 2552-2558.
32. Dragone, L.; Moggi, P.; Predieri, G.; Zanoni, R., *Appl. Surf. Sci.*, **2002**, 187, 82-88.
33. Julián, B.; Gervais, C.; Cordoncillo, E.; Escribano P.; Babonneau, F.; Sanchez, C., *Chem. Mater.*, **2003**, 15, 3026-3034.
34. Drake, K.; Carta, D.; Skipper, L.J.; Sowrey, F. E.; Newport, R. J.; Smith M. E., *Solid State Nucl. Magn. Reson.*, **2005**, 27, 28-36.
35. Aronne, A.; Turco, M.; Bagnasco, G.; Ramis, G.; Santacesaria, E.; Di Serio, M.; Marenna, E.; Bevilacqua, M.; Cammarano, C.; Fanelli, E., *Appl. Catal., A*, **2008**, 347, 179-185.
36. Di Serio, M.; Turco, R.; Pernice, P.; Aronne, A.; Sannino, F.; Santacesaria, E., *Catal. Today*, **2012**, 192, 112-116.
37. Rosatto, S. S.; Sotomayor, P. T.; Kubota, L. T.; Gushikem, Y., *Electrochim Acta*, **2002**, 47, 4451-4458.

38. Clapsaddle, B. J.; Sprehn, D. W.; Gash, A. E.; Satcher Jr, J. H.; Simpson, R. L., *J. Non-Cryst. Solids*, **2004**, 350, 173-181.
39. Francisco, M. S. P.; Landers, R; Gushikem, Y., *J. Solid State Chem.*, **2004**, 177, 2432-2439.
40. Aronne, A.; Marenga, E.; Califano, V.; Fanelli, E.; Pernice, P.; Trifuoggi, M.; Vergara, A., *J. Sol-Gel Sci. Technol.*, **2007**, 43, 193-204.
41. Braga, V. S.; Dias, J. A.; Dias, S. C. L.; de Macedo, J. L., *Chem Mater.*, **2005**, 17, 690-695.
42. Camargo, E. R.; Popa, M.; Kakihana, M., *Chem Mater.*, **2002**, 14, 2365-2368.
43. Somma, F.; Canton, P.; Strukul, G., *J. Catal.*, **2005**, 229, 490-498.
44. Carniti, P.; Gervasini, A.; Marzo, M., *J. Phys. Chem. C*, **2008**, 112, 14064-14074.
45. Damayanova, S.; Dimitrov, L.; Petrov, L.; Grange, P., *Appl. Surf. Sci.*, **2003**, 214, 68-74.
46. Tanabe, K., *Solid Acids and Bases: their catalytic properties*; Academic Press: New York, **1970**.
47. Kumar, V. V.; Naresh, G.; Sudhakar, M.; Tardio, J.; Bhargava, S. K.; Venugopal, A., *Appl. Catal., A*, **2015**, 505, 217-223.
48. Xu, Q.; Li, X.; Pan, T.; Yu, C.; Deng, J.; Guo, Q.; Fu, Y., *Green Chem.*, **2016**, 18, 1287-1294.
49. Kuwahara, Y.; Magatania, Y.; Hiromi Y., *Catalysis Today*, **2015**, 258, 262-269.
50. Huber, G. W.; Corma, A., *Angew. Chem. Int.*, **2007**, 46, 7184-7201.
51. Alonso, D. M.; Wettstein, S. G.; Dumesic, J. A., *Green Chem.*, **2013**, 15, 584-595.
52. Raspolli Galletti, A. M.; Antonetti, C.; De Luise, V.; Martinelli, M., *Green Chem.*, **2012**, 14, 688-694.
53. Abdelrahman, O. A.; Luo, H. Y.; Heyden, A.; Román-Leshkov, Y.; Bond, J. Q., *J. Catal.*, **2015**, 329, 10-21.
54. Cao, S.; Monnier, J. R.; Williams, C. T.; Diao, W.; Regalbuto, J. R., *J. Catal.*, **2015**, 326, 69-81.
55. Sudhakar, M.; Vijay Kumar, V.; Naresh, G.; Lakshmi Kantam, M.; Bhargava, S.K.; Venugopal, A., *Appl. Catal. B*, **2016**, 180, 113-120.
56. Michel, C.; Zaffran, J.; Ruppert, A. M.; Matras-Michalska, J.; Jedrzejczyk, M.; Grams, J.; Sautet, P., *Chem. Commun.*, **2014**, 50, 12450-12453.
57. Wąchała, M.; Grams, J.; Kwapiński, W.; Ruppert, A. M., *Int. J. Hydrogen Energy*, **2016**, <http://dx.doi.org/10.1016/j.ijhydene.2015.12.089>.

58. Xiao, C.; Goh, T-W.; Qi, Z.; Goes, S.; Brashler, K.; Perez, C.; Huang, W., *ACS Catal.*, **2016**, 6, 593-599.
59. Jansat, S.; Pelzer, K.; García-Antón, J.; Raucoules, R.; Philippot, K.; Maisonnat, A.; Chaudret, B.; Guari, Y.; Mehdi, A.; Reyé, C.; Corriu, R. J. P., *Adv. Funct. Mater.*, **2007**, 17, 3339-3347.
60. Zhang, Y.; Judkins, E. C.; McMillin, D. R.; Mehta, D.; Ren, T., *ACS Catal.*, **2013**, 3, 2474-2478.
61. Lo, C.-P.; Ramani, V., *ACS Appl. Mater. Interfaces*, **2012**, 4, 6109-6116.
62. Matura, V.; Guari, Y.; Reyé, C.; Corriu, R. J. P.; Tristany, M.; Jansat, S.; Philippot, K.; Maisonnat, A.; Chaudret, B., *Adv. Funct. Mater.*, **2009**, 19, 3781-3787.
63. Tristany, M.; Philippot, K.; Guari, Y.; Collière, V.; Lecante, P.; Chaudret, B., *J. Mater. Chem.*, **2010**, 20, 9523-9530.
64. Brinker, C.J.; Bunker, B.C. et al., Structure of Sol-Gel Derived Inorganic Polymers: Silicates and Borates, *Am. Chem. Soc.*, **1988**, 26, 314-332.
65. Jones, R.W., *Fundamental Principles of Sol-Gel Technology*, **1989**.
66. Hench, L. L.; West, J. K., *Chem. Rev.*, **1990**, 90, 33-72.
67. Flory, P. J., *Principles of Polymer Chemistry*, **1953**, Cornell University Press: Ithaca, NY, chapter IX.
68. Fidalgo, A.; Rosa, M. E.; Ilharco, L. M., *Chem. Mater.*, **2003**, 15, 2186-2192.
69. Ciriminna, R.; Fidalgo, A.; Pandarus, V.; Béland, F.; Ilharco, L. M.; Pagliaro M., *Chem. Rev.*, **2013**, 113, 6592-6620.
70. Dislich, H.; Hinz, P., *J. Non-Cryst. Solids*, **1982**, 48, 11-16.
71. Klein, L.C.; Garvey, G.J., *Mater. Res. Soc. Sym. Proc.*, **1984**, 32, 33-36.
72. Keefer, K. D., *Mater. Res. Soc. Sym. Proc.*, **1984**, 32, 15-24.
73. Livage, J.; Henry, M.; Sanchez, C., *Prog. Solid St. Chem.*, **1988**, 18, 259-341.
74. Gottardi, V.; Guglielmi, M.; Bertoluzza, A.; Fagnano, C.; Morelli, M. A., *J. Non-Cryst. Solids*, **1984**, 63, 71-80.
75. Bechtold, M. F.; Mahler, W.; Schunn, R. A., *J. Polym. Sci.:Polym. Chem.*, **1980**, 18, 2823-2855.
76. Hurd, C. B.; *Chem. Rev.*, **1938**, 22, 403-422.
77. Colby, M.; Osaka, A.; Mackenzie, J. D.; *J. Non-Cryst. Solids*, **1988**, 99, 129-139.
78. Debsikdar, J. C., *Adv. Ceram. Mater*, **1986**, 1, 93-98.

79. Mackenzie, J. D., *Science of Ceramic Chemical Processing*, eds. Hench, L. L.; Ulrich, D. R.: New York, **1986**, 113-122.
80. Chen, K. C.; Tsuchiya, T.; Mackenzie, J. D., *J. Non-Cryst. Solids*, **1986**, 81, 227-237.
81. Schubert, U., *J. Mater. Chem.*, **2005**, 15, 3701-3715.
82. Sanchez, C.; Livage, J.; Henry, M.; Babonneau, F., *J. Non-Cryst. Solids*, **1988**, 100, 65-76.
83. Kessler, J. *Sol-Gel Sci. Techn.*, **2009**, 51, 264-271.
84. Schattka, J. H.; Wong, E. H.-M. M.; Antonietti, M.; Caruso, R. A., *J. Mater. Chem.*, **2006**, 16, 1414-1420.
85. Rosen, M. J.; Dahanayake, M., *Industrial Utilization of Surfactants: Principles and Practice*, Amer Oil Chemists Society, **2000**.
86. Anderson, A.-L.; Binions, R., *Polyhedron*, **2015**, 85, 83-92.
87. Sannino, F.; Pernice, P.; Minieri, L.; Camandona, G. A.; Aronne, A.; Pirozzi, D.; *Appl. Mater. Interfaces*, **2015**, 7, 256-263.
88. Muñoz-García, A. B.; Sannino, F.; Vitiello, G.; Pirozzi, D.; Minieri, L.; Aronne, A.; Pernice, P.; Pavone, M.; D'Errico G., *ACS Appl. Mater. Interfaces*, **2015**, 7, 21662-21667.
89. Turco, R.; Aronne, A.; Carniti, P.; Gervasini, A.; Minieri, L.; Pernice, P.; Tesser, R.; Vitiello, R.; Di Serio, M., *Catal. Today*, **2015**, 254, 99-103.
90. Dickie, S. A.; McQuillan, A. J., *Langmuir*, **2004**, 20, 11630-11636.
91. Klepper, K. B.; Nilsen, O.; Hansen, P.-A.; Fjellvåg, H., *Dalton Trans.*, **2011**, 40, 4636-4646.
92. Esposito, S.; Turco, M.; Bagnasco, G.; Cammarano, C.; Pernice, P.; Aronne, A., *Appl Catal., A*, **2010**, 372, 48-57.
93. Aronne, A.; Vladimir, N.; Champagnon, S. B.; Fanelli, E.; Califano, V.; Usmanova, L. Z.; Pernice, P., *J. Non-Cryst. Solids*, **2005**, 351, 3610-3618.
94. Chang, S.-m.; Doong, R.-a.; *Chem. Mater.* **2007**, 19, 4804-4810.
95. Gionco, C.; Paganini, M. C.; Giamello, E.; Burgess, R.; Di Valentin, C.; Pacchioni, G., *Chem. Mater.*, **2013**, 25, 2243-2253.
96. Cesareo, E.; Korkina, L.; D'Errico, G.; Vitiello, G.; Aguzzi, M. S.; Passarelli, F.; Pedersen, J. Z.; Facchiano, A., *PlosOne*, **2012**, 7, e48849.
97. Anpo, M.; Che, M.; Fubini, B.; Garrone, E.; Giamello, E.; Paganini, M. C., *Top. Catal.*, **1999**, 8, 189-198.

98. Pieta, P.; Petr, A.; Kutner, W.; Dunsch, L., *Electrochim. Acta*, **2008**, 53, 3412-3415.
99. Bedilo, A. F.; Plotnikov, M. A.; Mezentseva, N. V.; Volodin, A. M.; Zhidomirov, G. M.; Rybkin, I. M.; Klabunde, K. J., *Phys. Chem. Chem. Phys.*, **2005**, 7, 3059-3069.
100. Sannino, F.; Pirozzi, D.; Vitiello, G.; D'Errico, G.; Aronne, A.; Fanelli, E.; Pernice, P., *Appl. Catal. B*, **2014**, 156-157, 101-107.
101. Ozacar, M.; Sengil, I. A., *J. Environ. Manage*, **2006**, 80, 372-379.
102. Vione, D.; Khanra, S.; Das, R.; Minero, C.; Maurino, V.; Brigante, M.; Mailhot, G., *Water Res.*, **2010**, 44, 6053-6062.
103. Burrows, H. D.; Canle, M.; Santaballa, J. A.; Steenkenc, S., *J. Photochem. Photobiol. B*, **2002**, 67, 71-108.
104. Öneby, K.; Håkansson, S.; Pizzul, L.; Stenström, J., *Biodegradation*, **2014**, 25, 291-300.
105. Medeiros, F. F. P.; Moura, M. F. V.; da Silva, A. G. P.; Souza, C. P.; Gomes, K. K. P.; Gomes, U. U.; *Braz. J. Chem. Eng.*, **2006**, 23, 531-538.
106. Nowak, I.; Ziolk, M., *Chem. Rev.* **1999**, 99, 3603-3624.
107. Zhu, H.; Zheng, Z.; Gao, X.; Huang, Y.; Yan, Z.; Zou, J.; Yin, H.; Zou, Q.; Kable, S. H.; Zhao, J.; Xi, Y.; Martens, W. N.; Frost, R. L., *J. Am. Chem. Soc.*, **2006**, 128, 2373-2384.
108. Gallo, A.; Tiozzo, C.; Psaro, R.; Carniato, F.; Guidotti, M., *J. Catal.*, **2013**, 298, 77-83.
109. Tiozzo, C.; Bisio, C.; Carniato, F.; Gallo, A.; Scott, S. L.; Psaro, R.; Guidotti, M., *Phys. Chem. Chem. Phys.*, **2013**, 15, 13354-13362.
110. Innocenzi, P., *J Non-Cryst Solids*, **2003**, 316, 309-319.
111. Gallardo, J.; Durán, A.; Di Martino, D.; Almeida, R. M., *J. Non-Cryst. Solids*, **2002**, 298, 219-225.
112. Cerruti, M.; Magnacca, G.; Bolis, V.; Morterra, C., *J Mater Chem*, **2003**, 13, 1279-1286.
113. Fidalgo, A.; Ilharco, L. M., *J. Non-Cryst. Solids*, **2001**, 283, 144-154.
114. Zhang, L.; Shi, H.; Li, W.; Zhang, X., *Thermoch. Acta*, **2003**, 570, 1-7.
115. Clayden, N. J.; Accardo, G.; Mazzei, P.; Piccolo, A.; Pernice, P.; Vergara, A.; Ferone, C.; Aronne, A., *J. Mater. Chem. A*, **2015**, 3, 15986-15995.
116. Kalapathy, U.; Proctor, A.; Shultz, J., *Bioresour. Technol.*, **2000**, 73, 257-262.

117. Velmurugan, P.; Shim, J.; Lee, K.-J.; Cho, M.; Lim, S.-S.; Seo, S.-K.; Cho, K.-M.; Bang, K.-S.; Oh, B.-T. *J. Ind. Eng. Chem.*, **2015**, <http://dx.doi.org/10.1016/j.jiec.2015.04.009>.
118. Lanza, R.; Järås, S.G.; Canu, P., *Appl. Catal., A*, **2007**, 325, 57-67.
119. Hengne, A. M.; Biradar, N. S.; Rode, C. V., *Catal Lett*, **2012**, 142, 779-787.
120. Bagnasco, G.; Cammarano, C.; Turco, M.; Esposito, S.; Aronne, A.; Pernice, P., *Thermochim Acta*, **2008**, 471, 51-54.
121. Manyara, H.G.; Weberb, D.; Dalya, H.; Thompsona, J. T.; Rooneya, D. W.; Gladdenb, L. F.; Stittc, E. H.; Delgadod, J. J.; Bernald, S.; Hardacrea, C., *J. Catal.*, **2009**, 265, 80-88.
122. Tukacs, J.M.; Király, D.; Strádi, A.; Novodarszki, G.; Eke, Z.; Dibó, G.; Kégl T.; Mika, L.T., *Green Chem*, **2012**, 14, 2057-2065.
123. Chappell, J.S.; Meyn, A.W.; Ngim, K. K., *J Forensic Sci*, **2004**, 49, 1-8.